Development of remotely sensed image velocimetry for large-scale free surface flows

Application to the flow through the Eastern Scheldt storm surge barrier

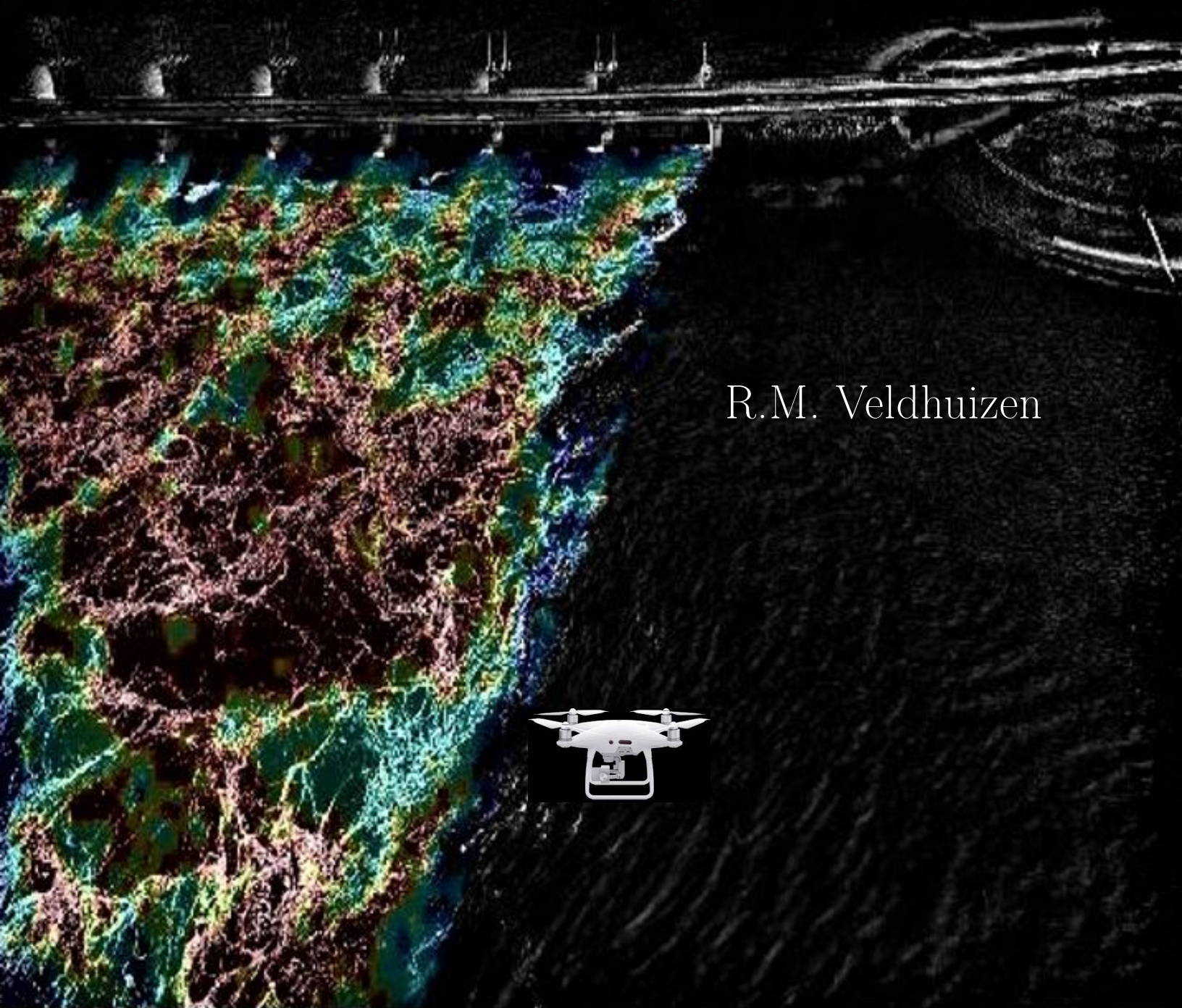

R.M. Veldhuizen

Development of remotely sensed image velocimetry for large-scale free surface flows

Application to the flow through the Eastern Scheldt Storm Surge Barrier

by

R.M. Veldhuizen

to obtain the degree of Master of Science
at the Delft University of Technology,
to be defended publicly on July 15, 2021

Student number:	5070155	
Thesis committee:	Dr. ir. R. J. Labeur,	TU Delft, chairman
	Prof. dr. ir. W. S. J. Uijttewaal,	TU Delft
	Dr. A. A. Simkooei,	TU Delft
	Dr. ir. Y. B. Broekema,	Deltares

An electronic version of this thesis is available at http://repository.tudelft.nl/.

Cover image: Greyscale image of the Eastern Scheldt storm surge barrier. The flow entering the estuary is overlain by a velocity field derived from remotely sensed image velocimetry (RSIV). Red colors indicate highest velocities, whereas blue colors are associated with the smallest velocities.

TU Delft Delft University of Technology

Deltares Enabling Delta Life

Preface

This thesis concludes my Master of Science in Geoscience & Remote Sensing at Delft University of Technology. The topic of this thesis reflects my passion for the observation of geophysical processes on the Earth's surface, with applications related to environmental fluid mechanics. Despite the challenges that this research has brought me, along with the global pandemic changing the course of our lives, I truly enjoyed the quest to apply data analysis and hydrodynamic theory to a specific hydraulic engineering case study. This final product cannot express the long days spent to manage a field campaign, and to better understand the fundamental principles associated with environmental flows. It also does not reflect the joy for the synthesis, the hope for good results and the frustration with each failed attempt. It however has provided me with invaluable knowledge of a subject I feel very passionate about, but of which I never got the chance to work on in practice. It has been without doubt the most rewarding part of my studies.

My gratitude goes out to the thesis committee for their constructive criticism during the meetings. I would like to thank Robert Jan Labeur as the chairman of the committee, establishing the first link with Deltares and being involved in the major decisions within the framework of this thesis. I also want to thank Alireza Simkooei for his help on the mathematics related to camera projections. You were always there when I needed you. Furthermore, I am thankful for Wim Uijttewaal for answering essential questions and to be the stand-in chairman during the final part of my thesis. I would like to give special thanks to Yorick Broekema for his admirable faith in the process, taking away many doubts I had along the way. You also provided me with me the best Deltares experience I could possibly have under the considered circumstances. The amount of time you put into your support is deeply appreciated. Although not related to the topic of this thesis, our lab days with Niek Bruinsma were a very enjoyable distraction from the long days working at home.

I am also grateful for the collaboration with Rijkswaterstaat and their indispensable contribution to the measurement campaign. Assistance from Merel Verbeek in the form of a Matlab script and her connections with employees from Rijkswaterstaat appeared to be a great asset to this work. Marijn van Helvert, Jan-Willem Mol, Lidwien de Bruijn, Dannie Beks, Veerle Sperber, Krijn Saman, and Piet Lievense were all closely involved in the project. Thank you for arranging the ADCP measurements on such short notice.

Finally, I would like to thank Noortje for her unconditional support throughout my entire studies. You were the one to convince me to pursue my dreams when I was about to finish my previous Bachelors, even though that meant I had to move back to a room the size of a walk-in closet. The last couple of months have not been easy for us both, with the turmoil of moving to our new home in Utrecht during the final stage of our theses. I'm really looking forward graduating together and starting a new chapter in our lives.

R.M. (Rick) Veldhuizen
July 2021

Summary

The Eastern Scheldt storm surge barrier (ES-SSB) is the largest hydraulic structure in the Netherlands. Its semi-open inlets allow for North Sea waters to enter and leave the Eastern Scheldt estuary with each tidal cycle, and can be closed during extreme storm events. The flow through the barrier is strongly contracted, and complex flow patterns emerge. Among characteristic flow features are the shallow jet and shallow mixing layer, generated as a result of large transverse shear stresses with horizontal lengths scales greatly exceeding the water depth. Large mean velocities in combination with the developing lateral non-uniformity of the flow between slack water and maximum flood gives rise to higher bed shear stresses. A bed protection up to a distance of about 600 m from the barrier is applied to stabilize the bed against increased hydraulic loading. Scour hole development adjacent to the applied bed protection was anticipated for, but expected equilibrium depths have not yet been reached. Reaching local depths of 60 m with respect to the water surface, these scour holes may on the long term be a threat to the stability of the barrier. Broekema (2020) concluded that during flow contraction, separation of flow near the bed of the scour hole is suppressed and high flow velocities in streamwise direction are found near the bed. Cyclic variations in lateral non-uniformity affect turbulence intensities and subsequent mixing of mass and momentum. Scour growth is therefore enhanced in two ways: i) velocities in the main flow remain high due to horizontal flow convergence, and ii) lateral velocity gradients are associated with larger turbulence intensities that are likely leading to larger bed shear stresses.

A field campaign was carried out at the ES-SSB in an attempt to better understand the relevant flow processes in the area. Drone images and acoustic doppler current profilers (ADCP) data were collected near the Roompot inlet section of the barrier on March 1, 2021. The images were processed using remotely sensed image velocimetry (RSIV). This new technique follows the procedure of conventional particle image velocimetry (PIV) in which displacements between image pairs are tracked and correlated, but is here adapted to be applicable for large-scale free surface flows. In contrast to single-point instruments measuring velocities at specific locations within the flow, RSIV data may provide information on the flow field as a whole. The development of this tool is an important component within the framework of this thesis, with a particular attention to the quality of the results. ADCP measurements were used to validate the RSIV-derived flow field and provided complementary information on temporal flow variations along specific transects in the area.

Ground control points (GCPs) were required to transform between image coordinates and a physical space. The challenge of dealing with a limited distribution of GCPs over a vast body of water was explored well in advance. Laboratory experiments were carried out to estimate the accuracy of the camera projection for various GCP configurations prior to the field campaign. A selection of these distributions therefore resembled those intended to be used at the Roompot inlet. Both from the experiments and the field application the value of more evenly distributed GCPs was well emphasized on. At the Roompot inlet the conversion between the imaged planed and a world coordinate reference system was restricted to a 2D (planar) projection as a result of an insufficient amount of GCPs positioned in streamwise direction. Despite small variations

in GCP elevations, relative errors between several distances across the domain measured by GPS and those estimated by the 2D projection were found not to exceed a few percent. Information on image transformation was missing at large distances ($>$ 100 m) from the barrier. Loss of projection quality in these areas may be partially compensated for by diminishing projection errors with decreasing distance to the camera, the relative importance of which could not be further studied.

The global flow field derived from RSIV showed velocities ranging between 2 - 3 ms^{-1} close to the barrier, to 1 - 2 ms^{-1} at a distance of 250 m in streamwise direction. Largest deviations were found near each separate opening in the inlet where insufficient lightning caused computed vectors to be either absent or underestimated. The results confirm a jet-like flow structure with high centreline velocities and strong horizontal gradients. Differences of about 0.2 - 0.6 ms^{-1} were generally found between overlapping RSIV and ADCP-derived velocities, which were mostly attributed to the different time intervals of measuring, the lack of ADCP data in highly turbulent flows, and the depth difference over which velocities were computed. The quality of the results motivate the collection of additional videos required to estimate the temporal evolution of the flow over a tidal cycle.

The developing flow non-uniformity was well captured by the ADCP measurements. Lateral velocity gradients computed across several lateral transects within the domain increased between 3 hrs and 1 hr before maximum flood (T_1 - T_3). At each interval lateral velocity gradients decreased in streamwise direction, along with a spatial growth of the mixing layer toward the scour hole. A large recirculation zone was shown to develop between the time intervals, leading to strong return currents close the scour hole. These currents are accompanied by streamline contraction on the interface of the main flow and adjacent water. Flow contraction and associated large lateral gradients during maximum flood were also observed on the upstream edge of the scour hole.

The results from this thesis showed that under certain conditions RSIV can be a valuable and promising tool to estimate the large-scale flow field around hydraulic structures. The estimated horizontal flow field may add to the understanding of scour processes at the ES-SSB via the following two observed flow features: (i) high mean velocities in the centre of the main flow, and (ii) large lateral horizontal shear. This, in combination with horizontal flow convergence of the jet observed by ADCP measurements supports the notion that scour development may be related to the laterally non-uniform flow.

Contents

List of Figures

List of Tables

1 Introduction

1.1 Background

The deltaic evolution of the Netherlands throughout geological history urges the country to cope with natural waters in a way unique in the world. Marine trading routes crossing the adjacent coastal waters have brought prosperity and knowledge in the past centuries, and its major rivers are the primary gateway to the European hinterland. The abundance of water however does not come without jeopardy, as almost a third of the country's surface area is located beneath sea level. Major flooding events with thousands of casualties already date back to 838 AD (Van Baars and Van Kempen, 2009). In order to avoid the increasing damage to the densely populated country, these events have inevitably led to a series of hydraulic engineering applications to interfere in the natural system. Among the most famous of these solutions are the Deltaworks, built in the immediate response to the so-called 'Watersnoodramp' in 1953. One of its key components is the Eastern Scheldt storm surge barrier (ES-SSB), located in the southwestern part of the Netherlands in the province of Zeeland (Figure 1.1).

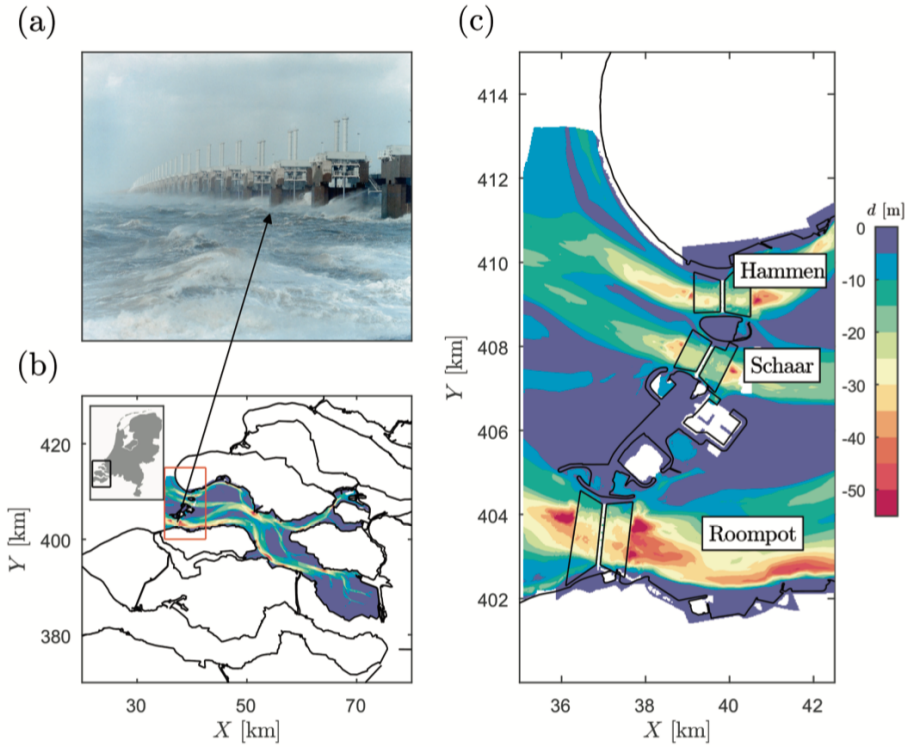

Figure 1.1: (a) An aerial image of the ES-SSB during a storm. (b) Location of the barrier and bathymetry of the basin. (c) Close-up of the bathymetry at the inlet. The scour holes are visible as dark-red patches. Bed protection is indicated with the black, solid lines (Broekema, 2020).

The ES-SSB is a primary flood defence system with a total length of 9 km. Rather than closing off the sea completely, the ES-SSB consists of a series of gates and dams that allow tidal water from the North Sea to enter and leave Eastern Scheldt estuary. The dams cover 5 km of the entrance, the remaining 4 km are covered by the three main inlets of the estuary, from south to north: *Roompot*, *Schaar*, and *Hammen* (Figure 1.1c). The semi-open structure of the ES-SSB allows for many of the estuary's dynamics to be retained, among which its salinity and tidal character, and helps preserving the ecological value of the area.

1.2 Problem statement

The tidal flow through the inlets strongly contracts, and continuity forces large flow accelerations around the inlets. The conditions at the ES-SSB therefore induce large potential for scour, which may on the long term affect the stability of the barrier. In recent years, multiple studies to understand flow dynamics around scour holes in the area have been performed. It appears that a positive feedback contributes to the increasingly high flow velocities around scour holes, thereby suppressing or even increasing their development. Broekema (2020) demonstrated that for certain stages within the tidal cycle two major flow patterns can be distinguished that are induced by changes in lateral non-uniformity in the flow: (i) vertical flow attachment and horizontal flow divergence, and (ii) vertical flow separation and horizontal flow convergence. The contracting flow and high turbulence intensities developing in laterally non-uniform flows apply additional bed shear stress to the underlying bathymetry around the ES-SSB. At the Roompot inlet, the bed reaches depths up to 60 m (Figure 1.1c). To account for these high bed shear stresses, bed protection up to a distance of about 600 m from the barrier's centreline were included in its design. Nevertheless, scour hole development has not yet reached an equilibrium but instead is still an ongoing process.

1.3 Data acquisition campaign

The non-uniformity of the flow and associated increased bed shear stresses are related to large horizontal flow patterns around the ES-SSB. Among these characteristic flow features are the shallow jet and shallow mixing layer, generated as a result of large transverse shear stresses with horizontal lengths scales greatly exceeding the water depth. These large-scale flow structures were studied near the Roompot inlet section of the barrier. To this end, a field campaign was carried out on March 1, 2021, during which data was collected using two techniques:

- **Remotely sensed image velocimetry (RSIV)**. RSIV is a whole-field measurement technique based on tracking displacements of features on the water surface between pairs of images. The procedure generally follows that of conventional particle image velocimetry (PIV), though is adapted to be applicable for (very) large areas using mobile filming. At the Roompot inlet these features are present in the form of bubbles and foam (or "boils") generated by the contracting flow through the barrier. Successive images were collected using a drone in order to capture the large water surface area. The motion of surface features between each image is estimated from an autocorrelation procedure. This requires information on the physical dimensions of the area to be known by projecting image coordinates (in pixels) to world coordinates (in X, Y, Z). Such a transformation can be established by capturing a series of reference points called ground control points (GCPs) visible on each image. The estimated distances of the flow features between image pairs and the known camera frame rate then

allow velocities over the water surface to be computed. Correcting and calibrating data obtained by drones however is not trivial over such a large field-of-view, and the distribution of GCPs is restricted by the large water surface in the domain. In this thesis therefore emphasis is put on the development of this innovative technique for large-scale hydraulic applications, taking into account the potential and restrictions of the parameters that are subtracted from the post-processed results.

- **Acoustic Doppler current profiler (ADCP)**. ADCP is an acoustic method to determine velocity profiles over the whole water column, using the scattering of ultrasound by particles that move with the flow. ADCP measurements at the Roompot area are carried out along specific transects sailed by a vessel, providing high quality data over 0.5 m depth intervals. This data is expected to contribute to the study on temporal flow development between slack water and maximum flood. The measurements are also used as a validation of the RSIV-derived velocities.

1.4 Objective and research questions

The core focus of this research is to study large-scale horizontal flow patterns near the Roompot inlet. Extracted velocity fields derived from RSIV and ADCP may provide complementary knowledge on the behaviour of flow non-uniformity and its relation to ongoing scour hole development in environmental flows. This research therefore also addresses the applicability of RSIV for related future projects in which surface flow velocities over large domains are to be measured. The primary research question can be formulated as follows:

How can remotely sensed image velocimetry be developed to estimate surface flow velocities for large-scale environmental flow applications?

The main question is divided into sub-questions corresponding to the different chapters in this thesis:

1. Which hydrodynamic processes are important to describe the flow patterns and development of scour holes at the Roompot inlet? (Chapter 2)
2. How can drone images and ADCP measurements be successfully obtained to study the relevant flow phenomena? (Chapter 3)
3. What information can be subtracted from the RSIV-derived flow field and what is the quality of the data? (Chapter 4)
4. To what extent can the RSIV and ADCP data be used to quantify large-scale horizontal flow patterns at the Roompot area? (Chapter 4)

1.5 Methodology and thesis outline

To answer the research questions, first a general study on the topic of shallow-flow dynamics is shared in Chapter 2. The fundamental aspects of 2D flow patterns and turbulence in open channel flows are reviewed to put the theory in the context of this thesis. It will also cover flow characteristics present at the Roompot inlet, and their implications on the ongoing scour. Data acquisition from the field campaign is the topic

of Chapter 3, in which the experimental setup and methodology of the RSIV and ADCP applications are described. It elaborates on the practical aspects of collecting and calibrating the images from the Roompot area suitable for RSIV post-processing.
The results and analysis of the data are discussed in Chapter 4. Starting with the quality of the projection matrix for various GCP configurations, the processed images are evaluated using a RSIV sensitivity study. The derived flow field is then validated by image-based observations and ADCP measurements to assess the quality of the data, followed by an ADCP time series analysis to study temporal variations in flow patterns between slack tide and maximum flood. In Chapter 5, the primary concepts considered in this research are discussed. Key elements are the interpretations of the derived results, and the capabilities and limitations of RSIV for studying the relevant flow phenomena. Chapter 6 contains the major conclusions established in this thesis, answering the research questions and providing recommendations for future studies on the subject.

2 Hydrodynamics in shallow flows

This chapter provides an overview of literature on the topics of horizontal shear flows and turbulence, and their relation to scour hole development required to put this study into context. In shallow flow problems velocity information with high spatial and temporal resolution is needed to understand the dynamics of the flow and the related mixing processes (Kantoush and Schleiss, 2009). Horizontal length scales of large-scale structures in these flows are much larger than the vertical extent of the flow. The fundamental properties in shallow flows can therefore be obtained by measuring surface velocities because the dominating processes develop in the horizontal plane. The shallowness of the flow imposes a characteristic length scale for the maximum size of turbulent structures in vertical direction. In free surface flows without lateral shear, the sizes of the turbulent structures (e.g. vortices) that emerge are mainly governed by the balance between the 2D production of turbulent kinetic energy at larger length scales in the upper part of the water column, and the decay of large structures as a result of interaction with the 3D turbulence generated near the bottom (Pan and Banerjee, 1995).

The chapter starts with a general description of shallow flows in Section 2.1. Their characteristics are covered in Section 2.2, including the two most important shallow flow patterns found near the Roompot inlet: the shallow jet and shallow mixing layer. A thorough description of 2D flows that occur around the Roompot scour hole then follows naturally in Section 2.3. The chapter continues with the implications of these shallow flows for the hydraulic loading on the bed. Section 2.4 therefore covers the relation between large-scale hydrodynamics and scour hole development. The most relevant conclusions of the theory covered in this chapter are captured in Section 2.5. Derivations of the relevant equations of motion and details on turbulence are provided in Appendix B.

2.1 General aspects of shallow flow dynamics

Lateral flow non-uniformity is an important concept in this research, because its shear instabilities lead to large-scale turbulence structures that control the mass and momentum exchange between fluids with different velocities. Its spatial development is therefore crucial to link horizontal flow structures to near-bed processes. Turbulence is induced when excessive kinetic energy in parts of the fluid overcomes the damping effect of the fluid's viscosity. The onset of turbulence is commonly expressed by the ratio of advective to viscous forces via the Reynolds number as

$$Re = \frac{\mathcal{L}\,\mathcal{U}}{\nu}, \tag{2.1}$$

where $\mathcal{L}$ and $\mathcal{U}$ are characteristic length scales and velocity scales, respectively, and ν is the kinematic viscosity of the fluid (m^2/s). For Re $>$ 2000, non-linear advective terms dominate and the flow can become hydrodynamically unstable (Nieuwstadt et al., 2016). Turbulence is induced by shear in a direction normal to the local flow velocity, causing the internally unstable flow to generate vortices or 'eddies' of sizes ranging from millimeter scale to horizontal length scales much larger than the water depth. The energetic aspects of turbulence involve two equations: one for the kinetic energy in the mean flow and another for the fluctuating

velocity in the turbulent flow. These equations lead to two fundamental results:

1. Turbulent kinetic energy is produced in the macrostructure and dissipated in the microstructure by molecular viscosity
2. Production and dissipation of turbulent kinetic energy are, in a first approximation, in local equillibrium.

The mechanism of energy transfer from the macroscale to the microscale is at the heart of turbulent flow behaviour and follows from a concept called vortex stretching. Although this process can only be driven in 3D space, many authors have adopted the term "quasi-2D" for vortices generated in open channel flows and geophysical flows where horizontal length scales are much larger than the water depth ($\mathcal{L} \gg h$ (Jirka, 2001; van Heijst, 2007; Talstra, 2011)). For such flows, large horizontal eddies are assumed to be depth-uniform because vortex stretching is strongly limited in the vertical direction. The quasi-2D nature of these dynamic recirculation zones has led to the widely adopted term "2D coherent structures", of which their characteristics will be discussed in the following section.

2.2 2D coherent structures

2.2.1 Definition and composition

Jirka (2001) distinguishes tree types of 2DCS that are primarily found in environmental flows: shallow wakes, shallow mixing layers, and shallow jets. The latter two are easily recognized at the Roompot inlet and will be treated in this section. Within the vortical structure of 2DCS, mass and momentum are isolated from the mean flow and their large scales can generate more effective mixing than 3D turbulent flow field alone (Weitbrecht et al., 2008; Socolofsky and Jirka, 2004). The vorticity contained in 2DCS originates from the initial transverse shear imparted on these flow during their generation. Jirka (2001) has defined three mechanisms for the generation of 2DCS that are also present at the Roompot area:

1. *Topographical forcing.* This is the strongest of the three mechanisms and induced by detachment of the boundary layer as flow passes objects or topographical features. 2DCS are generated by return velocities and strong transverse shear. An example of this mechanism is the flow passing through the ES-SSB that is partially obstructed by the pillars in between the inlet openings.
2. *Internal transverse shear instabilities.* Gradual spatial growth of the 2DCS is enhanced by velocity variations in transverse directions within the flow domain. Such gradients are well apparent within the jet-like flow structure downstream of the inlets, causing large horizontal shear between the main flow and surrounding waters.
3. *Secondary instabilities of the base flow.* This is the weakest of the three forcing mechanisms and describes the generation of 2DCS by the “upcascading” (backscatter) of 3D turbulence structures to larger scales. It is likely that upcascading does also play a role in the highly turbulent flow around Roompot inlet, where energy is continuously redistributed by means of conservation of kinetic energy and enstrophy.

The three mechanisms are illustrated in Figure 2.1.

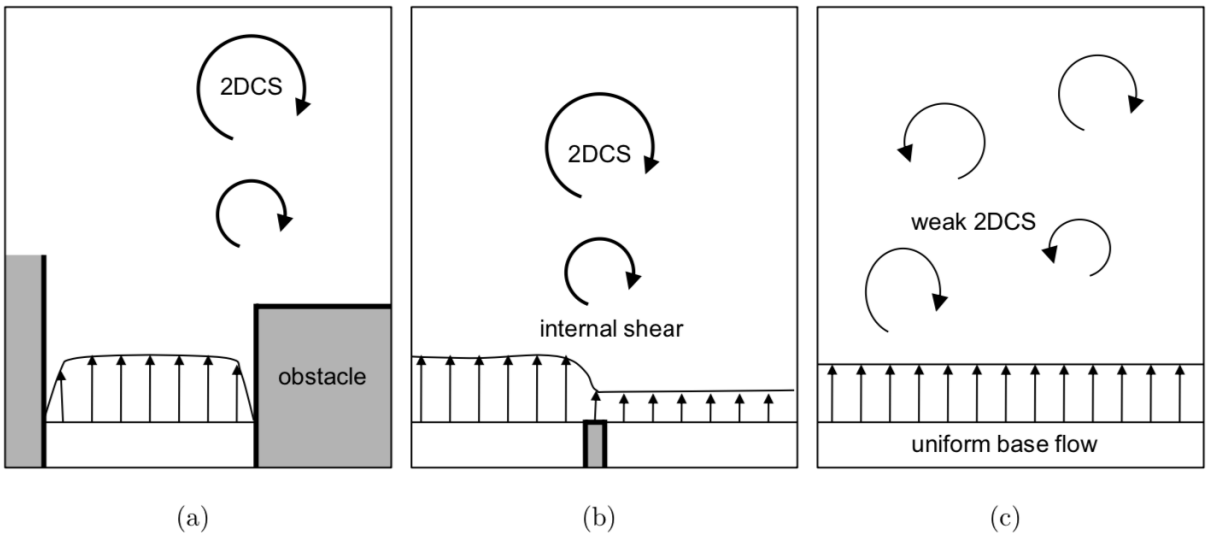

Figure 2.1: Illustration of the principles of three generation mechanisms for 2DCS (Jirka, 2001): (a) Topographical forcing, (b) internal transverse shear instabilities, and (c) secondary instability of the base flow.

The generation of 2DCS always require a certain travel time or distance from the origin of formation. Dracos et al. (1992) describes two processes that govern the growth of 2DCS. Pairing of separate structures leads to larger structures, in which the 2DCS grow larger in time. They also grow by the turbulent vortices that entrain or engulf the less turbulent adjacent ambient fluid. The enstrophy cascade leads to a k^{-3} distribution of turbulent kinetic energy as the rotational momentum is constant among the different vortex scales (see Appendix B). Far from the origin of generation, the large structures lose energy by bottom friction and eventually decay. The maximum eddy size λ found in shallow flows is limited, because energy dissipation scales with the size of the structures. Jirka (2001) indicates a theoretical upper limit of $\lambda_{max} = 2h/c_f$ (c_f being a friction coefficient), after which the 2DCS lose their rotational energy within one turnover.

2.2.2 Shallow jets

At either side of the Roompot inlet a jet develops of which its direction depends on the stage within the tidal cycle. A jet is formed when a fluid enters a stagnant environment of the same fluid (Nieuwstadt et al., 2016), decelerating the jet by exchanging momentum with the stationary ambient fluid. Large areas of horizontal shear are induced by the velocity difference between the jet and the adjacent flow. For shallow jets, Dracos et al. (1992) studied various regions of development based on the ratio of eddy traveling distance x and water depth H (Figure 2.2). In the "near field" region ($x/H < 2$), the flow behaves like a classical 2D jet not yet affected by the shallowness of the flow. The "intermediate field" ($2 < x/H < 10$) is characterized by secondary currents that affect the jet flow over the whole depth. The vertical velocity distribution is strongly non-uniform, with maximum velocities found near the bounding surfaces. The term "far field" refers to distances greater than about 10 times the water depth. Here, the jet is dominated by counter-rotating vortices and the secondary currents found in the near field are damped out. The mean velocity is

approximately uniform in the x-direction with only weak boundary influence. The mean flow and turbulence structures have a 2D character. 2DCS are well developed and eventually dissipate due to bottom friction.

The shape of the shallow jet observed at the the Roompot inlet deviates from the classic profile of a free turbulent jet shown in Figure 2.2. Lateral spreading is affected by the geometry of both the barrier and estuary, limiting lateral growth in streamwise direction. Also, the tidal waters do not flow through a single opening, but instead enter via separate sluices. As will be discussed later in this chapter however, many of the jet's characteristics resemble those introduced here.

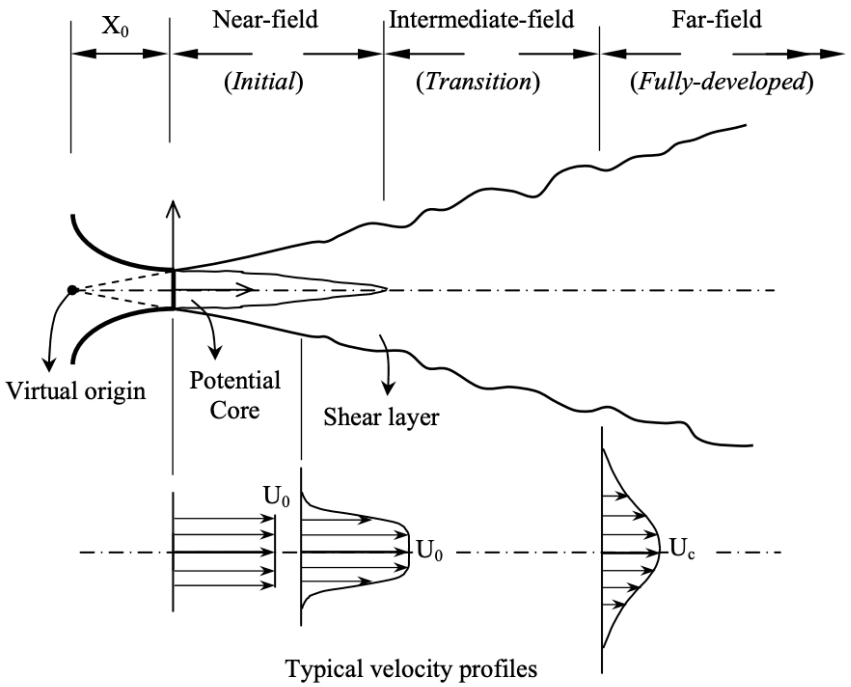

Figure 2.2: Schematic plan view of a free turbulent jet describing the different segments in streamwise direction (Abdel-Rahman, 2010).

2.2.3 Shallow mixing layers

A velocity disparity between two different layers of fluid produces shear stress at the interface of the layers. Infinitesimally small disturbances tend to grow in amplitude as a result of hydrodynamic instabilities. Transverse shear layers between contiguous flows of different velocity lead to the development of a mixing layer. Well defined examples can therefore often be found at either side of a jet. Similar to jets, mixing layers are considered shallow when the size of the largest turbulence structures is smaller than the width of the flow geometry, but significantly exceed the water depth. The 3D nature of turbulence is therefore confined to the horizontal plane only. Turbulence in a shallow mixing layer can be characterized by two different length scales: (i) the large length scales, with an order of magnitude the size of the width of the mixing layer, and (ii) the small length scales, with an order of magnitude the size of the water depth.

Turbulence at the bed is capable of transporting mass and momentum in vertical direction related to the small length scales. The velocity gradient over the mixing layer is important for its growth and retention. The horizontal vortices associated with the large length scales can be much greater than the water depth

and determine the horizontal transport by turbulence. The flow outside the mixing layer is not influenced by the mixing layer. The mean streamwise velocity on the high and low velocity side are denoted with u_1 and u_2, respectively. The flow outside the mixing layer defines the mean velocity in the center of the mixing layer ($u_c = (u_1 + u_2)/2$). The width of a mixing layer is then related to the velocity gradient via

$$\delta = \frac{\Delta U}{(\partial \bar{u}/\partial y)_{max}}, \tag{2.2}$$

where ΔU is the velocity difference $\bar{u_1} - \bar{u_2}$ between the two layers. Modeling the mean streamwise velocity field in a mixing layer is often performed under the assumption of self-similarity (Chu and Babarutsi, 1988; Uijttewaal and Booij, 2000). In a self-similar flow the lateral profiles of the streamwise velocity and the Reynolds stress can be described by a shape function, which is made dimensional with a typical length scale and velocity scale which may vary in downstream direction. A variety of functions can be considered, e.g. the error function or hyperbolic tangent. Van Prooijen (2004) found the latter function to fit their data well. The mean flow field is then approximated by

$$u(x, y) = u_c(x) + \frac{\Delta u(x)}{2} tanh(\frac{y - y_c(x)}{\frac{1}{2}\delta(x)}). \tag{2.3}$$

By using a profile function, the two-dimensional formulation is reduced to a formulation depending on the downstream position (x) only. The downstream development of the velocity difference Δu, the velocity in the center of the mixing layer u_c, the transverse position of the center of the mixing layer y_c, and the mixing layer width δ.

Characteristic properties of the shallow mixing layer are the downstream decrease of the velocity difference, the decreasing growth rate of the mixing layer width and the shift of the center of the mixing layer to the low velocity side. Following Chu (1983), the velocity difference $\Delta u(x)$ is expressed as

$$\Delta u(x) = \Delta U_0 exp(-\frac{2c_f}{h}x), \tag{2.4}$$

where ΔU_0 denotes the velocity difference at the inflow. Following the derivation by Van Prooijen (2004) using the shape function and the concept of self-similarity, the development of the mixing layer width can be derived:

$$\frac{d\delta}{dx} = \alpha\lambda, \tag{2.5}$$

in which λ is the relative velocity difference between two streams ($(\bar{u_1} - \bar{u_2})/(\bar{u_1} + \bar{u_2})$) and α is an experimentally determined spreading coefficient. Substitution in the velocity difference ΔU from Equation 2.4 and integration with respect to x leads to

$$\delta(x) = \alpha\frac{\Delta u_0}{u_c}\frac{D}{2c_f}(1 - exp(-\frac{2c_f}{h}x)) + \delta_0 \tag{2.6}$$

The initial width δ_0 is imposed by the thickness of the boundary layers that have developed and is approximately $\delta_0 \simeq h$.

In shallow mixing layers, the increase in width is smaller than for a free mixing layer because of the effect of bottom friction on the large structures. The conditions for self similarity are not fulfilled since the velocity difference between both sides of the mixing layer is not constant anymore due to friction. Hydrodynamic

instabilities as well as the growth of the mixing layer are suppressed by the energy dissipation by bottom friction. In contrast to a free mixing layer, λ in shallow mixing layer varies and depends on the rate of energy loss by bottom friction. In the development of a mixing layer, two regions can be distinguished:

1. Linear growth in the area where $\delta < H$. Energy dissipation by bottom friction is limited
2. Growth reduction where the horizontal length scale of the vortices are greater than the water depth. Bottom friction has a stabilizing effect on the large vortices and prevent them from growing.

2.2.4 Stability analysis

In 3D, the turbulence regime of shallow flows is governed by the ratio between advective and viscous forces, which is expressed by the Reynolds number Re. In the corresponding quasi-2D cases, bottom friction is more important than (molecular) viscosity. At scales larger than the water depth, transverse shear enhances the development of Kelvin-Helmholtz instabilities while the bed friction suppresses it. Ingram and Chu (1987) proposed a stability parameter, S, to define the ratio between the rate of energy gained by the work done by transverse shear, and the energy loss by bottom friction. It is generally expressed as

$$S = c_f \frac{L}{h}, \tag{2.7}$$

where h is the water depth, c_f is the bottom friction coefficient, and L is the width of the shear layer. This parameter is widely adopted because it is both convenient to estimate and emerges from linear stability analyses. Large scale instabilities develop when $S \ll 1$, i.e. when bed friction is dominated by transverse shear. Their development is constrained by the double cascading of energy and enstrophy. For a shallow mixing layer, Equation 2.7 is written as

$$S = \frac{c_f}{2\lambda} \frac{\delta}{h}, \tag{2.8}$$

Stability analyses have proven the existence of a critical value S_c. For $S \ll S_c$ the bottom friction has negligible effect and the growth of the instabilities in the mixing layer is not hindered. In case $S > S_c$ the growth of instabilities is impeded by bottom friction and its associated additional dissipation. The fast stream experiences a larger friction than the slow stream resulting in a decrease of the velocity difference with downstream distance. The growth of the mixing layer width will therefore be affected by the bottom friction in two ways. First the decreasing velocity difference leads to a decreasing value of λ and in principle to a decreasing growth rate. Second, the hydrodynamic (Kelvin–Helmholtz) instabilities that govern the mixing layer growth are suppressed by the bottom friction. Field observations, laboratory experiments and numerical studies have all been consistent in the spatial development of instabilities: they arise near the point of generation of the shear layer, then grow in scale with distance downstream over a certain region and eventually disappear. The growth of the shear layer is attributed to the increase in S up to the point where $S > S_c$. Downstream of this location, all large scale instabilities are damped and the 2DCS eventually disappear due to energy loss. Analyses on hydrodynamic instabilities are required to understand the sequence of generation, growth and decay of 2DCS. A linear stability analysis is often applied in studies devoted to shallow flows (van Prooijen and Uijttewaal, 2002; Ghidaoui et al., 2006; Socolofsky and Jirka, 2004). Using this approach, small perturbations are superimposed on a depth-averaged mean

flow field that is supposed to be in equilibrium Figure 2.3. A normal mode solution is applied to obtain linearized shallow-water perturbation equations. Higher order terms are eliminated via dimensional analysis. This system of equations can be studied as a generalized eigenvalue problem, the solution of which are the spatial or temporal growth rates of the perturbations. Using these solutions, the streamwise development of the total turbulence energy contained in the perturbations is computed.

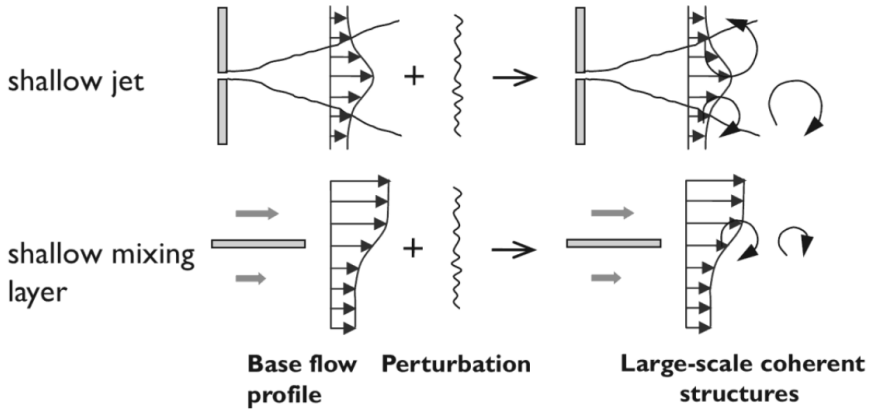

Figure 2.3: Perturbations to the shallow jet and shallow mixing layers leading to downstream 2CDS.

Most of these analyses consider a horizontal bed and are therefore relatively easy to conduct. Broekema (2020) included a varying bathymetry to account for the effect of a slope on the growth rate of stabilities both in laboratory cases as well as in the flow around the ES-SSB. It was determined that the presence of a streamwise slope leads to an enhanced maximum growth rate, both through a direct geometric forcing of the horizontal vortices and through streamwise change of the longitudinal mean flow velocity of perturbations. Therefore, the presence of a slope may lead to a larger turbulence length-scale. In their research, they found the growth rate as function of the wave number to diminish for larger distances, consistent with previous conclusions in this section. However, growth rates of perturbations towards the deepest point of the Roompot scour hole were demonstrated to be several orders of magnitude smaller than for experimental cases. This is related to the relatively large mixing layer width and a smaller longitudinal change of the streamwise velocity. For the field application, only growth of perturbations with $\mathcal{L} > 40$ m was observed. This length scale corresponds more or less to the distance between two subsequent pillars of the barrier, a feature that will be further discussed in Chapter 5. The phenomena and interactions covered here may have significant implications for the resulting bed shear stress. The impact of enhanced growth of perturbations adds to the impact that a streamwise bed slope has on the mean flow field, and the corresponding impact on the hydraulic loading.

2.2.5 Quantification of large-scale flow characteristics in environmental flows

Although many of the described characteristics and flow patterns are present at the Roompot inlet, quantification of 2DCS in an environmental flow is often not trivial. Large spatial and temporal variations of the flow induced by the tide and geometry of the area give rise to many complex flow phenomena not yet well understood. A description of flow patterns found at the Roompot inlet is therefore the topic of the next section, after which details on a new data campaign are provided in the following chapter. Before the

discussion proceeds however, this section first concludes with an overview of flow characteristics that are expected to be measured using RSIV and ADCP.

Since advective processes are governed by the large scale motions, the integral time and length scales introduced in Section 2.1 are important for processes such as turbulent diffusion and transport of momentum. It would thereore be useful to somehow estimate these scales at the Roompot inlet. One possibility is to consider the autocorrelation. The macro scale $\mathcal{T}$ is related to the time scale of large turbulent structures and can be determined by integrating the autocorrelation function between velocities of a certain time interval:

$$\mathcal{T} = \int_0^\infty R(\tau) d\tau, \tag{2.9}$$

where τ is the time interval (lag) and R the autocorrelation function is expressed as (Uijttewaal, 2002)

$$R_{v'(t_0)v'(t_0+\tau)} = \frac{\overline{v'v'}(t_0;\tau)}{\sqrt{\overline{v'^2(t_0)v'^2(t_0+\tau)}}}. \tag{2.10}$$

Specifically, the autocorrelation function describes the correlation between velocity values separated by various time lags and is therefore by definition 1 for τ=0. The rate at which the correlation function decreases with increasing time shifts indicates to what extent the fluctuations are associated with coherent motions. The time and length scales are coupled by means of Taylor's hypothesis of frozen turbulence (Taylor, 1938). Underlying this hypothesis are certain assumptions that should be carefully considered:

- The flow has a large mean velocity component in a well defined direction. The measured time series can then be considered as a spatial distribution of velocity fluctuations along a stream line.
- Eddies do not change during the passage time of the velocity measurement, and the fluctuation caused by the coherent motions does not affect the transport velocity significantly.

Observations of these motions might add to the discussion on e.g. developing shear instabilities and vortex shedding, both of which were treated in the previous sections. An overview of all relevant flow characteristics that can potentially be observed with the aid of RSIV and ADCP are given in Table 1.

Table 1: Overview of expected flow characteristics to be observed using RSIV and ADCP. Details on the measurement campaign is the topic of Chapter 3.

Observation	**RSIV**	**ADCP**
Jet-like flow structure	x	x
Mixing layer development	x	x
Whole-field estimates	x	
Horizontal gradients	x	x
Eddies	x	x
Temporal flow field evolution	x	x
Vertical velocity profile		x
Recirculation zones		x

2.3 Flow observations near the Roompot inlet

The discussion so far is an important step towards understanding the relevant processes that occur near the Roompot scour hole. The chapter continues with a description on how the theoretically derived results are related to flow observations in the corresponding area. Research by Broekema (2020) was carried out near the Roompot scour hole in an attempt to relate the observed flow patterns to the ongoing scour. Their observations form the basis of the discussion on scour hole development in the next section, and are therefore reviewed first.

2.3.1 Description of major flow patterns

The exchange of water between the North Sea and the Eastern Scheldt has profound implications for the flows at either side of the Roompot inlet. The partial blockage by the barrier leads to a maximum water level difference of approximately 1 m between the sea- and landward side. Flow velocities through the inlets can reach up to 4 ms^{-1} and higher (Bijlsma et al., 2017). Broekema (2020) distinguishes three primary features that occur during flood conditions, illustrated in Figure 2.4. The deepest part of the scour hole is located at (1), where water depths locally reach up to 60m (see also Figure 1.1c). Position (2) indicates a circulation zone, induced by the lateral velocity gradient between the fast flowing current and the adjacent ambient fluid. This lateral shear will induce lateral transfer of streamwise momentum, which is usually accounted for by means of large-scale vortices. This lateral momentum transfer, combined with conservation of mass eventually gives rise to a region of fluid recirculation. The strongly contracted flow through the barrier indicated by (3) shows characteristics of a jet.

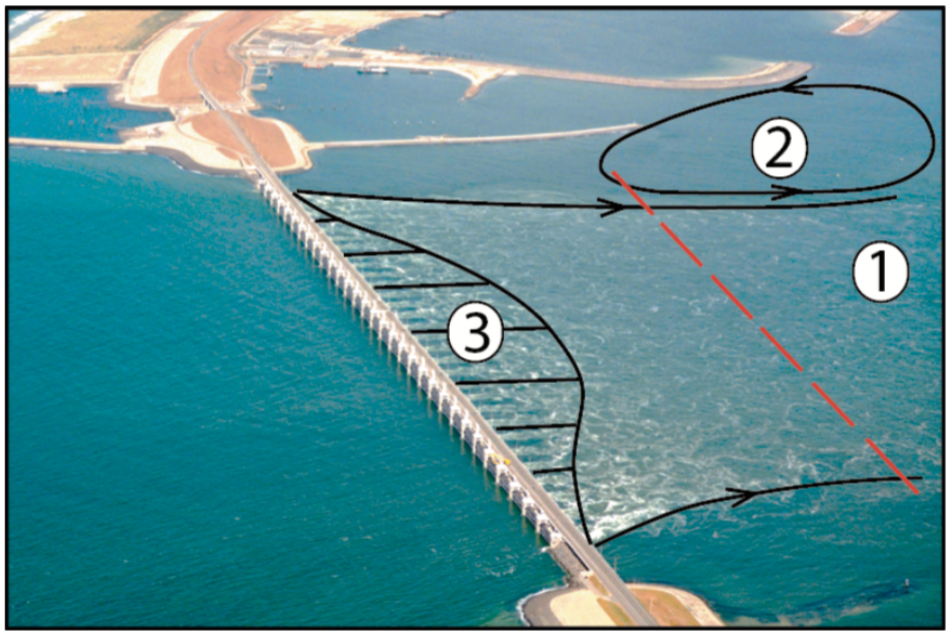

Figure 2.4: Aerial photograph of the flow at the Roompot inlet of the ES-SSB during maximum flood flow, looking to the Northeast. The red dotted line denotes the edge of the bed protection. The flow through the barrier is strongly contracted. Boils are generated from flow separation at the barrier piers. Location (1) indicates the deepest part of the scour hole where maximum contraction is found. The absence of foam in the region adjacent to the main flow indicates that a recirculating motion is present at (2). The outflow from the barrier is schematized as a jet (3). (Broekema (2020)).

Large variations across the three flow patterns exist and become particularly evident when the data analyses performed by Broekema (2020) over the area are examined. Depth-averaged velocities over the Roompot scour hole were measured and interpolated across four transects ($R_1 - R_4$) during three different stages within a tidal cycle: about 1.5 hours after slack tide (T_1, Figure 2.5a-b), at maximum flood (T_2, Figure 2.5c-d) and one hour after maximum flood (T_3, Figure 2.5e-f). R_1 - R_4 correspond to the sailed transects over the domain. For transect $R3$ crossing the scour hole in an east-west direction, the vertical velocity structure of the flow during stages T_1 and T_2 are plotted in Figure 2.6. In the following the most important results from the data analysis is summarized:

- At T_1 the lateral variability of the flow is limited, and flow lines above the scour hole are approximately straight (Figure 2.5a-b). The figure also shows a developing large-scale horizontal recirculation zone in the area north of the scour hole. The vertical velocity profile depicted in Figure 2.6 resembles the structure found in 2D scour hole experiments performed by e.g. Stenfert (2017), Guan et al. (2014), and Koopmans (2017). A return current at the upstream edge of the scour hole develops as a vertical circulation zone is induced by separation of the flow.

- During maximum flood conditions at T_2, the horizontal circulation zone has increased in y-direction and stretches further south (Figure 2.5c-d). Flow velocities are maximum and streamlines are converging towards the deepest part of the scour hole, causing the flow flow to become more non-uniform. In contrast to T_1, streamwise reduction in depth averaged velocities is less evident. The vertical structure

of the flow is significantly different from that at time T_1. Flow separation is suppressed and return currents are absent, leading to a much more uniform flow.

- At time T_3 (Figure 2.5e-f), the horizontal extent of the recirculation zone has increased compared to time T_2. Its dimensions are now maximum in both $x-$ and $y-$direction. Since the streamlines are still strongly converging over the scour hole's centre, relative horizontal velocity differences continue to persist that affect the horizontal non-uniformity of the flow. Although less apparent than during maximum flood, the flow velocity in front of and above the scour hole is still larger than elsewhere in the domain.

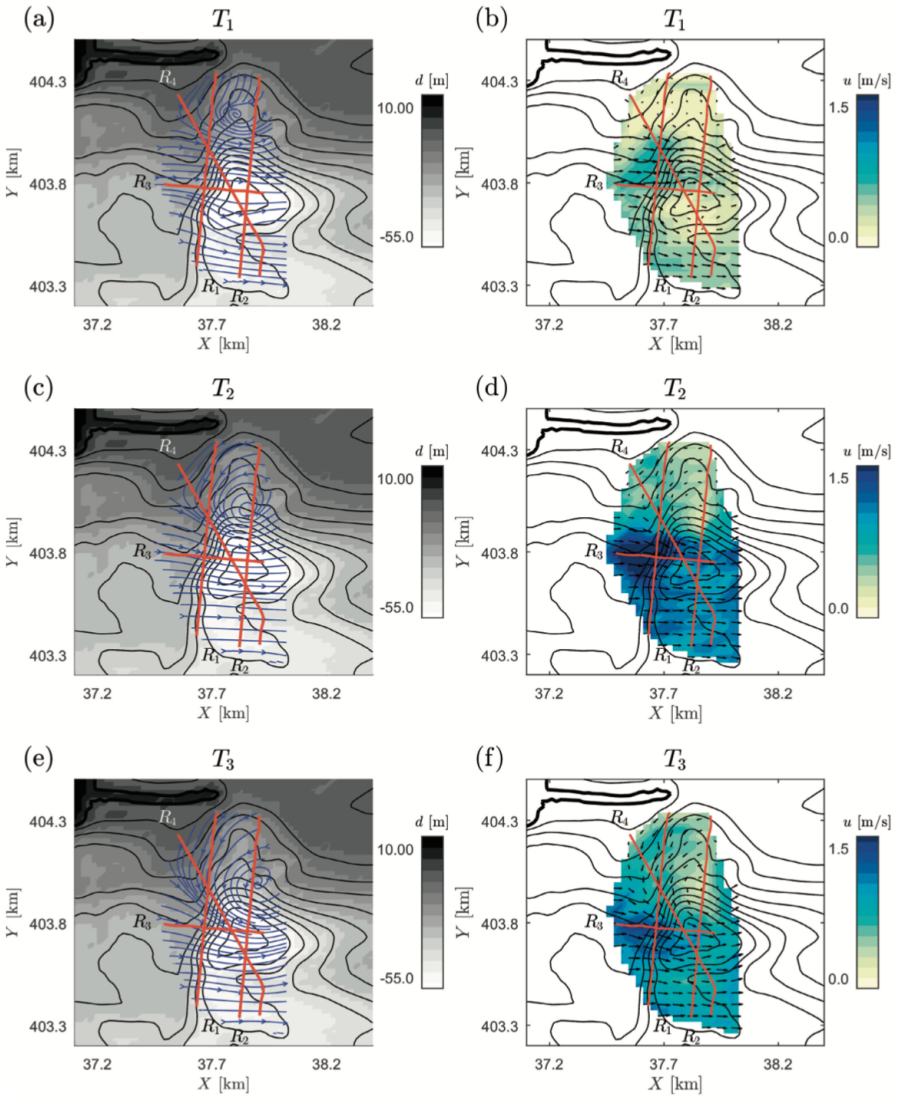

Figure 2.5: Streamlines (left panels) and depth-averaged velocity magnitude (right panels) at the Roompot inlet for three different stages of the tidal cycle: 1 hour before maximum flood (a-b), at maximum flood (c-d), and 1 hour after maximum flood (e-f). R_1 - $R4$ are the transects over which velocities were measured. (Broekema (2020)).

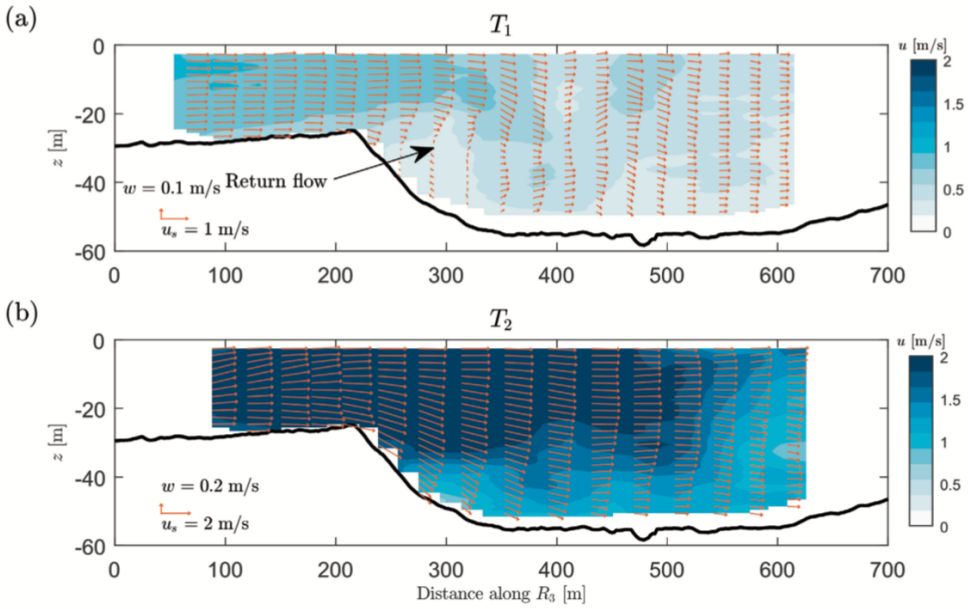

Figure 2.6: Flow in the x, z-plane along transect R3 at the Roompot inlet at time T1 (a) and T2 (b). The colourmap denotes the velocity magnitude (Broekema (2020)).

.

2.3.2 Analysis of flow observations

As the water level difference between the sea and basin-side becomes larger, velocities increase and the flow becomes laterally more non-uniform. Streamlines start to show a contracting behaviour towards the deepest part of the scour hole. When velocities increase further, vertical flow separation is suppressed and the flow remains attached to the bed. This is not expected for steep slopes, where an abrupt deceleration of the flow normally leads to vertical separation of the boundary layer (Guan et al., 2014; Stenfert, 2017; Ghodsian and Vaghefi, 2009). This phenomenon may be explained by additional acceleration of the flow resulting from conservation of potential vorticity. Following Broekema (2020), the conservation of potential vorticity is derived from the 2D shallow water equations, and the acceleration equation for the depth-averaged vorticty. This leads to the following expression:

$$(\frac{\partial}{\partial t} + \bar{\mathbf{u}} \cdot \nabla)(\frac{\omega + f}{d}) = 0. \tag{2.11}$$

Here, f is the Coriolis force induced by the rotation of the Earth. Assuming $f \ll \omega$ and local accelerations are relatively small for the domains considered, Equation 2.11 can be reduced to

$$\tilde{u}\frac{\partial}{\partial x}(\frac{\omega}{d}) + \tilde{v}\frac{\partial}{\partial y}(\frac{\omega}{d}) = 0, \tag{2.12}$$

where $\tilde{u}$,$\tilde{v}$ are the depth-averaged velocity components in a (x, y) coordinate system. From Equation 2.12 it follows that if the water depth is assumed to be uniform, vorticity increases proportionally to the relative depth increase. If the lateral velocity is assumed to be small, the vorticity is mainly determined by the lateral gradient of the streamwise flow velocity. As the water depth increases, flow contraction occurs as

larger streamwise gradients in the flow are present. The flow may experience an additional acceleration that counteracts the adverse pressure gradient which would normally result in vertical flow separation (Broekema, 2020). Their experiments have shown that a lateral velocity gradient, obtained by a horizontal contraction in the flow, can indeed counteract flow separation on downward slopes up to 1:2. Similar conclusion were drawn from experiments on jet behaviour in longitudinal deepening shallow flows (van de Zande, 2018) and on non-uniform flow fields behind a lateral expansion (Üşenti, 2019). The increase in vorticity induced by larger lateral velocity gradients gives rise to increased internal shear within the flow. The changing non-uniformity of the flow over the tidal cycle therefore also provides a feasible explanation of how the horizontal recirculation zone is evolving. The cyclic variations in lateral uniformity have profound implications for the turbulence intensities and subsequent mixing of mass and momentum. In the next section, the relevance of vertical flow separation and horizontal mixing on the development of scour holes is therefore evaluated.

2.4 Scour hole development

2.4.1 2DV scour

The large flow accelerations and velocity gradients associated with the tidal flow moving through the Roompot area induce additional bed shear stress at either side of the barrier. This hydraulic parameter is often expressed in terms of a friction velocity as the two quantities are related via the following expression:

$$\tau_b = \rho u_*^2, \tag{2.13}$$

in which τ_b is the bed shear stress, and u_*^2 is the friction velocity. The friction velocity is the characteristic velocity scale in the near-bed region of a flow, and is linked to turbulent structures near the bed. Much research is devoted to better understand and predict scour hole development, and literature is especially rich in studies on 2D-vertical geometries (e.g. Stenfert (2017); Guan et al. (2014); Koopmans (2017); Hoffmans and Booij (1993)). Figure 2.7 schematizes the distinct zones that are often classified. Initial scour develops when (local) bed stresses are sufficiently large for sediment transport to exceed sediment supply. For gentle upstream slopes of the scour hole up to about 7°, the flow is able to stay attached to the bed (Chandavari and Palekar, 2014). Steeper slopes cause the flow to separate, creating a circulation zone up to the location where flow reattaches. The results in these studies all satisfy the principle of mass conservation, where increasing flow depths induced by scour lead to a reduction in flow velocities. Consequently, bed erosion ceases to continue when the flow velocity reaches a certain erosion threshold. As a result, the hydraulic loading on the bed continues to decrease, until the equilibrium scour hole configuration is reached.

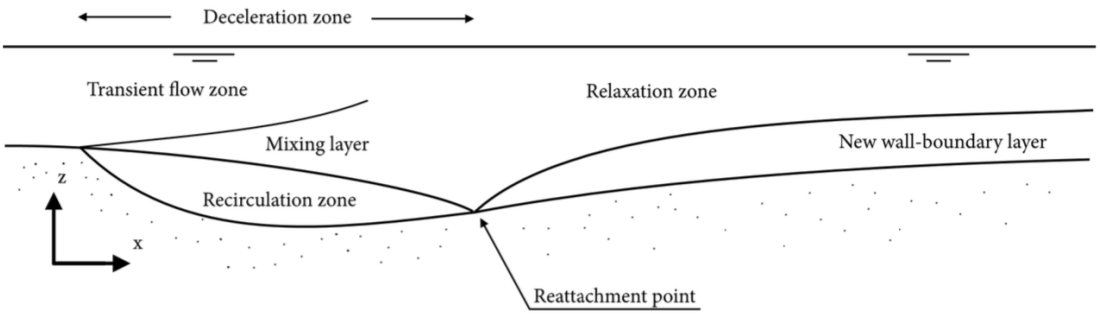

Figure 2.7: Flow conditions in a 2D-vertical scour hole. Based on Hoffmans and Booij (1993).

.

Many expressions for equilibrium scour depths exist (e.g. Hoffmans and Verheij (1997); Breusers (1966)). As they were experimentally derived using a variety of (mostly) 2D configurations, none of them are conclusive for the Roompot scour hole considering the complex flow and geometry of the area. Nevertheless, such an expression was used for the design of the bed protection. It now appears that the equilibrium depth has already been reached. Regularly carried out measurements at the scour hole however indicate that scour is still an ongoing process. The 2D feedback mechanism that was described becomes different when the three-dimensionality of the flow phenomena are taken into account.

2.4.2 3D scour holes

For a developing scour hole in horizontal shear flows, flow convergence in combination with vertical attachment may persist. Depending on the upstream lateral gradient in streamwise velocity, the flow velocity and hydraulic loading are consequently considerably larger than for horizontally uniform flow fields. In the previous section it was mentioned that high flow velocities not sufficiently counteracted by pressure gradients for flow separation to occur induce high turbulence intensities at the bed of the scour hole. This is also evident from the non-linear relation between bed shear stress and flow velocity (Equation 2.13). As a result, lateral mixing of mass and momentum may be enhanced. In contrast to the 2D-vertical scour hole examples therefore, a positive feedback loop in the presence of the scour hole induces further development. This is particularly evident at the eastern side of the inlet adjacent to the applied bed protection. Here, scour holes have locally reached depths to up to 60 m with respect to the water surface, associated with roughly 40 m of scour. This scour can be classified as clear water, edge scour; the barrier effectively blocks sediment input, and the bed protection is geometrically closed, (e.g. no sediment can be eroded from under the layers of rock).

Broekema (2020) demonstrated the differences in scour hole development for laterally uniform (Case I) and laterally non-uniform flows (Case II) in a laboratory experiment. Flow velocity and turbulence properties were measured using acoustic Doppler velocimetry (ADV), capable of measuring the full 3D velocity time-series. Figure 2.8 compares the scour geometry at the end of the test for both Case I (upper panel) and Case II (lower panel). Maximum scour depths for the laterally non-uniform case did not correspond to locations where peak velocities were greatest. Instead, they were found in the shear layer where the lateral component of the Reynold stress, $\tau_{xy} = \overline{u'v'}$, was largest. The scour depth at the end of Case I is more or less uniform

over the width of the flume, and the peak of the lateral shear stress tended towards the center of the jet. This jet converges in the horizontal plane as the scour depth increases.

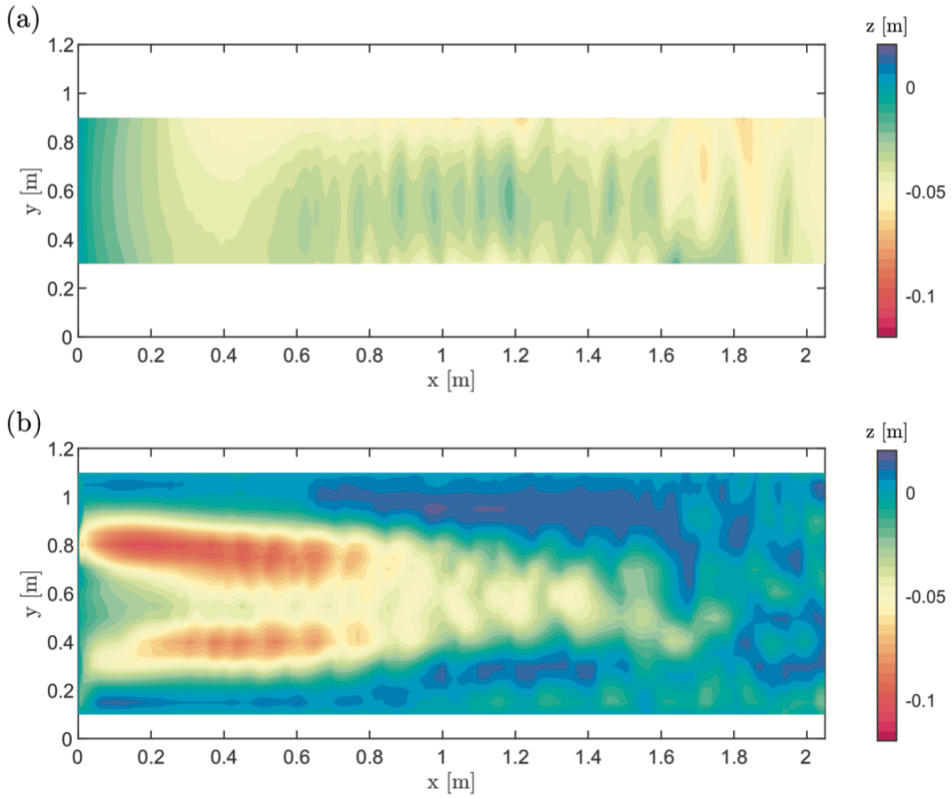

Figure 2.8: Final scour depth in experimental cases for (a) a laterally uniform flow, and (b) a laterally non-uniform flow (Broekema, 2020).

Similar behaviour was found during the experiments carried out by Üşenti (2019), who demonstrated that horizontal flow structures in flows with lateral velocity gradients are indeed affected by the scour hole. They observed a shift of the center of the mixing layer towards the high velocity region in the scour hole. The results from both studies indicate that maximum scour depth is not necessarily attributed to the maximum flow velocity, but rather to additional disturbances of the boundary layer by the large-scale lateral motion. It is likely that turbulence intensities here are increased, leading to enhanced mixing and larger near-bed gradients. The associated bed shear stresses have a higher potential for scour. The depth of the Roompot scour hole is therefore controlled by a feedback mechanism between developing lateral shear and flow contraction that becomes more important as the scour hole develops.

2.5 Conclusions

Theoretical description of shallow flows

This chapter covered the fundamental aspects of shallow flows and its implications for large-scale flow structures found at the Roompot inlet. Flows are characterized as shallow when the horizontal length scales

greatly exceed the vertical one. The onset of turbulence and the double energy cascading are important concepts within this thesis' framework. They help to understand the development of large coherent structures in quasi-2D flows, of which the shallow jet and the shallow mixing are the two major structures found around the Roompot scour hole. Transverse shear layers between contiguous flows of different velocity lead to the development of a mixing layer. Similar to jets, mixing layers are considered shallow when the size of the largest turbulence structures is smaller than the width of the flow geometry, but significantly exceed the water depth. The 3D nature of turbulence is therefore confined to the horizontal plane only. Characteristic properties of the shallow mixing layer are the downstream decrease of the velocity difference, the decreasing growth rate of the mixing layer width and the shift of the center of the mixing layer to the low velocity side.

The sequence of generation, growth and decay of 2DCS can be understood by performing linear analysis on hydrodynamic instabilities in the flow. Maximum growth rate is enhanced by the presence of a streamwise slope by two mechanisms: through a direct geometric forcing of the horizontal vortices and via streamwise change of the longitudinal mean flow velocity of perturbations. The increased growth rates of these perturbations add to the impact that a streamwise bed slope has on the mean flow field, and the corresponding impact on the hydraulic loading.

Flow analysis at the Roompot inlet

To apply the theoretical knowledge on shallow flows to flow patterns observed near the ES-SSB, Broekema (2020) quantified the flow field around the Roompot scour hole using ADCP measurements. The cyclic tidal variations continuously affect the horizontal structure of the flow, the implications of which are particularly exposed when the flow structure over different tidal stages is considered. The development of a large horizontal circulation zone and the contraction of streamlines are attributed to these changes in lateral non-uniformity. During contraction, flow separation near the bed of the scour hole is suppressed and high velocity values in the streamwise direction are maintained. The cyclic variations in lateral uniformity therefore affect turbulence intensities and subsequent mixing of mass and momentum.

Scour hole development

The scour hole at the Roompot inlet has not yet an equilibrium yet, but instead is still growing. Expressions that assume a 2DV profile (and thus a lateral uniform flow) underpredict scour depth. It appears that Roompot scour hole is controlled by a feedback mechanism between developing lateral shear and flow contraction that becomes more important as the scour hole develops.

The interaction between large-scale horizontal flow structures and scour development that was stressed in this chapter motivates a further study on flow non-uniformity at the Roompot inlet. Details on a data analysis campaign in which ADCP measurements and drone images over the area are collected is the topic of the next chapter.

3 Field campaign: acquisition and processing of flow data

A field campaign was carried out to collect data at the Eastern Scheldt storm storm surge barrier, near the Roompot inlet. In this chapter a brief overview of the contents of the campaign are described. A full description is shared in Appendix A. The goal of the measurements is to acquire data to (i) study 2D horizontal flow patterns at the water surface, and to (ii) assess the possibilities of applying RSIV over large areas using a drone. To this end, drone images and ADCP measurements were collected during the measurement campaign. Section 3.1 elaborates on the requirements for determining the appropriate time interval to measure the tidal flow in the area. The acquisition of drone images is the topic of Section 3.2, in which the measurement prerequisites and strategies for filming are being discussed. It also covers the post-processing steps of the images required to prepare for the RSIV analysis. The chapter concludes with an explanation and measurement strategy for collecting ADCP data in Section 3.3.

3.1 Time and date of the measurement campaign

As the tidal character of the flow generates large water level differences between either side of the barrier, significant variations in flow velocities exist. The time and date at which the data is to be collected are limited by certain conditions. Most importantly, data acquisition for the purpose of this research can only be performed during the rising tide, when the flow is directed towards the estuary. Additionally, different time intervals between slack tide and maximum flood are considered to study the developing non-uniformity in the flow with increasing flow velocities. Foam and bubbles generated by the contracting flow are also more apparent during high flow velocities. Finally, weather conditions played a role in the decision on an appropriate measurement date. High wind gusts, solar reflection, rain and mist may hamper the drone in filming the water surface. On the basis of these motives, the measurement campaign was scheduled around spring tide on March 1, 2021 between 10 am - 5 pm. Maximum flood conditions were present at around 3 pm. Average wind speeds of 18 ms^{-1} (3 - 4 Bft) and a temperature of 5 - 8 °C were recorded throughout the day. Unforecasted fog and clouds limited filming in the morning and early afternoon, whereas clear sky conditions were present after 2 pm. Filming was therefore only possible around maximum flood.

3.2 Drone measurements and image processing

This section elaborates on the separate elements of which the RSIV procedure is composed of. First, challenges corresponding to the selection of relevant flow locations and the geometry of the area are addressed. Information on GCP configurations and GPS positioning is treated next, followed by a thorough description of the projective transformation between image coordinates and world coordinates. The section concludes with pretreatment of the images and image evaluation using the Matlab toolbox PIVlab.

3.2.1 Measurement locations

Deciding on the geometry of the image and the orientation of the camera with respect to the large water surface is not a trivial task. Prior to the actual fieldwork campaign, the occurrence and locations of the relevant flow phenomena were considered. Satellite images were analyzed to determine the field of view with respect to the observed flow structures. The images also contributed to a better understanding of the dimensions of these flow patterns and the accessibility of the area. Figure 2.4 already illustrated the location of flow circulation near the Roompot scour hole, indicative for large lateral velocity gradients. These gradients are also predicted to be found closer to the barrier at the interface between the fast flowing jet and the adjacent waters, the reason of which follows from Section 2.3. In Figure 3.1, these two locations of expected high shear are schematically drawn and provided a first order approximation of the relevant locations to be filmed.

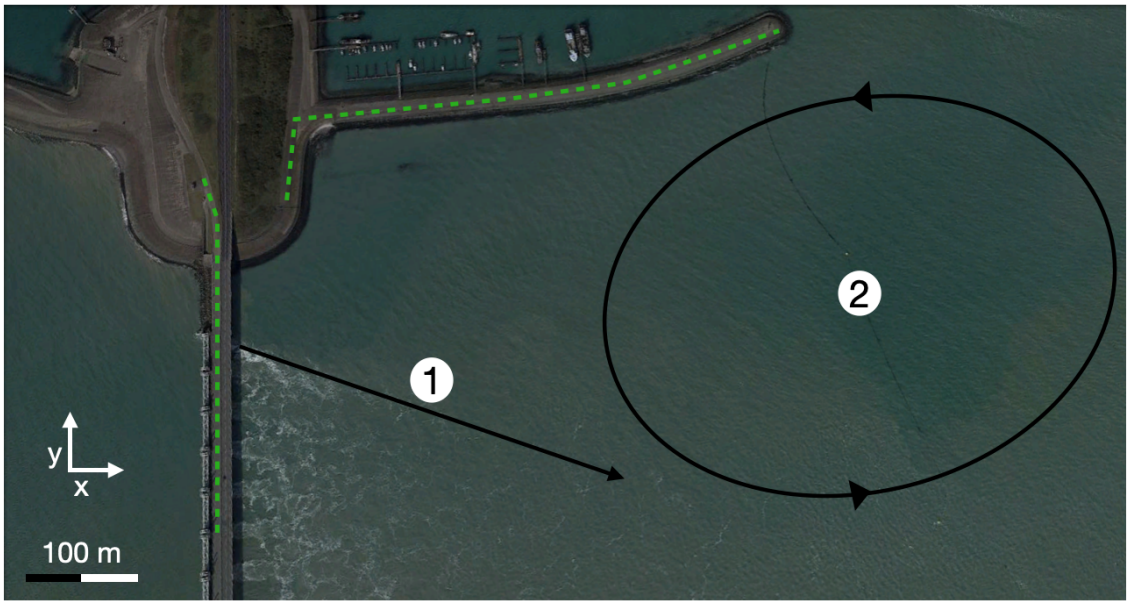

Figure 3.1: Satellite image of the area showing two locations in which large lateral velocity gradients were expected: (1) indicates the interface between the jet and the ambient fluid, whereas (2) includes a recirculation zone. The dotted green line illustrates the areas accessible by foot.

Aside from the dependence on weather and tidal conditions, the acquisition of images over the areas introduces certain challenges that originate from the large distance between the relevant flow phenomena and the solid ground. The following constraints are taken into account in order to decide on the required camera specifications and the actual size of the areas:

1. The coverage of large areas with a drone can be controlled by increasing the elevation and angle under which the camera should film. The penalty for these adjustments is the loss in ground sampling distance, both in an absolute sense as well as for the relative horizontal pixel distance. This loss in spatial resolution makes post-processing of the images more difficult.

2. A sufficient amount of reference points should be visible on each image and measured at great accuracy. These ground control points (GCPs) are required to transform the raw raster images to real spatial

locations using camera projections. Ideally, GCPs should be placed rather uniformly across the area to fully control the accuracy of the transformation in every direction (Zhao et al., 2003). Filming over a vast body of water limits this distribution, and buoys installed on the water surface that could possibly act as GCPs are susceptible to drifting. The only locations where GCPs can be deployed are either on the barrier, or on the dam perpendicular to it stretching into the estuary. For RSIV applications on the scale of large fluvial and coastal processes, where generally a lack of reference points is inevitable, it would be valuable to examine the error ranges for different GCP configurations. Various marker orientations along the margins of the images are therefore considered. To prepare for the different set-ups, laboratory experiments were carried out to examine the quality of the camera projection for different GCP distributions in a controlled environment.

3. Limited amount of natural tracers. To subtract surface velocity vectors from a series of images using correlation techniques, tracers tracked by the RSIV method should be well visible on the water surface. Tracers that were assumed to be suitable for this process are comprised of air bubbles and foam (boils) generated by the contracting flow through the barrier. The large distance between solid ground and these tracers again puts additional constraints on the areas chosen. At location (2) in Figure 3.1, these boils even were fully absent.

No area could be selected that fully complies with the above prerequisites, urging to make concessions to the distribution of GCPs and the region of interest including natural tracers. Perhaps the most obvious candidate for assessing the method's applicability is the area located close to the barrier (Area A). Successful PIV application very close to the barrier (i.e. tens of meters) was already demonstrated by Verbeek et al. (2017). Here, natural tracers are expected to be well visible and GCPs can be distributed along the barrier's axis. A drawback would be the distance from the actual scour hole. The second area chosen (Area B) covers the recirculation zone in the northeastern Roompot area, of which the reasoning follows from the results by Broekema (2020). The sediment plume evident in Figure 3.1 provides an additional motive to study flow processes here. A disadvantage however is the lack of natural tracers to be accurately detected by the autocorrelation algorithms.

Taking all circumstances into consideration, Figure 3.2 shows the two areas that were selected assuming they would yield the most relevant information on the horizontal flow field. Positions of the GCPs, drone and piloting platform for each area are also indicated.

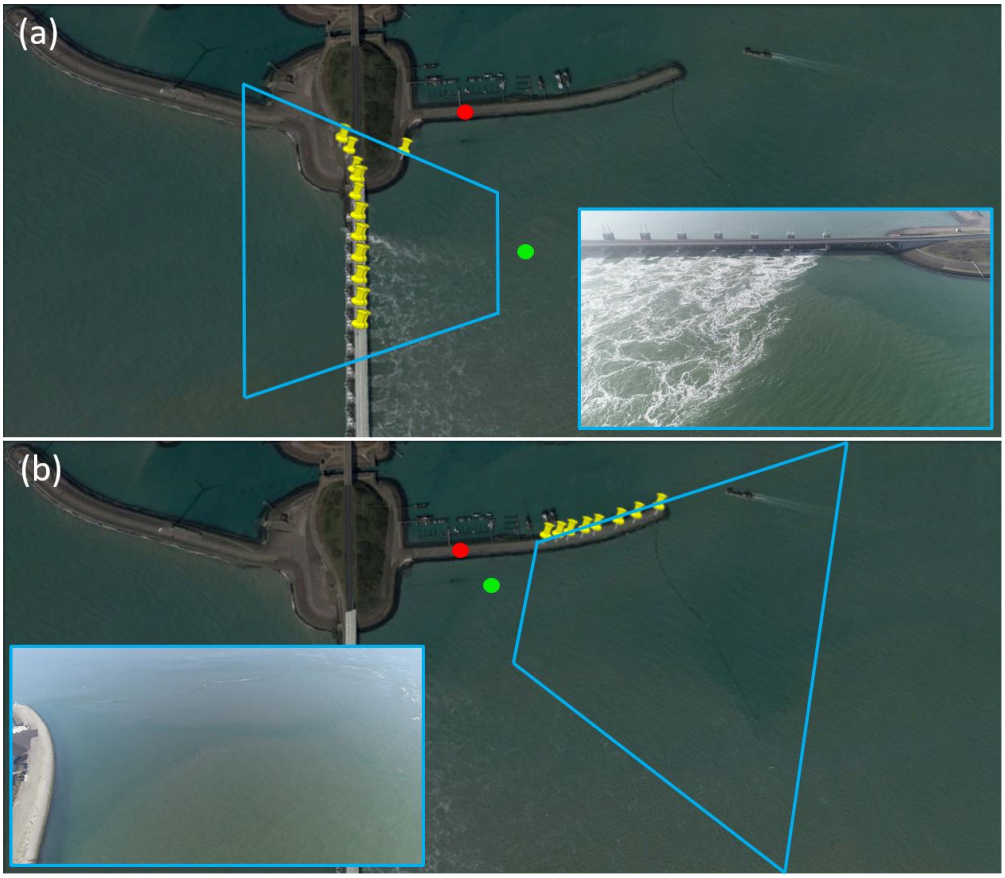

Figure 3.2: Satellite images of the measurement site. The blue boxes indicate the two different areas. Image (a) illustrates the area close to the barrier where the natural tracers and distribution of the GCPs were expected to be well visible on the images (Area A). Image (b) shows the area over the northeastern Roompot scour hole (Area B). The inset photos are taken during the measurement campaign. Yellow pins indicate ground control points. The red dot marks the location of the drone pilot, whereas the green dot indicates the fixed drone position during filming.

3.2.2 Camera requirements and locations of GCPs

For both areas, filming the water surface at large elevations and angles requires a high resolution camera to be mounted on the drone. The drone used is a DJI Phantom 4 Pro 2.0, equipped with a 20 mega-pixel (4096x2160) camera recording at 30 frames per second. It contains a field-of-view of 84° with a focal length of 8.8 mm (35 mm format equivalent) (Zhao et al., 2003). With a mass of 1.375 kg and a 3-axle image stabiliser the drone was capable of filming relatively steady under the recorded wind speeds. The measurements were carried out from a single aerial position to assure the least amount of correction required for post-processing. An entire cycle of ascending, positioning, filming and landing lasted for a duration of 10 - 15 min and was repeated multiple times throughout the day. The flight altitude and camera tilt angle were 120 m and 65°, respectively, to be able to cover the full extent of the areas.

A total of 34 GCPs were deployed along the margins of the areas: 12 on the dam parallel to the channel, 6 close to the N57 roadway and 16 on the bikeway across the barrier, where they are closest to the measurement area and fixed on the solid ground. The markers on the barrier were orientated along the barrier's axis, but some variability in its perpendicular direction was included to anticipate on expected distortion at the

edges of the images. The GCPs on and near the dam were uniquely marked to be easily recognizable and distinguishable. Around the barrier, existing signs and marks on the bikeway provided visible reference points and therefore no additional markings were required (Figure 3.3).

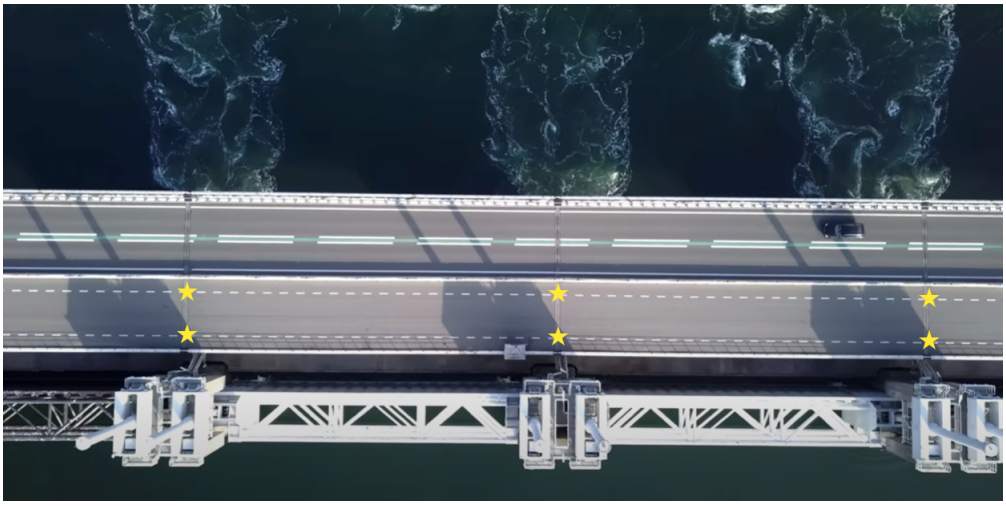

Figure 3.3: Example of measured GCP locations on the traffic markings at the barrier's bikeway, indicated with yellow stars.

3.2.3 GNSS coordinate transformation

Positions of the GCPs were determined using a Trimble R8 GNSS system, capable of receiving signals at dual-frequency, 24 channel GPS, with an integrated GPS antenna and 450 MHz radio-transmitter Bilajbegović et al. (2007). World coordinates were derived using the Netherlands Positioning Services (NETPOS) GNSS products. The system makes use of 31 reference stations with a spatial interval of 40 km (Figure 3.4).

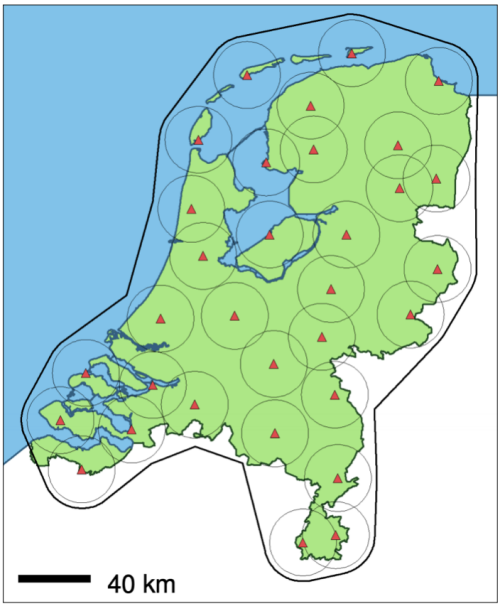

Figure 3.4: Locations and coverage of the NETPOS reference stations (http://euref.eu/).

The services provide GPS and real-time corrections for positioning in the European Terrestrial Reference System (ETRS89). The network is designed to link all reference stations to a central data processing center to obtain optimal calculations Qu (2012). However, rather than creating a real-time link between the GNSS receiver and the NETPOS central station, post-processing steps were taken to determine the position via post-processing kinematic (PPK). This method is more robust as it traces back and forth through the data multiple times to give reliable data correction, providing a precision of the base net better than 1 cm horizontally and 3 cm vertically (Lesparre, 2006). The raw data was converted to Dutch 'Rijksdriehoekscoördinaten' (RD coordinates) linked to the ETRS89 reference systems. All coordinates and their standard deviations are shared in Appendix A. Two out of the 34 measurements were discarded for having a standard deviation in the order of the GNSS precision. For the other markers standard deviations accounted for 0.9 - 1.6 mm.

3.2.4 Image calibration

RSIV in itself provides velocity in pixels per frame rate. To ensure that the tracked displacements between each image pair are solely due to a real displacement of the water surface, every separate image of the sequence must be scaled identically. This implies that for obliquely taken images the dimensions of the image pixels are required to be estimated. Correction for the obliquity of an image is called orthorectification and is a very fundamental step within the overall RSIV process. The transformation procedure between image coordinates and world coordinates using a camera projection is therefore described first. The quality of this transformation primarily depends on the spatial information in the area that can be obtained by GCPs. The challenge of distributing GCPs across the Roompot area was already mentioned in Section 3.2.1, thereby imposing restrictions on the projection accuracy. For this reason, laboratory experiments were carried out prior to the fieldwork campaign to assess the range of expected projection errors. Using a series of GCP distributions similar to those intended to be applied for the field application, GCP configurations at the Roompot inlet were adapted according to the information on the transformation quality. This will be the topic of the concluding part of the section.

Camera projection

The camera projection is solved for by following the routines described by De Vries et al. (2011) and Holland et al. (1997). Typically, image stabilization and orthorectification are done by georeferencing control points in the image that define a transformation matrix. The matrix entries should first be adjusted to eliminate the effects of image distortion caused by lens convexity. These distortions can be modeled and corrected for via

$$\Delta r = k_1 r^3 + k_2 r, \tag{3.1}$$

where Δr is the distortion pixel displacement, k_1 and k_2 are coefficients, and r is the radial distance from the principle point coordinates u_0 and v_0.

The next step is to determine the intrinsic parameters of the camera that are related to its sensor, i.e. the dimensions of the pixels, the camera's focal length and the optical center of the sensor. Although there are more accurate (and considerably more elaborate) methods to determine the intrinsic parameters, the method proposed by Zhang (2000) is used because moderate accuracies (i.e., accuracies to within a single

picture element) are assumed to be sufficient over the large areas considered. First the intrinsic camera parameters including distortion coefficients are stored in project matrix K as:

$$K = \begin{bmatrix} f_u & 0 & 0 \\ 0 & f_v & 0 \\ u_0 & v_0 & 1, \end{bmatrix} \tag{3.2}$$

with s being a parameter that accounts for skew in the charge-coupled device (CCD) array of the camera, and

$$\begin{aligned} f_u &= F * s_x \\ f_v &= F * s_y. \end{aligned} \tag{3.3}$$

Here, F is the focal length (in mm), and s_x, s_y are the horizontal scale factors (in pixel length^{-1}) in the u and v directions, respectively. Estimating the intrinsic parameters often includes an experimental set-up to calibrate the CCD using a number of accurately measured control point observations, using for example a checkerboard imaged from different angles Heikkila and Silvén (1997). Calibrations can be performed using existing tools, such as Matlab's single calibration application or Python-OpenCV. The parameters are generally invariant for a specific lens-camera-image processing system trio and therefore only need to be determined once. The transformation that relates the 3D world coordinates X_i and the corresponding image points x_i, are related through a camera projection matrix according to

$$sx_i = K \begin{bmatrix} R \mid t \end{bmatrix} X_i \tag{3.4}$$

in which t is the translation vector (X, Y, Z), R is the 3x3 rotation matrix describing the orientation of the camera coordinate system with respect to the world coordinate system, and

$$x_i = \begin{pmatrix} u \\ v \\ 1 \end{pmatrix}, \qquad X_i = \begin{pmatrix} X \\ Y \\ Z \\ 1 \end{pmatrix}. \tag{3.5}$$

Equation 3.4 assigns new coordinates to every pixel of the image so that they correspond to the physical space, producing a high level of geometric integrity. Unknowns in the rotation matrix are the pitch (τ), roll (σ) and yaw (ϕ) angles indicated in Figure 3.5.

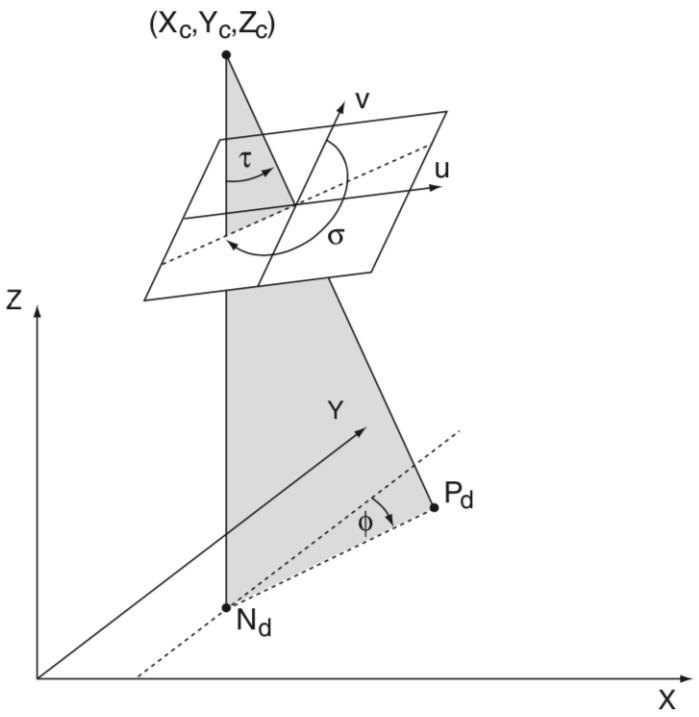

Figure 3.5: Schematic illustration of the collinearity between camera parameters (x_c,y_c,z_c), world coordinates (X,Y,Z), image coordinates (u,v), and rotation angles (ϕ,τ,σ) (De Vries et al., 2011).

With the five intrinsic parameters determined, the second step consists of estimating the extrinsic parameters. This is often done by measuring the camera positions (X_c, Y_c, Z_c), and the camera orientation (σ, τ, ϕ) using perspective-n-point (PnP) (Gao et al., 2003). This algorithm solves for the six degrees of freedom using a non-linear least squares method between the GCPs and the camera. The rotation matrix and translation vector, which represent the coordinate system transformation between world coordinates and camera coordinates, can subsequently be derived from the camera pose. For the Roompot application the PnP solution did not accurately estimate the camera's extrinsics. It appeared that the uneven GCP distribution imposed restrictions on solving for the full camera matrix. A solution is proposed that involves computing the homography matrix H instead, i.e. a geometric transformation matrix is applied to map points on an image to a planar surface. Because of the 2D nature of this projective transformation, all $Z-$coordinates are assumed to be on the same plane with $Z = 0$. The GCPs at the Roompot inlet are positioned at an average elevation of about 10 m above the water surface. It is assumed that projection errors introduced by these height differences are relatively small with respect to the camera elevation. Also, since the scaling factors are now constrained (because on a plane all the points are constrained to lie on a surface, rather than being uncorrelated) Equation 3.4 can be simplified to

$$x_i = HX_i. \tag{3.6}$$

Similar to the PnP solution, the unknown elements of the homography matrix can be solved for with the aid of (at least 4 non-collinear) GCPs. The homography can then be inverted to map from a physical plane to the image plane. Derivations and additional information on the method is provided in Appendix C.

For all camera projection methods, the described transformation from image coordinates to world coordinates assumes that each GCP is positioned at the very same pixel location throughout the entire film record. In reality, some degree of geometric distortion on the raw drone images caused by the wind or vibrations cannot be fully prevented. The effect of such movements is a small continuous variation of the field of view of the camera creating shifts in the coordinates. These shifts caused by rotational and translational motion of camera are not necessarily the same throughout the image. Geomtric distortions unavoidably leads to errors in the camera projection if the same projection is applied to all images. Two solutions for camera shifts are proposed to limit the amount of errors:

1. Break down the record into videos with smaller durations and determine for each record the new approximated image coordinates of the GCPs. The projection matrix for the separate series is recomputed and their averages can be combined to improve the estimate. Although being more accurate, manually searching for new image coordinates in each record is a time consuming task.

2. Auto-detect markers on each image. For the entire record, feature detection algorithms for GCPs may greatly improve the overall camera projection. Auto-detection is very sensitive to errors and requires large contrasting markers to be reliable. For the current application, this technique was not appropriate as the markers themselves shared too many lightning properties with the direct environment, making them poorly distinguishable.

Experimental set-up

Because determining the exact pixel dimensions is so important for the RSIV analysis (to convert between velocities provided in px/frame rate to physical units), the quality of the reprojection to 3D world coordinates is ideally somehow to be validated. In fact, the values of the computed velocity vectors very much depend on the accuracy of the scaling, and the quantification of reprojection errors may greatly contribute to the overall accuracy of the derived velocity field. For the field application, the camera position can only be determined in the range of the GPS accuracy on board of the drone (in the order of several meters both horizontally and vertically). Also, since the markers are placed at the margins of the domain, there is no reference case for which the projection is assumed to be (close to) exact. Prior to the fieldwork campaign therefore, a laboratory experiment was carried out to test the projection on a 2x2 m domain in a controlled environment where a total of 46 markers were placed uniformly over the area and their relative positions known to mm accuracy (Figure 3.6). The camera parameters, including angle and focal length, were kept constant and similar to those intended to be used at the Roompot area. The camera itself was mounted on a platform at an elevation of 1.10 m. The squared domain in this 'base case' set-up is approximately 250 times smaller than the areas for the field application. A 10 m height difference between the markers on the barrier and the dam thus translates to a variation of 4 cm in the experiment. Similarly, lateral variability of 5 m across the bikeway on the barrier is scaled down to 2 cm for the test cases. Throughout a series of tests, various marker configurations were applied to resemble the field cases. To this end, reference points were removed and added along the upper and lateral margins of the images. The different set-ups were then compared to the reference solution to determine the relative importance of marker variability across the domain. One such field configuration that resembles the distribution at the Roompot inlet is shown in the right image of Figure 3.6, where the markers on the x-axis also include slight variability in vertical and lateral directions.

Other set-ups with exaggerated variations in each dimension were also tested to account for the validity of different marker compositions.

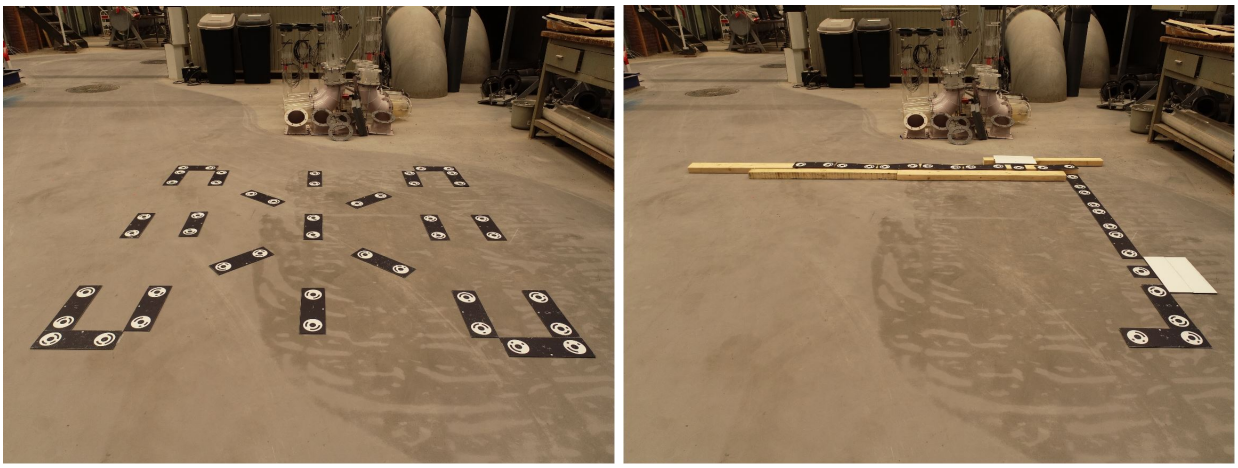

Figure 3.6: Overview of experimental set-up. Left image: the locations of the markers and their distances to the camera are measured accurately to provide a reference solution for various projections. Right image: one of the configurations as was intended to be used at the Roompot inlet.

3.2.5 Image enhancement

Other unavoidable issues in outdoor implementation of RSIV include for example variations in luminosity and contrast due to clouding or reflections. One approach to improve the measurement quality is the enhancement of images before the actual image correlation in the RSIV process takes place (Raffel et al., 2007; Shavit et al., 2007). Figure 3.7 illustrates the applied sequence of enhancing contrast to the raw images. The original RGB color images are first converted to greyscale so that the images carry only intensity information. The contrast between the greyscale images is then increased using the contrast limited adaptive histogram equalization (CLAHE) that was developed to increase the readability of image data in medical imaging (Pizer et al., 1987). CLAHE operates on small regions (tiles) of the image. In every tile, the most frequent intensities of the image histogram are spread out to the full range of values (from 0 to 255). Regions with low exposure and regions with high exposure are therefore optimized independently. CLAHE improves the probability of detecting valid vectors in experimental images by 4.7 $\pm$ 2% (Shavit et al., 2007). In the next step, the mean of each pixel across all images is subtracted from these greyscale values, resulting in a mean intensity that is approximately constant. Other pretreatment methods, such as the application of a high-pass filter or intensity capping, are also tested.

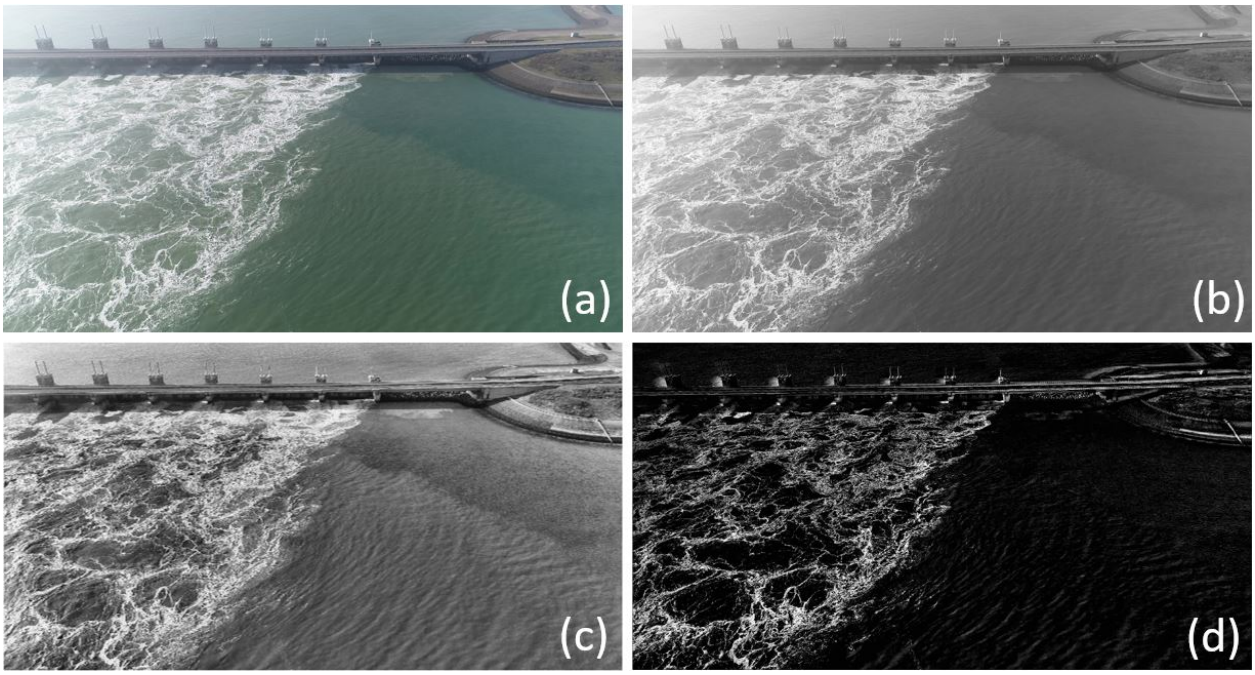

Figure 3.7: Sequence of image enhancement: (a) original RGB images are converted to (b) greyscale, (c) enhanced using CLAHE, and (d) detrended.

3.2.6 Image evaluation

Once the images are detrended and the tracers on the images produce sufficient contrast with their environment, they can be evaluated using RSIV to obtain flow velocity vectors of the water surface. The implementation of the RSIV algorithms is carried out using the Matlab toolbox PIVlab, which is appreciated across many research applications that involve tracking of particles for fluid flow analyses (Thielicke and Stamhuis, 2014). The most sensitive part of this analysis is the cross-correlation algorithm, that can be solved for using three different options available within PIVlab. Here, the fast Fourier transform (FFT) window deformation algorithm is selected because in many situations it delivers the most accurate results. Small sub-images called interrogation areas are cross-correlated to derive the most probable particle displacement in the interrogation areas. This cross-correlation is a statistical pattern matching technique that aims to find the particle pattern from interrogation area I back in interrogation area I'. This statistical technique is implemented with the discrete cross- correlation function (Huang et al., 1997)

$$C(m,n) = \sum_{i=-\infty}^{\infty} \sum_{j=-\infty}^{\infty} [I(i,j)][I'(i+m, j+n)], \tag{3.7}$$

where i and j give the positions of the interrogation windows where sub-sampling occurs. The function Equation 3.7 is evaluated by the summation of the products of the pixel grey values in the two interrogation windows. A peak cross-correlation value results when the interrogation windows of the first and second frames match-up. The numerical value of the spatial shift variables that results in the best match-up (i.e., the highest correlation values) is a direct estimate of the average displacement vector for the group of particles that were captured in the interrogation windows. The process is repeated for all interrogation areas of the

image pair resulting in a complete vector diagram of the flow studied.

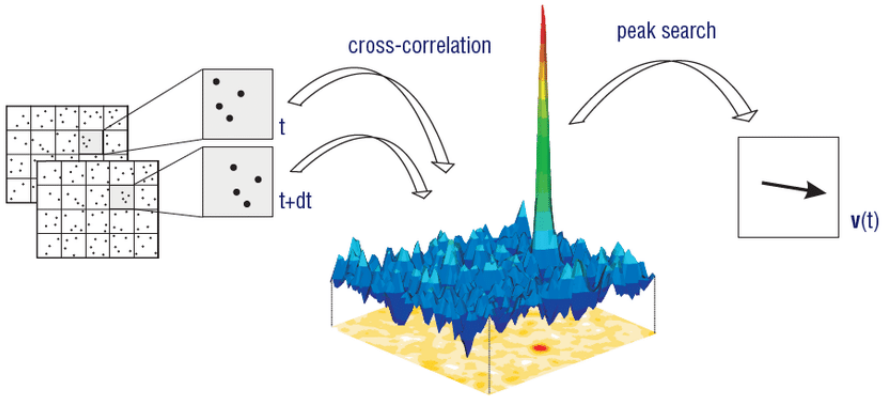

Figure 3.8: Schematic illustration of a common PIV process (Wieneke, 2017). Motions between image pairs are cross-correlated via a peak match-up, providing an average displacement of a group of particles or features within an interrogation area.

The particle displacement between two interrogation areas can be determined straightforward from the location of the intensity peak of the correlation matrix, and can be refined with every pass (Scarano and Riethmuller, 1999).

The amount of passes, size of each interrogation window, and their overlap are not arbitrarily selected by default. In fact, PIVlab offers a variety of interrogation options to balance between signal-to-noise ratio (SNR), robustness of the cross-correlation technique and computational demand. The first pass uses relatively large interrogation areas to reliably compute the displacement of the image data. The larger the interrogation areas, the better the SNR, and the more robust cross correlation is. But large interrogation areas will only give a very low vector resolution, and decreasing the sizes of the interrogation areas of each subsequent pass is needed to improve the resolution. The displacement information of the first pass is used to offset the interrogation areas in the second pass, and so on. An overlap between the interrogation areas is applied so that there is additional displacement information at the borders and corners of each interrogation area. Smaller overlap limits the amount of velocity vectors over each area, whereas large overlapping areas demand greater computational expenses. However, the amount of overlap does not improve the spatial resolution since neighbouring vectors are not independent. A commonly used overlap of 50% is therefore selected to account for these considerations (Roth and Katz, 2001).

3.3 ADCP measurements

3.3.1 Data collection

Flow velocities in the two areas were also derived from ADCP sensors (Teledyne RDI Workhorse Sentinel) mounted on a vessel along specific transects. The ADCP sensors measured velocities over vertical profiles using a broadband signal with a frequency of 614 kHz and a depth cell size of 0.5 m. The beam angle of the instrument was 20° with respect to the vertical, and the standard deviation per transmitted pulse was equal to 7.0 cms^{-1} (Teledyne, 2021). The measurements provide high quality data used for detailed flow information, and are therefore complementary in the analysis on the large-scale flow field. The ADCP data

are also intended for the validation of the RSIV-derived velocities. Ideally, the measurements should overlap with the time of drone filming (i.e. to measure within the same time interval) to validate the surface velocity vectors in the same stage of the tidal cycle. However, the different measurements were conducted closely one after another to avoid noise in the images generated by the vessel and its trail. Because flow velocities range from zero to about 4 ms^{-1} between slack water and maximum flood (see Section 2.3), the choice of collecting non-overlapping data restricts the duration of the sailed transects in each area. The transects should nevertheless cover the major part of the areas chosen to overlap with most of the RSIV-derived velocities. Therefore, the two domains were chosen to be sailed in 12 min considering a sailing velocity of 4 ms^{-1} . This time window was assumed sufficiently small for the flow to be stationary. A safety line orientated in north-south direction complicated the collection of ADCP data over the entire second area, causing some transects to be (partially) interrupted. Details on the proposed transects and their coordinates can be found in Appendix A. The actual sailed transects are shown in Figure 3.9. The sailing routes were be repeated several times per area (similar to the drone measurements), to include different stages within a tidal cycle.

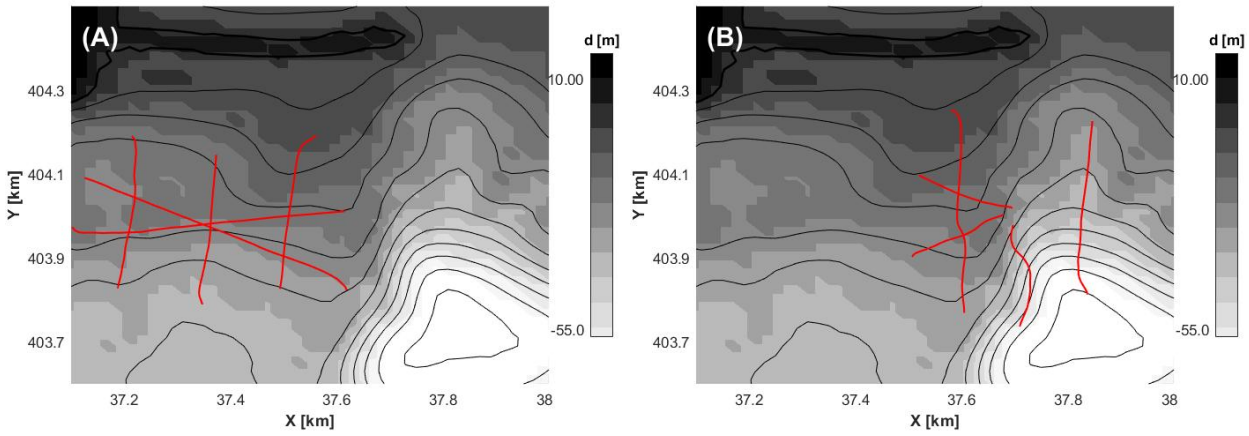

Figure 3.9: Sailed transects over the domain. The greyscale denotes the water depth. Note the north-south orientated barrier and the easterly stretched dam perpendicular to it. In the right figure, the transects are interrupted by a safety line.

3.3.2 Post-processing

The coordinates of the sailed transects were first stored in an interpolated x, y, t-space with a time step Δt equal to the duration of the transects. Depth-average velocities were computed by integrating the ADCP-derived velocities over the vertical data points, and dividing the result of that operation by the depth covered by the vertical data points. These depth-averaged velocities were then interpolated to the nodal points of the spatiotemporal grid using linear interpolation. ADCP data could not be collected at locations where the flow was too turbulent. For the RSIV validation, only values close to the water surface were taken into account. Depth-averaging was therefore performed over the upper five values (to a depth of 2.5 m from the water surface) to avoid the effect of large variations by instantaneous velocities.

4 Analysis and interpretation of observed flow data

This chapter describes the analysis and interpretation of data obtained from the field campaign. Section 4.1 first covers the results from the laboratory experiments because the camera calibration process is an essential step in the RSIV-process. With the intrinsic parameters and the expected magnitude of the projection errors known, the chapter continues with a translation to the field application. Section 4.2 elaborates on the projection quality estimate based on different GCP configurations at the Roompot inlet. It then proceeds with a sensitivity analysis and validation of RSIV-derived surface velocities. In Section 4.3, the validated results are used to interpret observations of large-scale flow patterns. The section continues with a time series analysis of the ADCP measurements throughout the domain to study temporal variations in the flow field. Finally, Section 4.4 concludes with a summary of the most important results derived in this chapter.

4.1 Validation of experimental cases

This section elaborates on the camera projection quality derived from the experimental cases in order to test a series of different marker configurations. These set-ups were similar to those at the Roompot inlet, and aided in assessing the errors expected to be found using a limited GCP distribution across the area. The transformation between image and world coordinates expressed by Equation 3.4 includes the estimation of both the intrinsic (K-matrix) and extrinsic (rotation matrix and translation vector) camera parameters.

4.1.1 Intrinsic camera parameters

As a first step in the image calibration procedure, the K-matrix was determined by Matlab's `Camera Calibrator` application. This calibration involved a total of 30 input images that contained a checkerboard pattern covering at least 20% of the imaged area. From these 30 images, 13 were rejected as they could not be detected by the calibration algorithm. The mean reprojection error, used to quantify how closely an estimate of a 3D point recreates the point's true projection, amounted 2.37 px for a $1.77{\cdot}10^7$ pixel image. After removing another 7 images that were considered outliers for having reprojection errors > 2 px, the mean reprojection error was reduced to 1.52 px. The estimated camera pose and the corresponding errors per image are shown in Figure 4.1. The intrinsic camera parameters were computed accordingly and are given in Table 2.

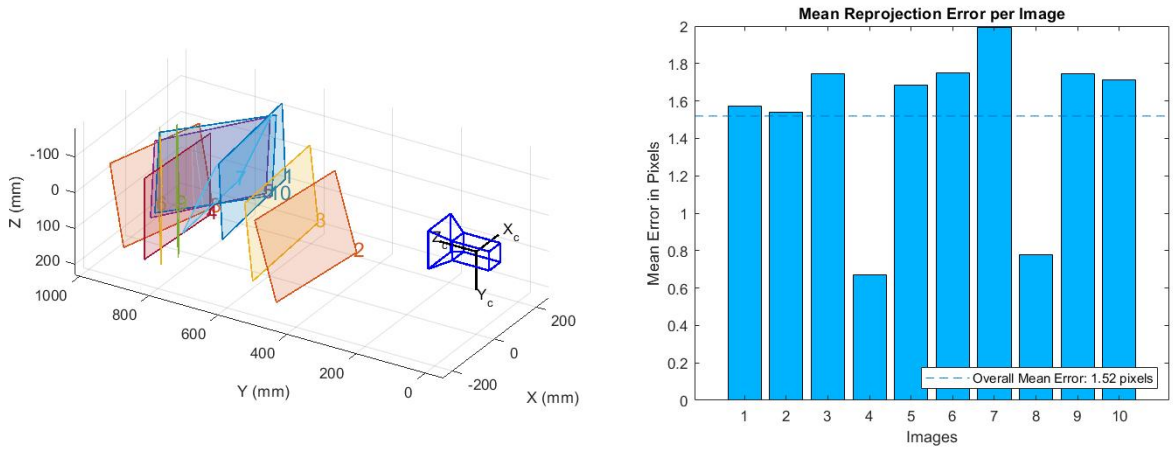

Figure 4.1: Estimated camera pose (left) and reprojection errors (right) used to determine the elements of the intrinsic camera matrix K.

Table 2: Intrinsic camera parameters and distortion coefficients determined by the `Camera Calibrator` within Matlab's Computer Vision Toolbox.

Parameter	**Value**
f_u	2687.62
f_v	2686.15
u_0	1974.34
v_0	1496.10
k_1	-0.13097076
k_2	0.10007409

4.1.2 Extrinsic camera parameters

The camera pose for the experimental base case set-up described in Section 3.3.4 was then solved for with PnP using the image coordinates (x', y') of the markers, their world coordinates (X, Y, Z), and the intrinsic camera parameters. The estimated camera position (X_c,Y_c,Z_c) was at 102.5 cm, -127.03 cm and 109.53 cm relative to the imaged plane, respectively, all of which were within 1.5 cm of the measured camera location (Figure 4.2).

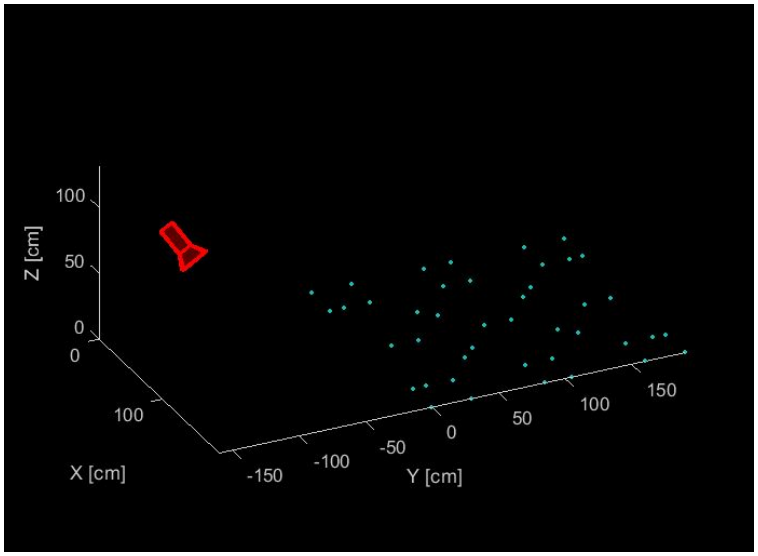

Figure 4.2: Estimated camera pose of the base case scenario derived from the *PnP* solution.

With the intrinsic parameters and camera pose known, the projection was computed from the rotation matrix and translation vector that make up the camera extrinsics. World coordinates were converted to their 2D image point locations and reprojected back to the physical space in order to estimate the projection quality. Figure 4.4 shows the results and projection for the base case set-up. The root-mean-square (RMS) error between all measured and projected coordinates was 1.32 cm.

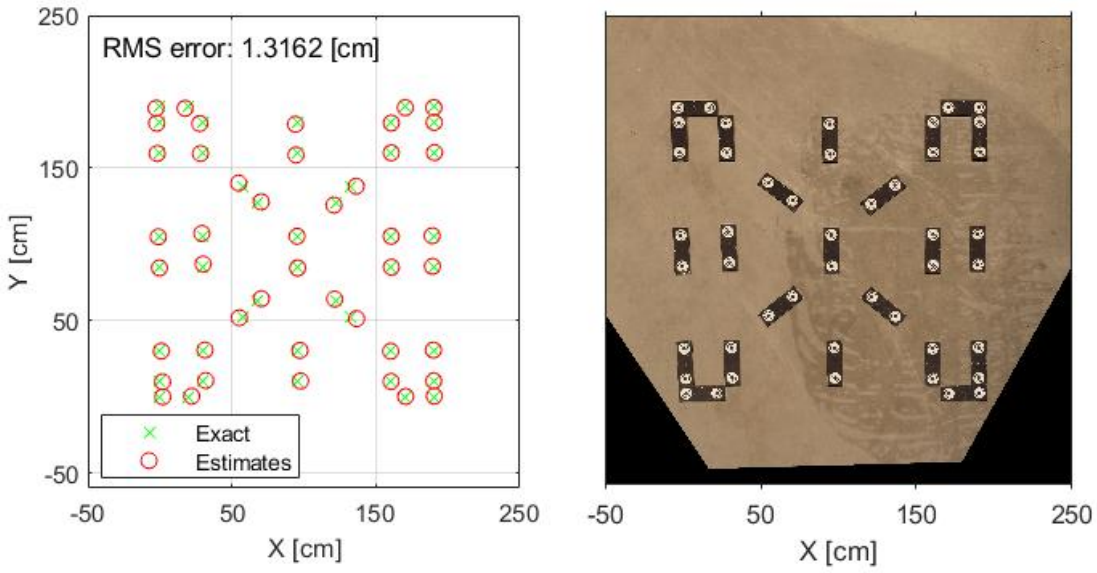

Figure 4.3: Left figure: RMS error between measured and estimated world coordinates of 46 markers across the base case set-up. Right figure: projected image providing a top view of the domain.

The RMS error is believed to originate from three uncertainty sources: (i) the reprojection error of 1.5 px introduced by calibrating the camera, (ii) the large angle at which the domain was imaged, and (iii) slight measurement errors of marker locations during the experimental set-up. With the base case as an 'exact' reference solution, different marker configurations were deployed similar to the field applications. The following set-ups were accounted for:

1. Markers placed across a straight horizontal line at y=190 cm that resembles the barrier's axis in the Roompot area.
2. Similar to 1), with the exception of having slight $y-$variability of 5 cm that accounts for lateral distribution on the barrier's bike way.
3. Markers placed across straight lines on the upper and right margins of the domain (at x=190cm and y=190 cm). The vertically placed markers represent the dam parallel to the main flow.
4. Similar to 3), but now with slight $y-$variability of 5 cm on the $x-$axis.

For case 1, the complete lack of spatial information in the $y-$direction limited the accuracy of the projection (Figure 4.4). The RMS error equalled 12.4 cm which is the highest value of all test configurations. When small variations in the $y-$direction are added (case 2), the RMS error reduced to an estimated 9.8

cm. For the third test scenario, the error equalled 7.3 cm. The effect of adding markers along the $y-$ axis thus dominates over the lack of lateral variability on the $x-$axis. Combining the spatially varied markers (case 4) introduced the lowest RMS error with a value of 6.7 cm. It should be noted that due to an uneven marker distribution throughout the domain and measurement errors that were made, the solution of the camera projection is biased. This is evident from the accurate estimates at the right margin of the domain with respect to the other estimates (lower panels in Figure 4.4). The trends however indicate that adding lateral variability greatly contribute to the projection quality, and in a more relative sense helped to predict expected projection errors in the Roompot area.

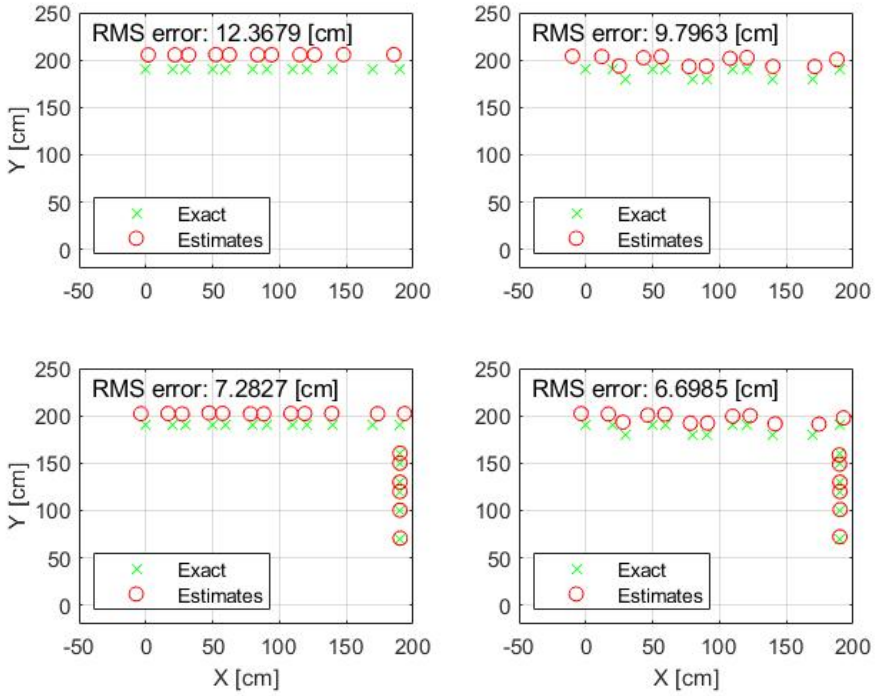

Figure 4.4: Different marker configurations and their RMS error between measured and estimated positions. Upper panels: markers were only placed along the $x-$axis similar to the barrier's axis in the Roompot area. Lower panels: added markers on the right margin of the domain that resemble the dam parallel to the main flow. Errors significantly reduce when lateral variability is added.

4.2 RSIV analysis

4.2.1 Projection analysis at the Roompot inlet

In Section 3.3.4 emphasis was put on the importance of determining the pixel dimensions in order to convert velocities from px/frame rate to ms^{-1}. In a controlled environment, the distance between the camera and each reference point is known to great accuracy. At the Roompot inlet this information is absent, and the homography was computed instead. Validating the projection is nonetheless still possible in a more relative manner, i.e. by comparing the errors for different marker set-ups. In Area B the lack of GCPs ultimately led to very inaccurate projections, and it was chosen not to proceed with the RSIV procedure at the flow near the scour hole. In Appendix E.2 more information on this projection and attempts to compensate for

the limited amount of GCPs is shared.

For Area A the image transformations provided much better results, of which the projection qualities were tested using three marker configurations:

- Case I: 11 GCPs that were placed only in the $x-$direction on top of the barrier.
- Case II: 18 GCPs including slight variability in perpendicular direction on the barrier's bikeway.
- Case III: similar to case 3, but with an additional marker just within the camera's view positioned on the dam at a perpendicular distance of about 100 m from the barrier.

Figure 4.5 shows the projected homography estimated for the three cases cases. The projection of case I appears to be very distorted. Differences between the other two projections are much smaller.

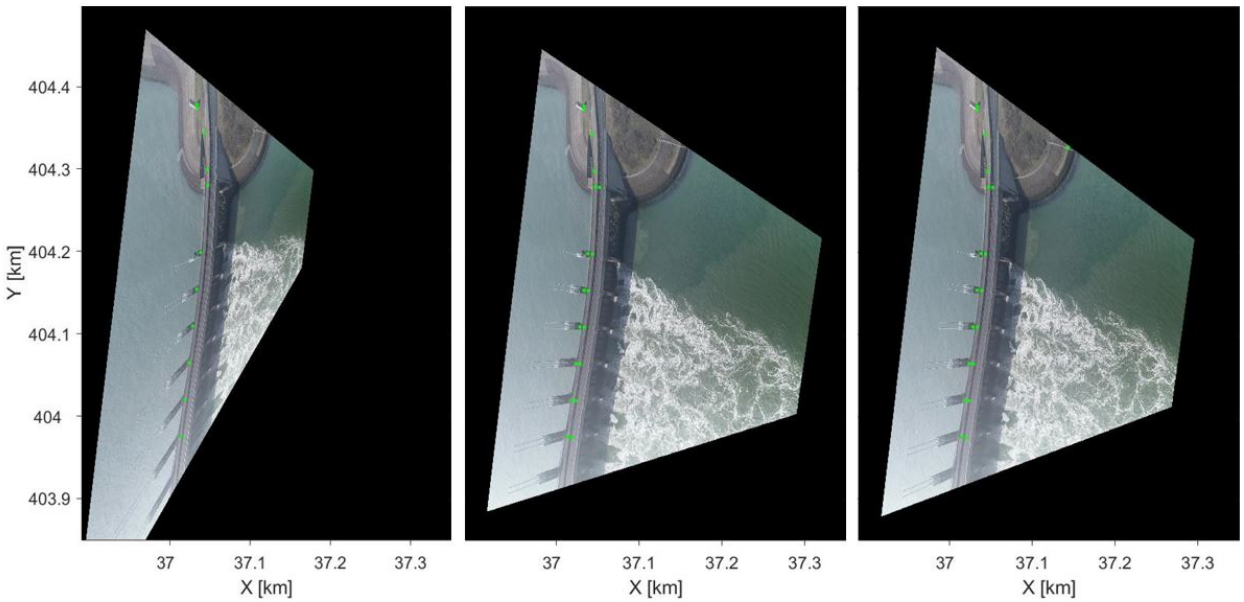

Figure 4.5: Camera projection in the ETRS89 (RD) reference system, for a) case I, b) case II and c) case III.

The variations in x, y-extent between the three configurations were then compared using several true distances known from the measured GPS locations. These distances were chosen such that they would cover areas sensitive to the camera projection, particularly in lateral direction and around the margins. Figure 4.6 shows an image after correcting for lens distortion with the distances 1...6 that were compared with the different projections. In Table 3 the distances measured by GPS are provided. The subtracted distances for the locations are given by Δd in Table 4.

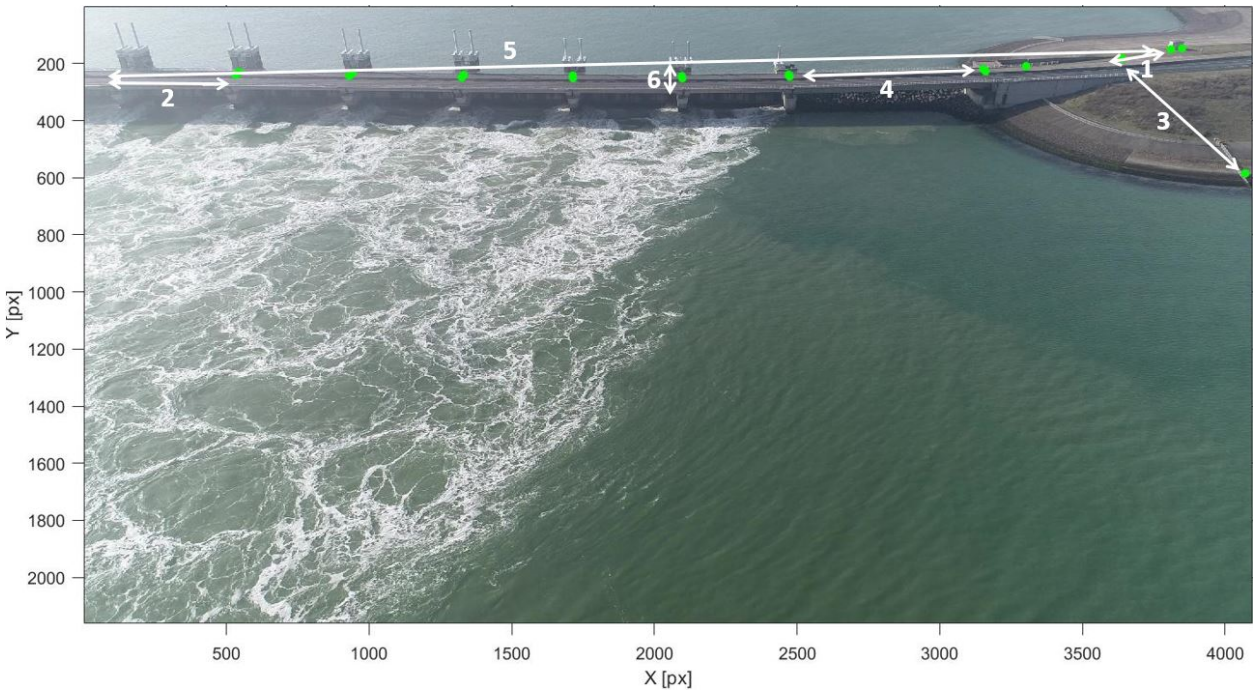

Figure 4.6: Undistorted image after lens correction. White arrows indicate distances between several measured positions across the domain. Green dots mark the locations of the GCPs.

Table 3: True distances between several locations measured by GPS coordinates.

Location	True distance [m]
1	33.7
2	45.1
3	100.9
4	81.5
5	446.8
6	11.7

A closer look on the values of Δd quickly reveals remarkable projection differences that arise from the varying GCP configurations. For all cases, variations of distances in $y-$direction (locations 1,2,4, and 5) are very small due to the well distributed markers across the barrier's axis. Even the largest distance of 6.1 m corresponding to case I that spans over the entire barrier only leads to an average vertical error of about 1.5 mm/px ($\sim$ 1% of vertical pixel dimension). In general, maximum errors between measured distances along the $y-$direction in all cases account for averages < 5 mm/px ($\sim$ 5% of vertical pixel dimension). Although for case I deviations on average are slightly larger, differences in vertical scaling for each configurations is very similar.

On the contrary, horizontal deviations are much greater (locations 3 and 6), and the added GCPs in lateral direction have a severe impact on the scaling in perpendicular direction to the barrier. Particularly for case I, errors over a 100 m stretch can be as large as 25% of the horizontal pixel dimension. For case III, Δd equals 10 cm over the width of the road and 2.8 m for location 3. Although the lateral errors are within

an acceptable range of < 5 % of the true distances, information on scaling at large $x-$ values (close to the camera) is missing. To what extent this lack of information affects the RSIV results is covered in the next section.

Table 4: Overview of the projection quality for the three different cases. Δd is the absolute difference between measured and projected distances.

Location	**Case I**		**Case II**		**Case III**	
	Δd [m]	Deviation (%)	Δd [m]	Deviation (%)	Δd [m]	Deviation (%)
1	1.9	5.6	2.8	8.3	1.8	5.3
2	2.3	5.1	0.2	0.4	1.2	2.7
3	25.9	25.7	9.5	9.4	2.8	2.8
4	1.4	1.7	1.6	2.0	1.6	2.0
5	6.1	1.4	1.0	0.2	3.0	0.7
6	1.6	13.7	0.7	6.0	0.1	0.9

4.2.2 Sensitivity analysis

Now that each image is scaled identically and the pixel dimensions validated for the three marker configurations, the next step is to apply Equation 3.7 over a series of calibrated image pairs. Before the analysis on flow characteristics can be performed, it is meaningful to first discuss the contrasts in the computed velocities that arise from various settings implemented in PIVlab. This allows for flow characteristics to be studied in a more representative manner. In Section 3.3.5 the choice for the most essential settings was elaborated on. What is left are the options with respect to the interrogation sizes, time windows (i.e. amount of image pairs), and the frame rate over which the velocity vectors are to be computed. As was previously discussed the size of the interrogation areas should partially overlap to account for additional information on the displacement at the borders and corners of each image. Also, to prevent the process to be dominated by noise and to compute a more robust cross-correlation, large-sized interrogation areas for the first pass are selected. In the two subsequent passes, the amount of pixels is reduced by 50%. In order to obtain the optimal parameters for RSIV analysis, different sensitivity tests were first carried out. Effects of different parameters are discussed below:

- Length of images sequences. Three video durations (10, 30, and 60 s) were tested aiming to determine an appropriate length of image sequences. The results are shown in Figure 4.7. The effect of geometric distortion is immediately recognized by the velocity values computed over the barrier and outside the domain that are non-physical in nature, and are much more pronounced using larger recordings. On the barrier, these values are in the order of 0.25 - 0.5 ms^{-1} for T=10 sec and T= 30 sec, while errors up to 2 ms^{-1} are observed for $T = 60$ sec. For the latter, large rotations are evident between the upper and lower part of the barrier, but are also pronounced on the water surface. The errors here are reflected in the velocities within the main current, which are generally about 1 ms^{-1} larger with respect to the other durations. In Table 5 the RMS errors between image pairs for the three durations are shown, with comparible errors between records of 10 s and 30 s and much larger RMS errors for a duration of 60 s. The remaining part of the RSIV analysis therefore continuous on the flow characteristics derived from the configuration that includes a duration of 30 s, because it provides the most appropriate trade-off

between geometric errors and record length. The magnitude of the erroneous velocities outside the domain (about 0.25 ms^{-1}) that are added to the velocities derived over the water surface are accounted for during further analyses.

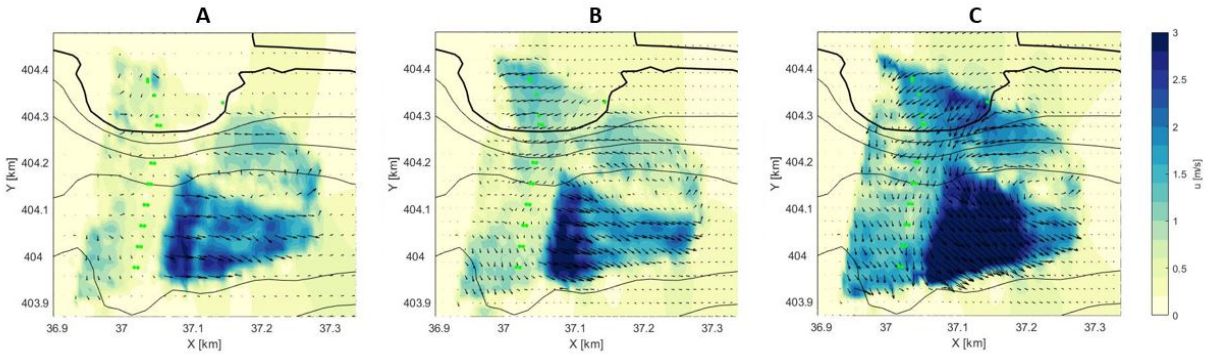

Figure 4.7: Derived velocity vectors for three record durations: (a) 10 s, (b) 30 s, and (c) 60 s. Green dots indicate the estimated locations of the GCPs.

Table 5: Maximum RMS errors between image pairs for different durations.

***T* [s]**	**Max. RMS error [m]**
10	5.11
30	6.70
60	12.81

- Numbers of passes of different IA kernels in PIVlab. In PIVlab, the pass of a larger kernel helps to calculate global velocities, and the smaller one is used for local results with more accuracy. The difference in estimated flow fields between three and two passes appeared to be negligible. Using two passes was considered more efficient to present the flow patterns and was thus utilized in the further calculations.

- Sizes of IA: The key element of RSIV image processing is to search the most probable tracer path by comparing IA's between two consecutive frames. Images with an IA of 64, 128, and 192, and 256 pixels were analyzed, of which the results are illustrated in Figure 4.8. Loss of coherence is observed for an IA of 64 px, whereas information on small-scale structures is lost for an IA of 256. To prevent the process to be dominated by noise and to compute a more robust cross-correlation, large-sized interrogation areas are generally preferred. Thielicke and Stamhuis (2014) mention that maximum particle displacement should therefore be smaller than one quarter of the interrogation area. With a maximum velocity threshold of 5 m/s, particle displacement will not exceed $5/0.11 = 45$ px. An IA of 192 would then be the most appropriate window size and is used throughout this study.

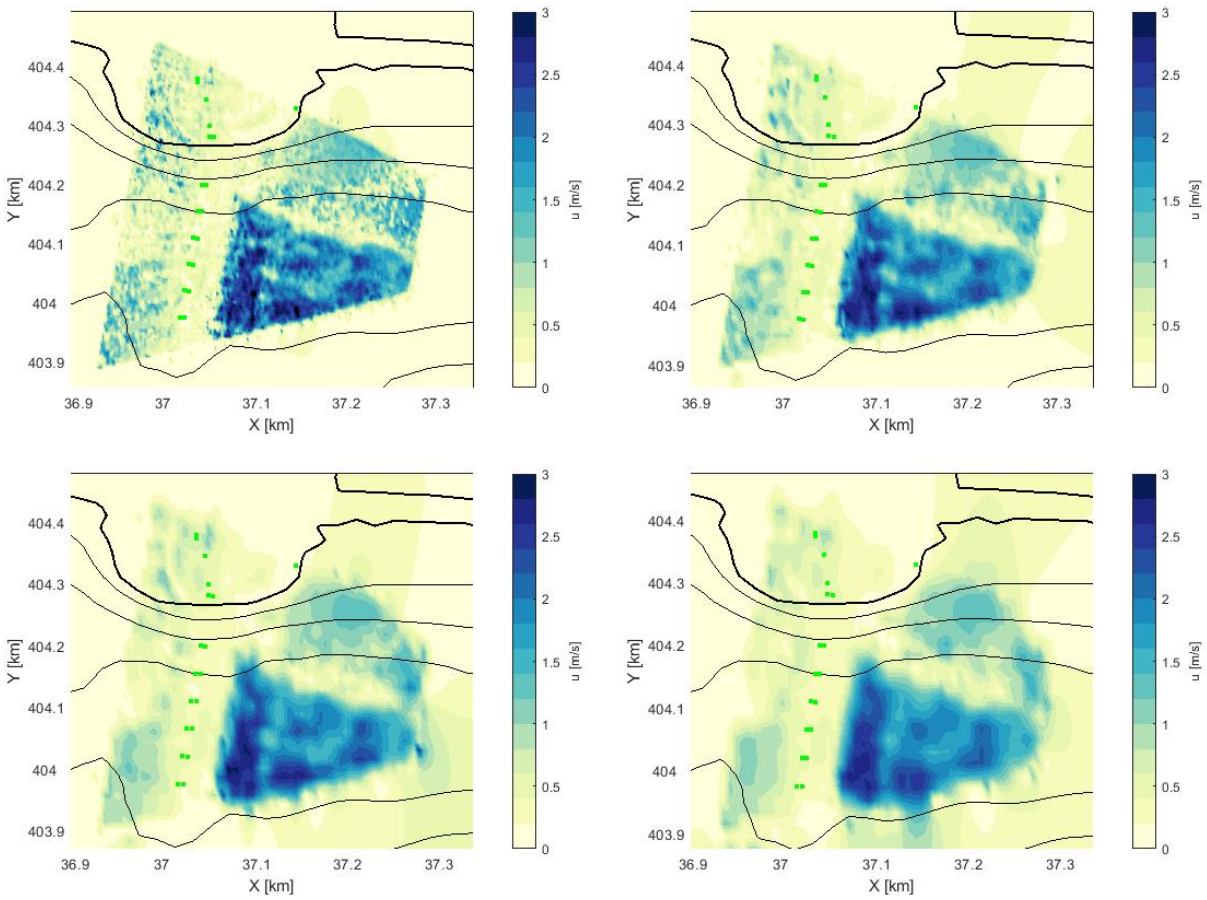

	a	b	c	d
IA [px]	64	128	192	256
Size (x,y) $[m^2]$	19x11	38x22	58x33	76x44

Figure 4.8: Four different interrogation areas that were used in the sensitivity analysis with increasing size from (a) (upper left) to (d) (lower right). Green dots indicate the projected GCP locations.

- Amount of frames per second. Although the camera filmed at 30 fps, particle motion between each image pair may be detected differently when choosing a larger time step. The choice for a suitable frame rate depends on how well a group of particles can be correlated: it should not be too small for motions to be undetected, and not too large to prevent particle agglomeration to saturate the interrogation areas. To analyze this, velocity vectors were computed using frame rates of 3, 10, and 30 fps (Figure 4.9. Large differences across the domain are clearly evident. Based on the expected velocity distribution, image (b) appears to yield the most appropriate flow field. In a quick assessment to validate whether or not this is correct, and to attempt to explain the velocity differences for each frame rate, tracers within an interrogation area were tracked visually for a series of successive images. In Figure 4.10 the water surface is overlain with a 192x192 px rectangular grid that corresponds to the selected *IA* size. Motion between each image was poorly distinguishable for a frame rate of 30 fps,

whereas large displacements were apparent when choosing 3 fps. A value of 10 fps is therefore selected based on these considerations. Although dependent on seeding density and flow velocities, similar rates were used in other related studies regarding riverine environments, where frequencies of 5 fps (Le Coz et al., 2010), 7 fps Weitbrecht et al. (2008), and 12 fps (Zhu and Lipeme Kouyi, 2019; Dal Sasso et al., 2021; Detert and Weitbrecht, 2015) were applied.

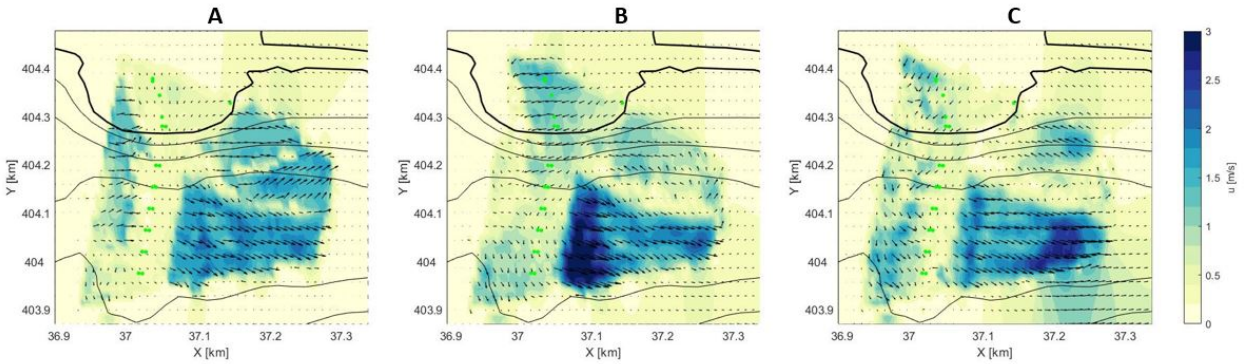

Figure 4.9: Derived velocity vectors for various frame rates per second tested: (a) 3 fps, (b) 10 fps, and (c) 30 fps. Green dots indicate the projected GCP locations.

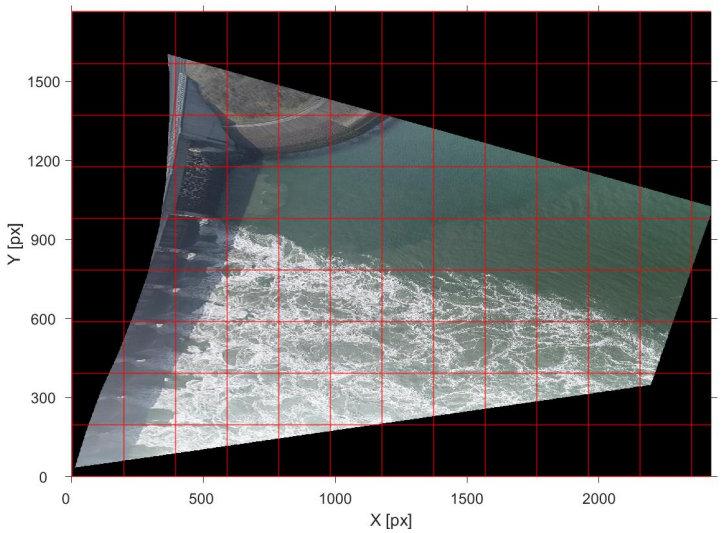

Figure 4.10: Projected image of the water surface overlain by a rectangular grid in which each rectangle has the dimensions of the first interrogation area (192x192 px). The image is used to visually observe displacement of boils between image pairs for the three different frame rates.

- Pretreatment methods in PIVlab. Finally, different PIVlab pretreatment methods were applied in the analyses and the results show a great similarity with or without different highpass, intensity capping, or window deformation treatments. Only a Wiener filter was found to remove noise on the flow field related to the surface ripples. For the current application these velocities not related to the main current were clearly distinguished, and therefore do not contribute to improved velocity estimates in the relevant part of the area. Therefore, no pretreatment method was applied. A selection of these

methods is further discussed in Appendix E.1.

In Table 6 the results are summarized.

Table 6: Selected options to be used for further analysis based on the results from this section.

Parameter	Setting
Duration	30 [s]
FPS	10 [Hz]
IA (1st pass)	192 [px]
Overlap	50%
Nr. of passes	2
Sub-pixel precision	3-point fit Gaussian
Window deformation	Linear
High/lowpass filter	-

4.2.3 RSIV validation

Image and vector-based validation

In this section a closer look on the auto-correlation results is taken by controlling a series of post-processing techniques to verify (in)accurate velocities present across the computed flow field. To exclude geometric errors and computed velocities not related to the flow (such as motion of traffic along the barrier's road), a mask is applied to only cover the water surface at the estuary side of the barrier. A threshold rejecting vectors with a standard deviation of 3 times the velocity value and a normalized median test (Westerweel and Scarano, 2005) were included to filter out inaccuracies. The normalised median test adapts to the local flow situations and is based on the velocity fluctuations and median of a 3×3 neighbourhood of data points. Also, velocity limits were set based on the results from Chapter 2.4. Streamwise velocities are permitted on the interval [-2,5], whereas lateral velocities are accepted on the interval [-2,2]. Figure 4.11(a) illustrates the entire range of velocities computed over the imaged water surface with many erroneous, non-physical velocities present before filtering. The accepted velocities after applying the thresholds and limits are shown in Figure 4.11(b). The choice for the velocity limits specified is supported by the high point density found within the rectangular area.

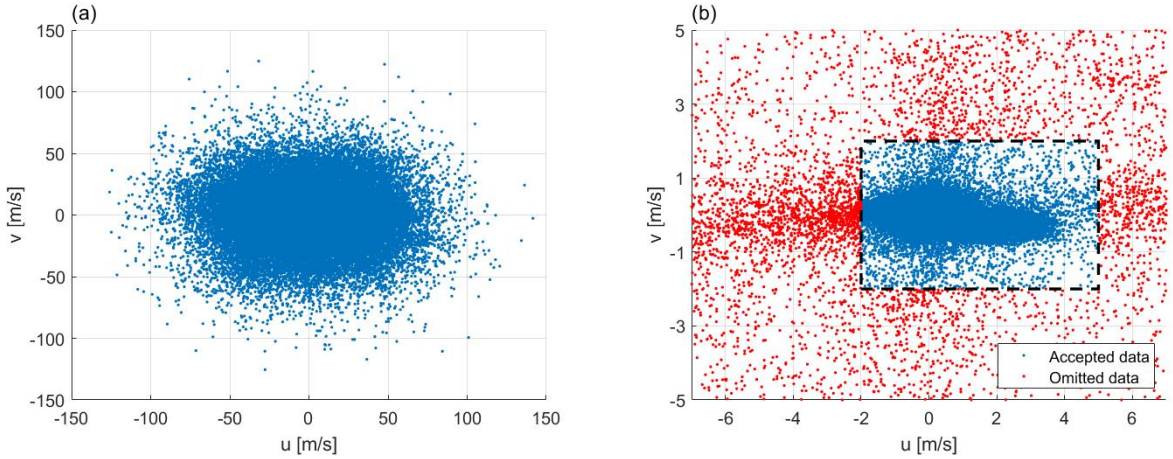

Figure 4.11: Scatter plots of (a) all computed values in the domain before filtering and (b) close-up of accepted velocities.

The velocities that were eventually accepted amounted for 33% of the total number of derived velocities. An interpolation technique based on the work of D'Errico (2006) was applied to linearly interpolate between rejected values over the water surface. In Figure 4.12(a) the flow field is plotted using the filtered and interpolated velocities.

For a more general application of filtering techniques in environmental flows, the extent to which the computed flow field is sensitive to the velocity limits is further examined by selecting a series of different velocity intervals (Figure 4.12). It appears that the flow field remains unaffected by the selected limits. Apparently, the high and erroneous velocity values that were included are very local and are averaged out by the abundance of correct flow velocities within the interrogation areas.

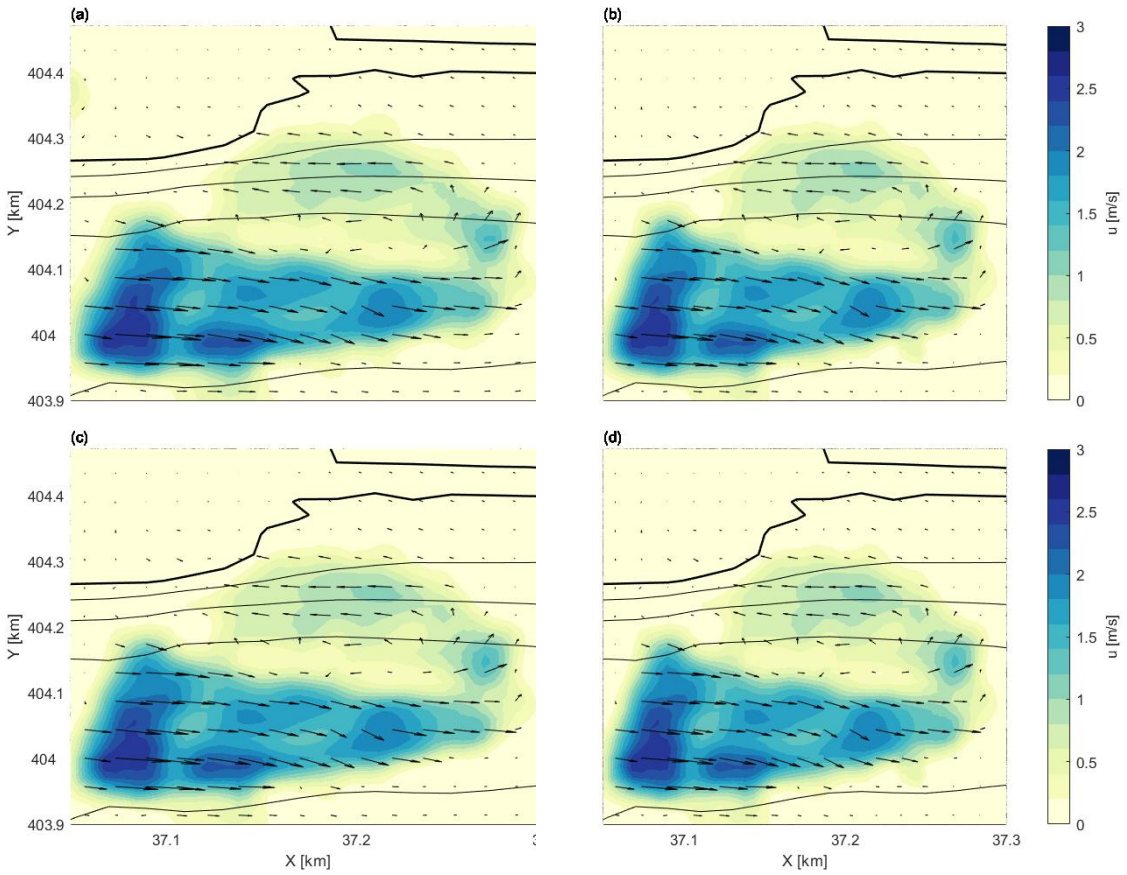

	(a)	(b)	(c)	(d)
u [m/s]	[-2,5]	[-5,10]	[-2,5]	[-100,100]
v [m/s]	[-2,2]	[-2,2]	[-5,5]	[-100,100]

Figure 4.12: Computed flow fields according to a series of different velocity limits in streamwise and lateral direction.

Images can also be validated by assessing the direction and magnitude of computed vectors over the water surface. In Figure 4.13 a selection of vectors is plotted over the greyscale projection. Largest values are found close to the barrier in the main flow, gradually decreasing in streamwise direction. Vectors computed north of the main current are oriented differently. Natural tracers are absent here and instead surface motion is induced by ripples. These ripples are generated by the main current (at the right margin of the image) and an eastern wind. At the location where the Northsea waters enter the estuary through the separate openings, velocity values are either missing or very small. Although highest velocities are expected here, the area suffers from insufficient lightning. Sunlight is partially blocked by the barrier and boils on the water surface are poorly distinguishable from their surroundings. Shadow effects therefore cause velocities here to be severely underestimated.

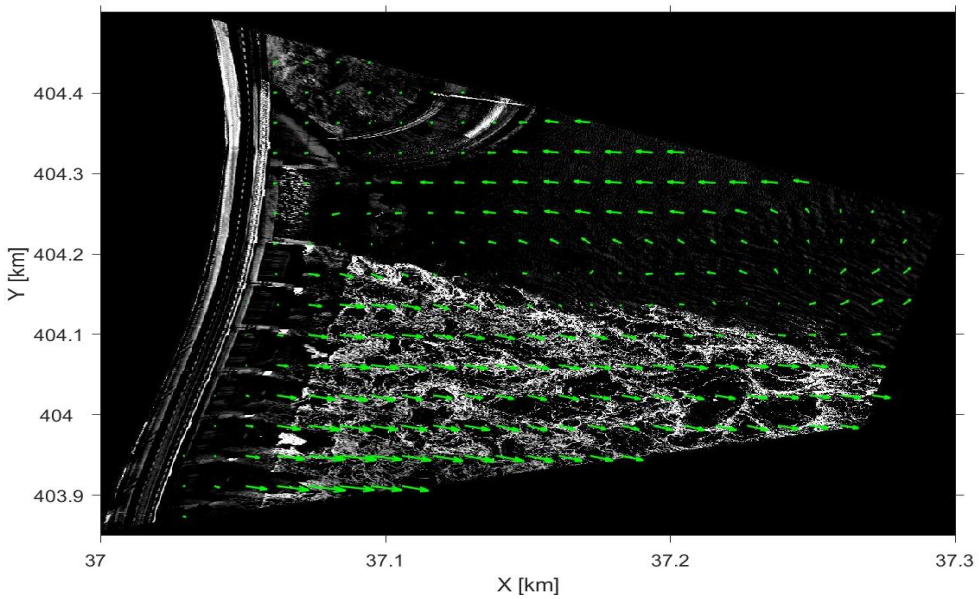

Figure 4.13: Time-averaged vector magnitudes computed over the water surface. Poor lightning and surface roughness limit the RSIV accuracy.

Validation by ADCP

The derived velocity field using the optimized RSIV settings is validated with ADCP data for the area in which the measurements overlap. Because the flow near the barrier was too turbulent for the ADCP data to be collected, velocities are compared for a distance reaching between 80 and 230 m in easterly direction from the barrier. The mean velocity value of the error that originates from geometric distortion was subtracted from the velocity field. ADCP measurements were carried out between 12.30 pm - 14.30 pm (2.5 to 0.5 hours before maximum flood), followed by 30 seconds of drone filming at 14.45 pm. Figure 4.14 shows the comparison between (a) the RSIV-derived velocities and (b) depth-averaged ADCP values over a depth of 2.5 m. Adjacent to the main flow, for $y>$ 200 m, velocities derived by RSIV are not reflected by the ADCP and have a different orientation than those within the main flow. The origin of this discrepancy was discussed in the previous section.

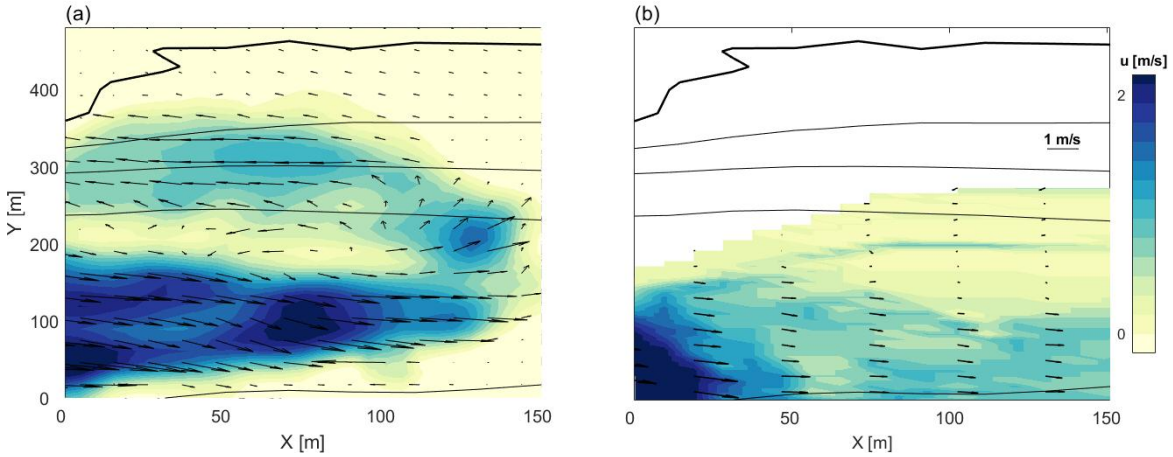

Figure 4.14: (a) velocities derived from RSIV. Note the strong return currents adjacent to the main flow. (b) depth-averaged velocities measured by ADCP measurements over a depth of 2.5 m.

The results for the main flow generally agree to $\mathcal{O}(10^{-1})$ ms^{-1} , with RSIV-derived velocities showing slightly higher values with respect to the ADCP data. A maximum velocity difference of about 1 ms^{-1} is found at $x = 75$ m. In Figure 4.15 the magnitude of the velocities across a horizontal transect of 135 m (a-b) and a vertical stretch of 75 m (c-d) are compared for three different stages in the tidal cycle: 3 hrs before maximum flood (T_1), 2 hrs before maximum flood (T_2), and 1 hr before maximum flood (T_3). The flow around maximum flood was too turbulent for the ADCP data to be measured. Some velocities at T_3 were linearly interpolated in order to retain continuous data. The higher RSIV velocities are clearly evident, with average differences generally between 0.2 - 0.6 ms^{-1} . Slightly higher values were measured towards maximum flood, thus indicating that differences with RSIV-derived velocities diminish over a tidal cycle. A large anomaly in the middle of the horizontal transect is present that was also observed from Figure 4.14. This may be the result of the smaller time-averaging by RSIV, poor tracer density, or both. Velocity disparities over the remaining part of the flow are mostly attributed to the different time intervals of measuring, the lack of ADCP data in highly turbulent parts of the flow, and the depth difference over which velocities were computed.

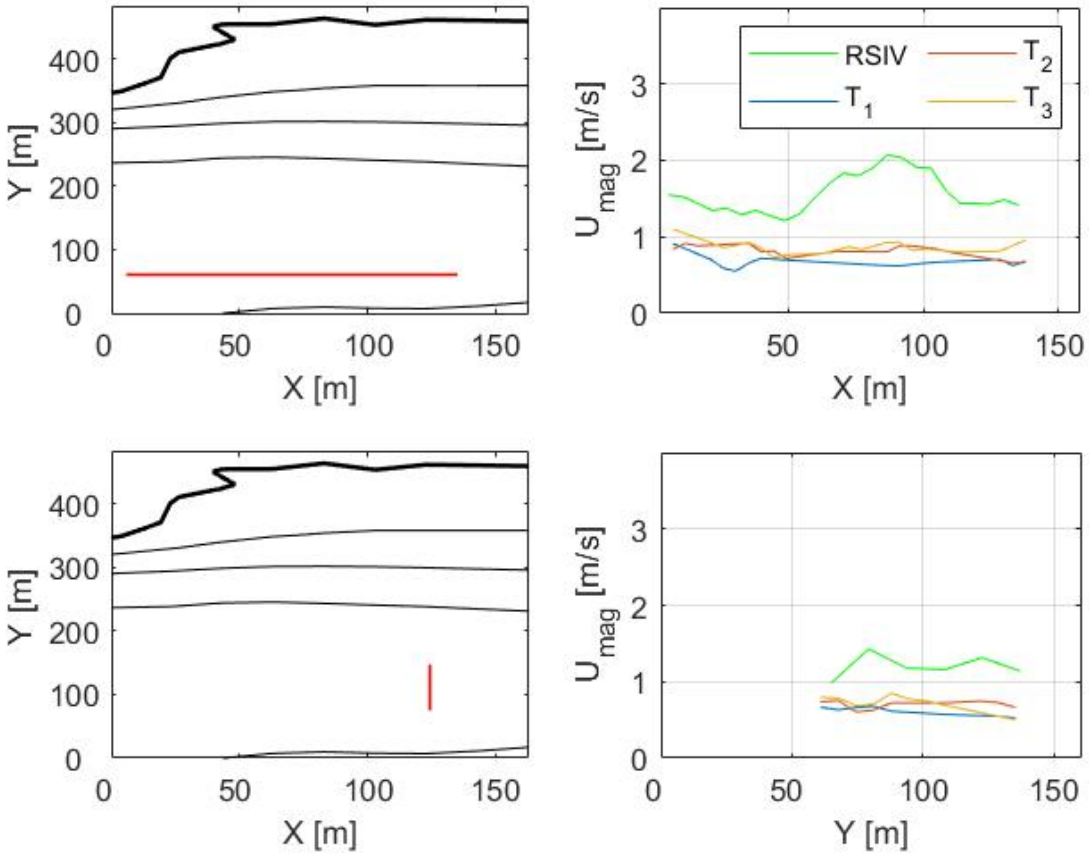

Figure 4.15: Comparison between velocities measured by RSIV and ADCP along two overlapping transects in an interpolated space. T_1 - T_3 indicate the different time intervals towards maximum flood.

4.3 Observations of large-scale flow patterns

With the aid of the ADCP data and validated RSIV results an attempt is made to quantify flow characteristics within the main current. Chapter 2 concluded with a discussion on enhanced mixing of mass and momentum as a result of the temporarily varying tidal flow through the ES-SSB. These processes have shown to affect the turbulence intensities around local scour holes. Developing large-scale horizontal flow structures over a tidal cycle contribute to additional hydraulic loading on the bed, and their macro properties may be estimated using a combination of the techniques applied so far.

4.3.1 RSIV velocity profiles

Figure 4.16 shows the 30 s time-averaged filtered velocity field derived from RSIV. The near-field region of the flow $x/H < 2$ matches the classical 2D structure of a jet close to the inlet, and is dominated by the high velocity core with velocities in the order of 2 - 3 ms^{-1}. The intermediate region, covering the remaining part of the imaged flow, stretches from about 50 m to 250 m east of the barrier. Velocities in this part of the flow range between 1 and 2 ms^{-1}. To obtain a better visualization of the flow non-uniformity, Figure 4.17 illustrates

lateral velocity gradients along transects R_1 and R_2 indicated in Figure 4.16. Using ordinary polynomial fitting, gradients of the order $\mathcal{O}(10^{-3})$ are estimated over both transects. Even though these values depend on the location of the transect over which they are computed, results were consistent throughout the analysis. These flow quantities in principle allow for the estimation of mixing layer characteristics that were introduced in Chapter 2. It should however be stressed that the global profiles and complexity of the flow reduce the estimation quality to rough approximations, rather than estimations of specific values that can be compared with results derived from experiments in controlled environments. With a maximum velocity difference of about 1.5 ms^{-1} and lateral velocity gradients of about $7\mathrm{e}^{-3}\mathrm{s}^{-1}$, the mixing layer width (Equation 2.2) equals an estimated 200 m. This value seems too large in the area close to the barrier (R_1) where the mixing layer has yet to develop, but may be more correct at larger streamwise distances. The single time interval over which images were acquired limits observations on temporal evolution of flow non-uniformity. The analysis therefore continues with the ADCP data measured over intervals T_1 - T_3.

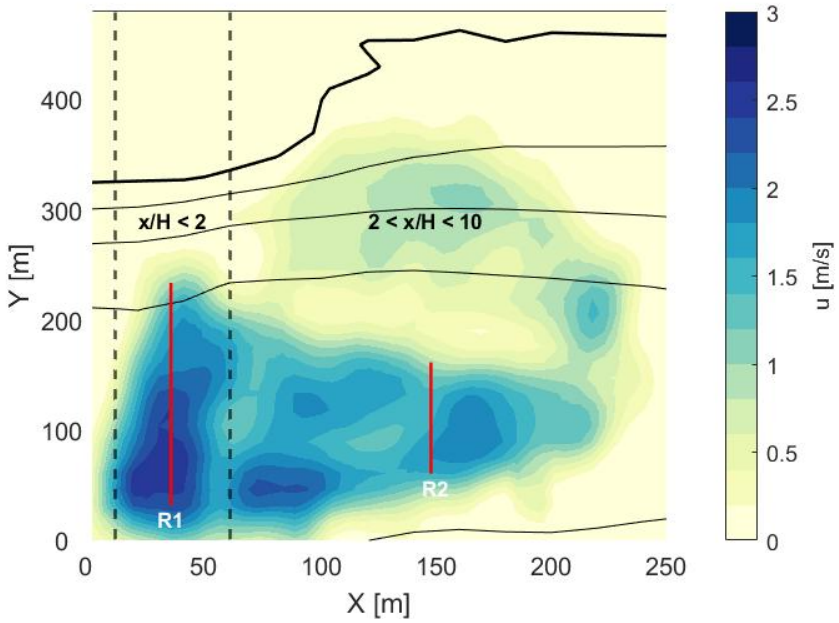

Figure 4.16: RSIV-derived flow field over the whole domain. R_1 and R_2 are the transects over which lateral velocity gradients are estimated. The dotted lines indicate the regions classified in a typical 2D jet.

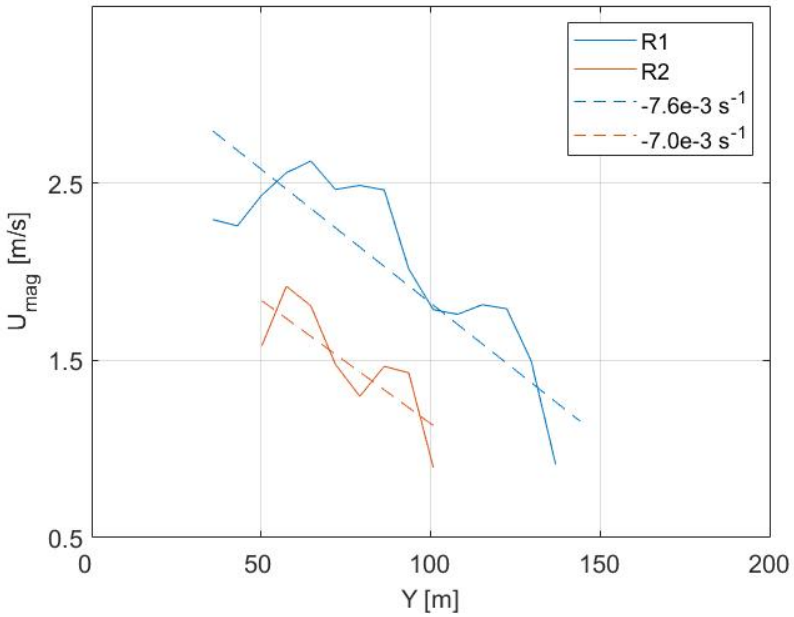

Figure 4.17: RSIV velocity profiles along lateral transect R_1 and R_2. Trend lines are plotted as dotted curves using a polynomial fit.

4.3.2 ADCP time series analysis

Developing flow non-uniformity

Differences in flow non-uniformity over a tidal cycle can be assessed via temporal variations in lateral velocity gradients over the domain. For Area A, these profiles are computed along transects $R3 - R5$ illustrated in Figure 4.18 with a spatial interval of about 150 m. Observed values of cross-sectionally averaged streamwise velocity u_a, lateral variation in streamwise velocity over the cross-section ΔU, and the maximum lateral velocity gradient du/dy are shown in Table 7. These quantities will be discussed separately:

- For each transect, the cross-sectionally averaged streamwise velocity u_a increases between T_1 and T_3, which is attributed to the increase in flow velocities between slack tide and maximum flood. Significant variations in u_a also exist in streamwise direction, with higher values found closer to the barrier.
- The lateral cross-sectional variation in streamwise velocity (ΔU) is defined as the difference between the minimum and maximum velocity along a transect. It generally shows larger values towards maximum flood, caused by the increasing velocities in the main flow. Similar to u_a and following the same reasoning, ΔU decreases in streamwise direction.
- The maximum lateral velocity gradient ($(\frac{du}{dy})_{max}$) is computed by dividing ΔU over the corresponding lateral distance, and therefore exhibits the same trends: maximum lateral gradients increase towards maximum flood, and decrease in streamwise direction.

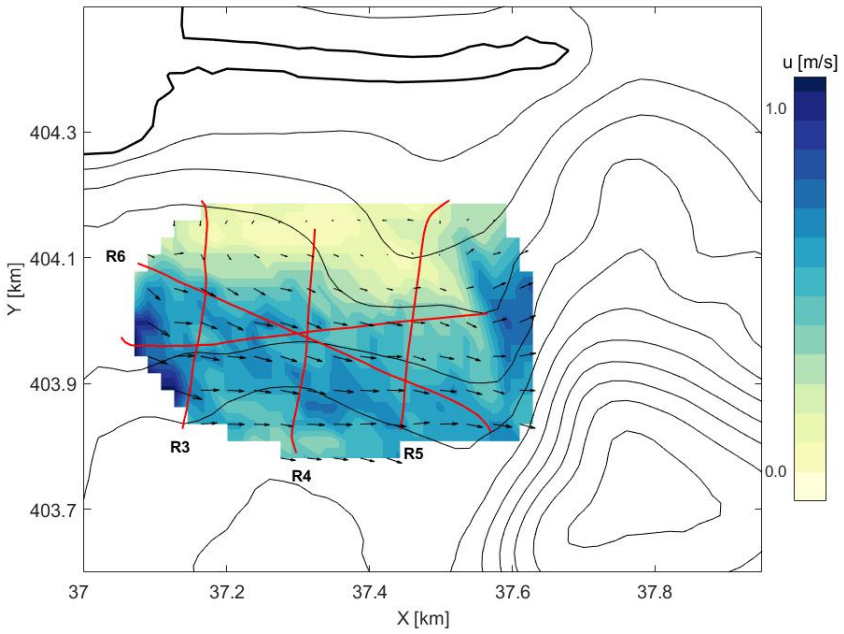

Figure 4.18: Processed depth-averaged velocities over a depth of 2.5 m, measured with ADCP. $R3$ - $R5$ are transects over which lateral velocity profiles are computed. R_6 indicates a streamwise transect used to estimate turbulence length scales in the main flow.

Mixing layer widths can again be estimated using the quantities in Table 7. Trends in the lateral velocity profiles are consistent and at least provide some degree of confidence in the order of magnitude of the mixing layer's extent. Lateral velocity gradients and lateral cross-sectional variations are of the order $\mathcal{O}(10^{-3})$ - $\mathcal{O}(10^{-2})$, and $\mathcal{O}(10^{1})$, respectively. This leads to a width of the mixing layer δ of $\mathcal{O}(10^{2})$. More specifically, between transects $R3$ - $R5$ the width increases from about 250 m to 332 m at interval T_1, from 217 to 303 m at T_2, and from 207 m to 324 m at T_3. This would imply that the size of the mixing layer is relatively stable at large distances from the barrier, where the velocity range over a tidal cycle is not as much affected as observed close to the inlet.

Table 7: Observed values of cross-sectionally averaged streamwise velocity u_a, lateral variation in streamwise velocity over the cross-section ΔU, and the maximum lateral velocity gradient du/dy, along transects $R3$ - $R5$.

	Transect	u_a [m/s]	ΔU [m/s]	$(\frac{du}{dy})_{max}$ [s^{-1}]
T_1: 3 hours before maximum flood	R_3	0.68	1.02	4.07e-3
	R_4	0.64	0.88	3.39e-3
	R_5	0.38	0.71	2.14e-3
T_2: 2 hours before maximum flood	R_3	0.78	1.48	6.83e-3
	R_4	0.72	1.20	3.66e-3
	R_5	0.57	1.03	3.40e-3
T_3: 1 hour before maximum flood	R_3	0.86	1.48	7.15e-3
	R_4	0.83	1.16	4.47e-3
	R_5	0.60	1.20	3.70e-3

Figure Figure 4.19 shows the streamlines and depth-averaged flow velocities over Area A for the three different time intervals T_1 - T_3. At T_1, flow velocities are relatively moderate with parallel streamlines in the core of the jet. A recirculation zone indicated by the white arrow is forming and streamlines adjacent to the main current are slightly contracted. At T_2 and T_3, the recirculation zone is more pronounced and propagates in streamwise direction. Streamlines in the main flow are still parallel over the different time intervals, but are increasingly contracting on the interface with the recirculation zones. The mutual relation between flow contraction and the development of a recirculation zone is well apparent. Growth of the recirculations is linked to the increasing lateral non-uniformity of the flow (i.e. increased lateral velocity differences), a pattern that was also mentioned by Broekema (2020).

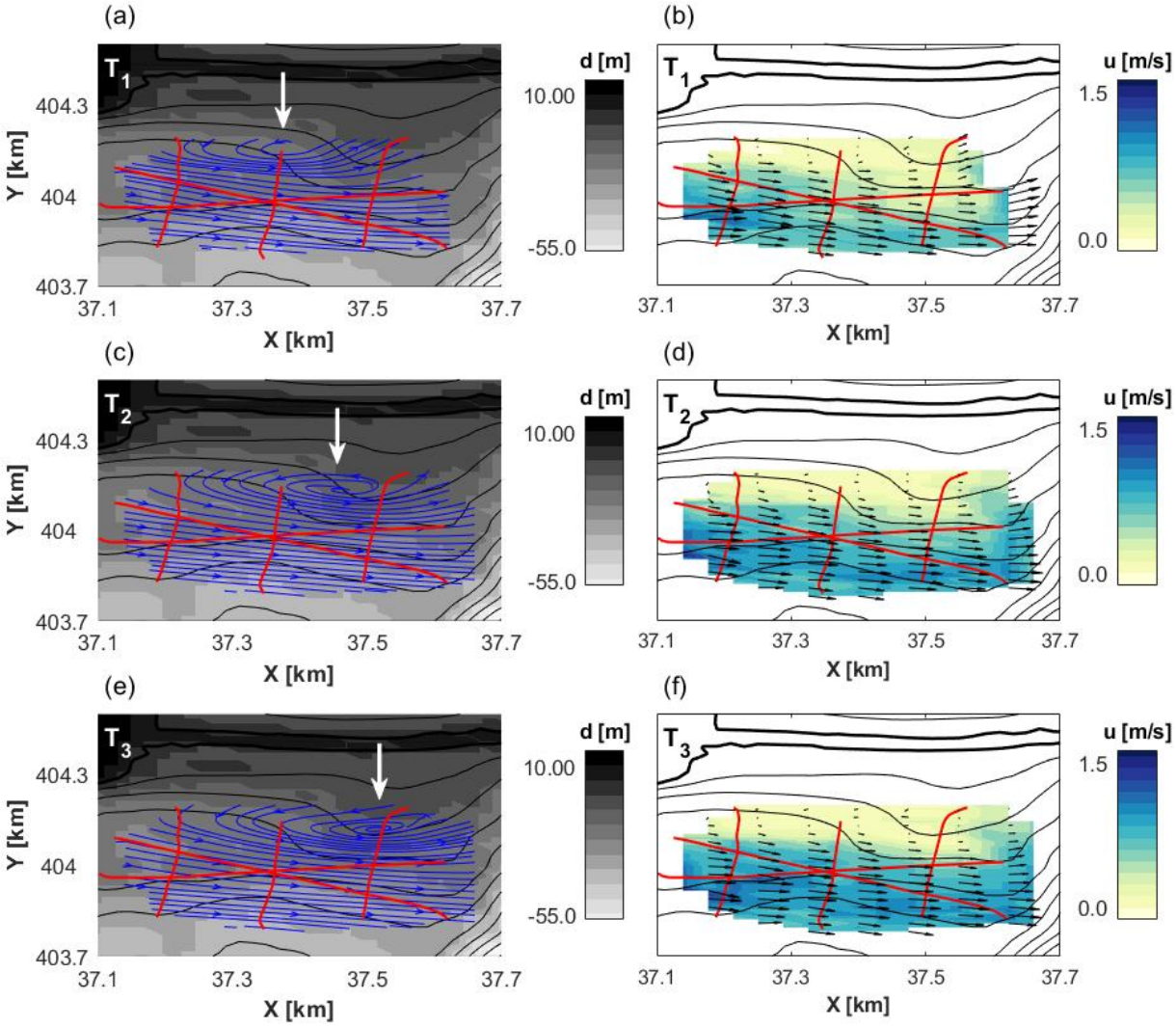

Figure 4.19: Streamlines (left panels) and depth-averaged velocity magnitude (right panels) at the Roompot inlet for three different stages of the tidal cycle: 3 hours before maximum flood (a-b), 2 hours before maximum flood (c-d), and 1 hour before maximum flood (e-f). White arrows indicate the streamwise propagation of a recirculation zone. The greyscale in the left panels denotes the water depth, and the colormap in the right panels the velocity magnitude.

Similarly, streamlines and depth-averaged flow velocities are also plotted for Area B close to the scour hole during maximum flood. Return currents adjacent to the main flow are strong, with values in the order of 0.8 ms^{-1}. In front of the deepest part of the scour hole, streamlines contract and velocities of about 1.5 ms^{-1} were measured.

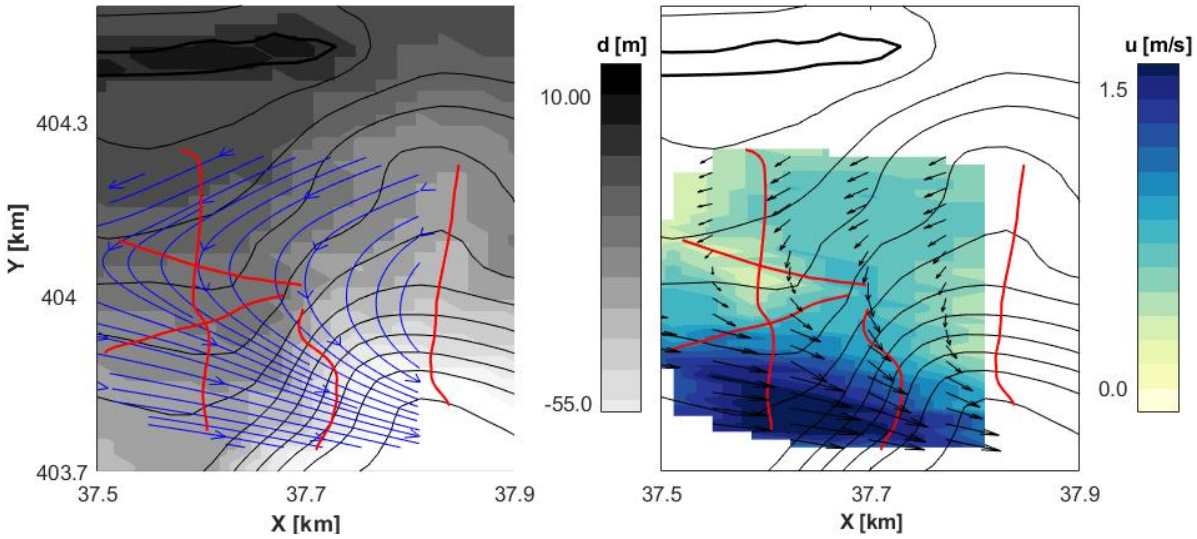

Figure 4.20: Streamlines (left panel) and depth-averaged velocity magnitude (right panel) near the Roompot scour hole computed over the entire water column.

Autocorrelation

The streamwise ADCP transect R_6 drawn in Figure 4.15 is used to get an impression of the turbulence scales. In Section 2.2.5 the autocorrelation was described which under certain conditions can be used to estimate characteristic time and length scales of turbulent motions. The first condition (a large mean velocity) is met as the transect is oriented (almost) parallel to the streamlines of the main current, with mean velocities equalling about 1 ms^{-1}. The second assumption (eddies are undisturbed during passage) is more difficult to satisfy because the measurements were not carried out from a stationary position. Despite correcting for the vessel's velocity along the transect using linear time interpolation, coherent motions are likely to be disturbed over a distance of 150 m. It may nevertheless be valuable to assess an order of magnitude of these motions, and to see whether similar scales can be identified from the RSIV results. In Equation 3.7 the normalized autocorrelation function is plotted for the three time interval T_1,T_2, and T_3. Evaluating Equation 2.9 yields values of $\mathcal{T} \approx 10$ s. Considering flow velocities in the order of 1 ms^{-1}, such time scales would lead to $\mathcal{L} \approx$ 10m. This is a rather low value for the large coherent structures, and seem more appropriate for the size of the vertical eddies. An alternative interpretation is that the length scales are related to eddies shed from the pillars between separate openings of the inlet. The pillars are about 5 m across, and similar-sized eddies generated by vortex shedding may grow in streamwise direction. This remains uncertain, as the observation of such a length scale assumes the autocorrelation to be estimated correctly. It may nevertheless be an interesting feature to study in future work.

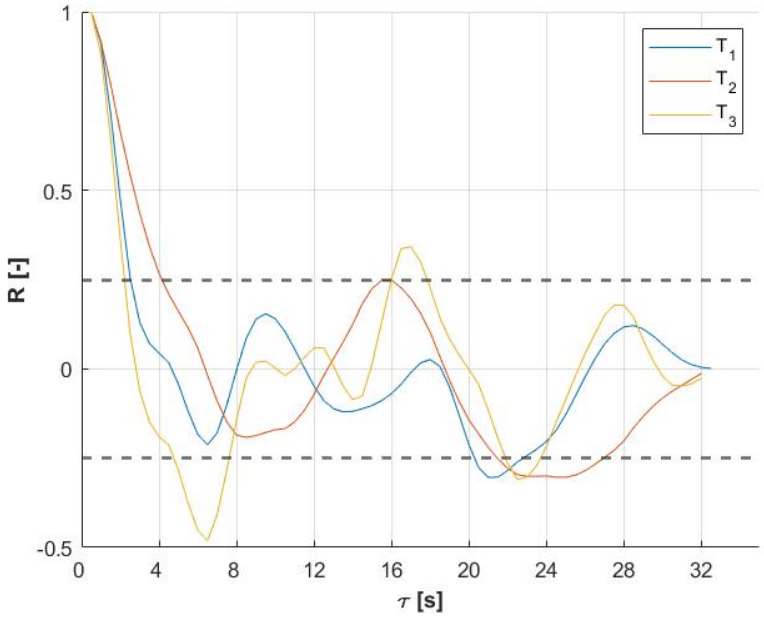

Figure 4.21: Normalized autocorrelation of velocities at intervals T_1 - T_3 along the transect parallel to the main flow (R_6). Dotted black lines indicate the 95% confidence bounds.

4.4 Conclusions

This chapter covered the analysis an interpretation of data obtained from drone imagery and ADCP measurements during a field campaign at the Roompot inlet. Prior to the campaign, a series of tests were carried out in a controlled environment to estimate the quality of the camera projection.

Image calibration

Laboratory experiments were carried out to determine the intrinsic parameters of the drone's camera, and to validate the camera projection for different marker configurations. The experiments were scaled to a domain of 2x2 m with GCPs located along the upper and right margins, similar to the configurations used at the Roompot area. Largest projection errors were associated with GCPs located only along a single axis on the upper margin of the images and without lateral variability, whereas markers placed in perpendicular direction significantly improved the accuracy of the transformation for each experiment. Even small variations in the order of a few percent of the total perpendicular distance already led to a reduction of projection errors by 15%. The projection was found to yield the most accurate results for markers distributed along both axes and including lateral variability, reducing errors by up to 40% compared to the most non-uniform GCP set-up.

Similar trends were derived at the Roompot inlet using three different configurations with increasing lateral variability of the positioned GCPs. Maximum errors between measured distances along the barrier's axis in all cases accounted for averages < 5 mm/px ($\sim 5\%$ of pixel dimension). The quality of the projection in this direction was found to be independent of lateral GCP distribution. The absence of GCPs in perpendicular direction however severely underestimated distances in downstream direction of the barrier. Although they

account for only 2% of the total streamwise distance, additional markers placed on either side of the bike way reduced lateral projection errors by up to 25%. The additional marker positioned about 100 m closer to drone improved the lateral projection by another 20%, thereby stressing the importance of a uniform GCP distribution.

RSIV sensitivity analysis

Being a relatively new technique over vast water surface areas, information on appropriate RSIV settings based on previous research was minimal. A series of options were explored to test the extent to which RSIV was assumed to be optimal for the current application. Geometric distortions restricted record durations larger than 30 s. IA sizes of 192 px (58x33 m^2) were found to yield the best compromise between vector resolution and SNR. Frame rates of 0.1 Hz over which autocorrelation between two image pairs was computed produced the most realistic results. Pretreatment methods such as high-pass filters or intensity capping did not noticeably affect the derived flow field.

Validation

The quality of the derived flow field from RSIV was first assessed using vector and image-based validation. Thresholds regarding maximum allowed velocities, standard deviations and a normalized median test were included to filter out velocities not related to motions on the water surface. RSIV accuracies were limited in areas subject to surface roughness or insufficient lightning.

Differences of about 0.2 - 0.6 ms^{-1} were found between overlapping RSIV and ADCP-derived velocities, which is mostly attributed to the different time intervals of measuring, the lack of ADCP data in highly turbulent flows, and the different time interval at which measurements were carried out.

Observations of large-scale flow patterns

Velocities ranged between 2 - 3 ms^{-1} close to the barrier, to 1 - 2 ms^{-1} at a distance of 250 m in streamwise direction. Largest deviations were found near the separate openings in the inlet, where insufficient lightning caused computed vectors to be either absent or underestimated. Global velocity profiles computed over horizontal and vertical transects within the main flow generally showed expected velocity gradients of the order $\mathcal{O}(10^{-3})$, indicating strong horizontal shear in the domain.

The temporal evolution of flow non-uniformity was well captured by the ADCP measurements across several lateral transects within the domain. Lateral velocity gradients decreased in streamwise direction, along with a spatial growth of the mixing layer towards the scour hole. A large recirculation zone was shown to develop between $T1$ - $T3$, leading to strong return currents close the scour hole. They are accompanied by streamline contraction on the interface of the main flow and adjacent water.

5 Discussion

The objective of this research is to develop a new method to estimate the horizontal flow field for large-scale free surface flows. The results and analysis from the data collected during the field campaign have shown that RSIV can be a valuable asset to the study on surface flow characteristics. This chapter further elaborates on the interpretation of the results in Section 5.1. A discussion on the relation of the observed horizontal flow field to scour development follows in Section 5.2. In Section 5.3, the performance of the RSIV application is reviewed.

5.1 Discussion on observed large-scale flow patterns

5.1.1 Quality of measurements

Results from Chapter 4 showed that RSIV-derived velocities over the water surface are consistent and generally well estimated, with values ranging between 1 - 3 ms^{-1} along a distance of 250 m east of the barrier. Highest flow velocities were found near the inlet. In Bijlsma et al. (2017) and Mooyaart et al. (2014), peak velocities of respectively 4 ms^{-1} and 3.3 ms^{-1} were reported during flood conditions. Similar values around the gate openings were derived from ADCP measurements and numerical simulations performed by O'Mahoney et al. (2020). The deviation in peak velocities was explained by the blockage of sunlight by the barrier, thereby reducing lightning contrast between the surface features and the surrounding environment. It is in this part of the flow where momentum exchange between the strong current entering the estuary and the adjacent flow is limited. Velocities within the first few meters from the barrier are therefore higher than elsewhere but could not be estimated accurately. The RSIV-derived flow field is changing in streamwise direction, reaching average values of about 1 - 2 ms^{-1} over the remaining 200 m. Momentum exchange with the adjacent waters cause a deceleration of the flow, and regions of high shear start developing. Similar velocity profiles are measured by ADCP, but are less gradual and generally contain smaller values of about 0.4 - 0.6 ms^{-1} in streamwise direction and 0.2 - 0.5 ms^{-1} in lateral direction. Differences between velocities are thought to originate from three (primary) sources:

1. The different time intervals in which measurements were carried out. Measuring at different time intervals can quickly lead to large velocity differences. ADCP data was also absent in very turbulent parts of the flow, with increasingly missing values for epochs close to maximum flood. In Figure 4.14 flow velocities measured with ADCP between T_1 - T_3 therefore showed only a marginal velocity increase. If average velocities over the streamwise and lateral transect as derived from RSIV are assumed to be about 1.5 ms^{-1} during maximum flood, then velocities increase with $\sim$0.25 ms^{-1} every hour from slack tide onward. Adding this rate to the values measured 3 hrs before maximum flood (at T_1) would give peak flow velocities that are indeed close to 1.5 ms^{-1} in these sections of the flow.

2. A non-logarithmic vertical velocity profile. RSIV velocities estimated over the water surface were validated by ADCP measurements averaged over the upper 2.5 m of the water column. It is unlikely that the complex flow at the Roompot inlet follows a logarithmic velocity profile over the water column,

which may suggest that significant velocity variations over small depth intervals are present. Tracers were also assumed to be representative surface features to follow the direction of the flow, but deviations caused by e.g. diffusion of foam possibly exist.

3. Record duration. A duration of 30 s was selected as the most appropriate video length over which velocities were time-averaged, whereas ADCP data were interpolated over a duration of 12 min. The RSIV-derived velocities are therefore more sensitive to local variations in the flow. This may for example explain the large velocity anomaly evident in the middle of the compared flow fields (Figure 4.14).

5.1.2 Developing non-uniformity of the flow

ADCP measurements along the three lateral transects in Area A showed an increase in the lateral velocity gradient, both temporally (between T_1 - T_3) and spatially (from R_3 - R_5). The increase in flow non-uniformity between slack water and maximum flood around the scour hole was previously demonstrated by Broekema (2020), and was shown in this thesis to already develop far upstream. In his dissertation, Broekema (2020) define a ratio between advective momentum flux and lateral shear stress, which is dependent on the ratio between the mixing layer width and a horizontal length scale. It is expressed as

$$\xi \propto a^{-2} \frac{u_a^2}{\Delta U^2} \frac{\delta}{L_H}, \tag{5.1}$$

where a is a proportionality constant of the order $\mathcal{O}(10^{-1})$ (Rodi, 1980), and $L_H = H/c_f$ is a horizontal length scale (Uijttewaal and Booij, 2000). Typical values for ξ using the values found in this thesis are of the order $\mathcal{O}(10^{-1})$, thus indicating that flows are indeed dominated by lateral shear stress. Whether or not such a conclusion can also be drawn from the RSIV analyses is yet to be sought after. From the current results lateral gradients were well apparent, though it would require multiple videos to evaluate their temporal development over a tidal cycle.

The increase in flow velocities between T_1 - T_3 measured by ADCP in Area A was shown to lead to the development of a large recirculation zone of which its centre migrates in streamwise direction. Streamlines between the main flow and the recirculation zone increasingly contract, providing additional space for the structure to also develop laterally. This supports the temporal evolution of lateral velocity gradients towards maximum flood. Similar behaviour was observed in Area B, where flow contraction is associated with strong return currents.

5.2 Relation to scour development

Although much research is devoted to scour holes in the vicinity of hydraulic structures, numerical models and experimental set-ups are often limited to either 2D configurations or simplified 3D geometries. In Chapter 2 a brief overview of important advances in scour hole prediction was provided, yet generally involved the assumption of a uniform upstream flow. Broekema (2020); Üşenti (2019); van de Zande (2018) all studied the implications for scour development in case the upstream flow is subject to (large) shear, i.e. $\xi \leq 1$. Using this information, the results on surface flow velocities derived in this thesis can add to the understanding of scour development at the ES-SSB via the interpretation of the following two observed features:

1. Mean flow velocity. Velocities derived from RSIV showed a jet-like flow structure, with velocities up

to 3 ms^{-1} close to the inlet and strong lateral gradients. In the centre of the main flow relatively high velocities persist at large distances from the barrier, and therefore maintain a high potential to erode sediment, further corroborated by the non-linear relation between flow velocity and bed shear stress demonstrated in previous studies.

2. Lateral horizontal shear. In Chapter 2 it was concluded that hydraulic loading on the bed is not necessarily greater in the main flow where flow velocities are highest, but can also have a large contribution to scour in the shear layers. Measuring the temporal development of flow non-uniformity over a tidal cycle can therefore add to the study on scour for environmental flow applications.

5.3 Discussion on RSIV performance

5.3.1 General remarks

The main component within the framework of this thesis is the development of RSIV for large-scale free surface flows, with a particular focus on the quality of the derived flow field. RSIV has shown to be a powerful tool to rather accurately estimate surface flow velocities on a large scale. The RSIV process appeared to be insensitive to filtering techniques and applied velocity limits. The method is therefore not necessarily case dependent but may be applicable to a wider range of environmental flows. In the following the most important elements of the RSIV procedure are discussed in more detail. The information can be used for further developments of the RSIV process.

The accuracy of the estimated flow field varies spatially, depending on the obliqueness of the image distortion, seeding density and distribution, local illumination and other factors. For instance, image perspective distortion is not uniform: objects closer to the camera are better resolved than those in the far field. Also, non-uniform seeding densities over the area may result in inadequate flow visualization. Kim (2006) conducted a thorough sensitivity analysis for image velocimetry to estimate river discharges. The relative contribution of the elemental errors to the final results was found to be mostly affected by the camera projection, seeding density, and sampling time. These will be discussed throughout this section.

5.3.2 Improvements on the camera projection

The constraint to accurately convert the camera's raster data to world coordinates over a vast body of water was a limitation well known in advance. For both Area A and Area B the distance between potential GCP locations and flow features that were to be studied proved to be a fundamental challenge for the accuracy of the camera projection. Choices on the distribution of GCPs around the domain were therefore thoroughly considered during the preparations for the field campaign. Solving for the camera parameters was a non-trivial task, and a certain loss of geometric integrity from camera distortions was inevitable. The elements of which the camera projection is composed of will be discussed separately.

Spatial GCP distribution

For Area A a high marker density across the barrier could be established, effectively mapping the world coordinates in the north-south direction with an error smaller than 1% with respect to the distances measured by GPS. Adding lateral variability in the GCP configuration did not significantly improve the projection

along the axis, but was demonstrated to be of vital importance if distances in streamwise direction were to be estimated accurately. The conversion to world coordinates for Area B was demonstrated to lead to large projection errors. Too much spatial information on the water surface was missing, despite the dense marker distribution on the dam.

Solving for the camera matrix

A limitation to the applied projection procedure is the assumption that all GCPs were situated at the same elevation (Z =0) in the imaged plane. The primary reason for this approach is the lack of uniformly placed GCPs from which the camera extrinsics could not be accurately derived from. The homography matrix was easily inverted because there was sufficient spatial distribution for a relatively solid 2D projection, allowing to solve for fewer degrees of freedom in the camera projection procedure. In principle, only 4 well-distributed GCPs should suffice for the inversion, as long as they are not collinear (i.e. are not located on the same line). This inversion indicates that in order to rectify the results from the image processing, it is possible to transform coordinates to the horizontal plane using at least four known GCPs defined at the water-surface plane.

To resolve the full camera matrix at least 10 well spread GCPs and their 3D coordinates in the real world will be then necessary (Fujita and Kunita, 2011; Le Boursicaud et al., 2016). Such a transformation is required for applications with significant water level gradients or strong topography, where height differences are relatively large with respect to the elevation of the camera.

Camera tilt angle

The camera's angle with respect to the area is a key parameter in the orthorectification process. Ideally, the camera should be positioned in the nadir of the imaged plane to limit the transformation corrections. Capturing a surface the size of areas considered with enough GCPs required a viewing angle of 60 - 70 °, even at the maximum allowed drone elevation of 120 m. Perspective errors for such angles are inevitable, and may lead to critical inaccuracies. Kim (2006) reported on the impact of oblique angles to the free surface plane on large-scale PIV measurement accuracies. They demonstrated that large angles should be avoided because orthorectification of images is difficult for significant camera tilt. Similar experiments were performed by Hauet et al. (2008), where two different angles showed large differences in the camera projection (Figure 5.1). Image (a) and image (c) correspond to the same condition of discharge and seeding, but the simulated recorded images were created with tilt angles of 55° and 70 ° respectively. After orthorectification and reconstruction of the images, the undistorted images look different. In the far field of the image (d), the patterns are not well reconstructed, with increase coverage and fuzzy edges. Despite a large camera angle used in this study the projection distortion was believed not to affect the flow field much. A combination of sufficient camera resolution, high feature density and well-distributed GCPs in the far-field of the camera's footprint (the latter resulting in detailed spatial information at the more distorted pixels) are believed to compensate for the large tilt angle.

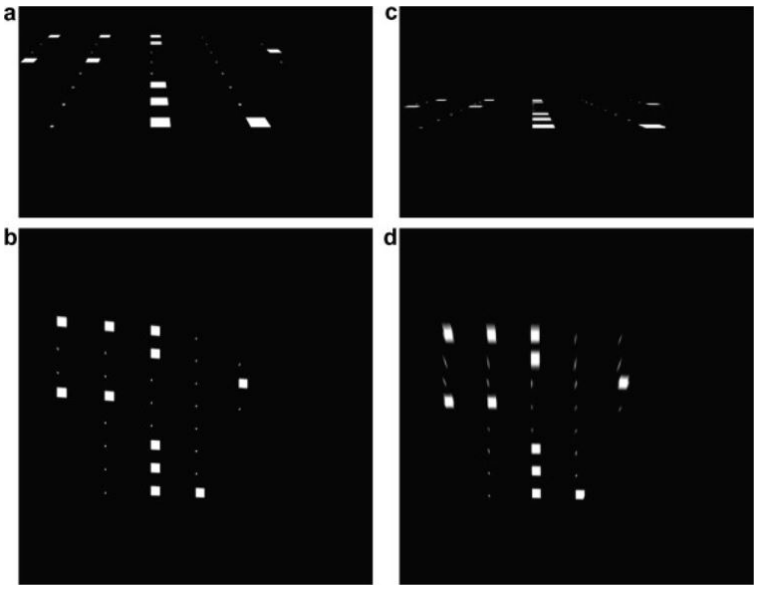

Figure 5.1: Images of the same situation recorded with two different tilt angles (55° for image (a) and 70° for image (c)) and the corresponding undistorted images.

Geometric distortions

Another constraint introduced by filming with a drone is the geometric error that arises from the rotation and translation of the camera. In fact, this issue has a much larger contribution to the total error budget of RSIV-derived surface velocities than only the projection error. This was attempted to correct for by subtracting a mean velocity vector computed on the barrier and outside the domain from the velocities at the water surface. Correcting for the distortion by subtracting a constant value is assumed to be justified because these velocities are non-physical in nature and therefore cannot originate from a source other than geometric effects. Geometric distortions however are not consistent throughout the domain, with larger deviations at increasing distances from the camera. Much of the flow is centered in the image and hence is less sensitive to rotational motion. It is likely that in some parts of the flow subtracting a mean value of 0.25 ms^{-1} leads to velocities that are not entirely correct. Being a small number however, the flow field will not be greatly affected by small changes in computed mean values.

5.3.3 Seeding density

High seeding densities were often present in the current application. For Area A boils were abundantly available in the main flow. High seeding densities can however rarely be reached in natural environments, especially during low-flow conditions. Therefore, artificial tracers are often used to increase surface seeding during filming. Examples are the use of biodegradable materials such as wood chips or eco-foam (Detert and Weitbrecht, 2015; Tauro and Grimaldi, 2017). In environments with large disparities in surface water temperature or sediment content, such as around confluences or in a river mouth, subtle differences in lightning properties or temperatures can be detected using high-resolution, sensitive (infrared) CCDs. The requirements for such sophisticated cameras cause successful applications currently to be limited, but promising results were found by Lin et al. (2019), Legleiter et al. (2017), and Kantoush et al. (2011).

5.3.4 Surface distortion

Noise on the images generated by e.g. capillary waves, surface glittering or shadows may decrease the SNR of the flow considered. In many applications this can potentially lead to a disturbed velocity field. Despite the obvious noise reflected in the velocities not corresponding to the tracer particles within the main flow, the two opposing currents near the Roompot inlet behaved independently. It is believed that boils within the main current dominated over other surface features. Derived vectors in the main flow are therefore not affected by the capillary waves. Poor or strong illumination may also restrict accurate vector computation between two image pairs when only natural light is used. As was shown at locations very close to the inlet, shadows on the water surface can significantly degrade image quality (Hauet et al., 2008).

6 Conclusions and recommendations

This chapter outlines the key findings obtained from the research study. In Section 6.1 the research questions that were introduced in Chapter 1 are answered. Recommendations for further research and improvement of the current work will then be described in Section 6.2.

6.1 Conclusions

The research objective of this thesis was to study large-scale horizontal flow patterns near the Roompot inlet by developing a remotely sensed image velocimetry method. The research questions are answered based on the results derived in this thesis.

6.1.1 Subquestions

1. Which hydrodynamic processes describe the flow patterns and development of scour holes near the Roompot inlet?

Chapter 2 thoroughly discussed the theory on shallow water dynamics, characterized by horizontal length scales much greater than the water depth. Waters from the North Sea entering the Eastern Scheldt estuary are highly contracted by the semi-open structure of the ES-SSB, and the flow shows similarities to that of a classical 2D jet. Close to the barrier, the flow is unaffected by the waters in the estuary, limiting momentum exchange and maintaining velocities up to 4 ms^{-1} . Mixing layers induced by transverse shear between contiguous flows of different velocity develop in streamwise direction. Characteristic properties of the shallow mixing layer are the downstream decrease of the velocity difference, the decreasing growth rate of the mixing layer width and the shift of the center of the mixing layer to the low velocity side. Bed protection was applied to a distance of about 600 m from the barrier to account for these high stresses. Recent surveys around the Roompot inlet have shown that scour processes are still ongoing even though expected equilibrium scour depths have already been reached. The ongoing development of the scour holes may ultimately be a threat to the stability of the barrier. Broekema (2020) studied the relevant processes that contribute to this unexpected behaviour. During horizontal contraction of the jet, flow separation near the bed of the scour hole is suppressed and high flow velocities in the streamwise direction are maintained. The cyclic variations in lateral non-uniformity affect turbulence intensities and subsequent mixing of mass and momentum. The presence of a scour hole may therefore enhance additional scour development in two ways: i) the centerline velocity remains high due to horizontal convergence, and ii) the influence of the lateral stress increases with changing bed slopes through a destabilization of the flow.

2. How can drone images and ADCP measurements be successfully obtained to study the relevant flow phenomena?

One of the most fundamental concepts discussed in this thesis is the extent to which the projection matrix is affected by different GCP configurations. These GCPs were required to transform image coordinates

to a world reference system. A water surface area of about 250x250 m was imaged with a drone from a stationary position. The limited possibility to deploy well-distributed GCPs across the area was first studied in a controlled laboratory setting, in which different marker configurations were tested to resemble set-ups intended to be used at the Roompot inlet. In the experiments a domain of 2x2 m was imaged. Markers were positioned on the upper and right margin of the images that corresponded to the barrier's axis and the dam parallel to the flow direction, respectively. Largest projection errors found in the experiments were associated with GCPs positioned along a straight horizontal line, whereas laterally varied markers significantly improved the accuracy of the transformation. Even small variations in perpendicular direction contributed to a better quality of the transformations. Experiments with improved measurements and additional markers configurations are required to better quantify the projection errors for future studies on the topic.

A selection of tested configurations was applied to the Roompot area, including a dense marker distribution on the barrier's axis. Similar to the experiments, the results showed that adding lateral variability (on the barrier's bike way) as small as a few percent of the total lateral distance was essential for more accurate projections. The lack of markers spread evenly throughout the domain however restricted solving for the full camera matrix, and instead the homography between the physical and imaged planes was computed. The homography assumes a planar transformation, even though the markers and the water surface were not positioned on the same elevation. With a camera altitude of 120 m, projection errors caused by these height differences of about 10 m are assumed to be small with respect to the geometric errors. These geometric distortions generated by the continuous motion of the camera caused limited the duration of the RSIV record. RMS errors between measured and estimated distances significantly contributed to the global projection errors for time-averaged flow fields exceeding 30 s.

3. What information can be subtracted from the RSIV-derived flow field and what is the quality of the data?

Post-processed surface velocities showed values that are expected within the domain, and generally agreed with results from previous research. Global velocity profiles computed along horizontal and vertical transects within the main flow showed expected velocity gradients. Geometric distortions and (to a smaller extent) errors in the projection matrix contributed to global errors. They were accounted for by subtracting a mean velocity value estimated over the area not related to the flow. Velocities ranged between 2.5 - 3 ms^{-1} close to the barrier, to 1.5 - 2 ms^{-1} at a distance of 250 m in streamwise direction. Largest deviations were found near the separate openings in the inlet, where insufficient lightning caused computed vectors to be either absent or underestimated. Differences of about 0.2 - 0.6 ms^{-1} were generally found between overlapping RSIV and ADCP-derived velocities, which were mostly attributed to the different time intervals of measuring, the lack of ADCP data in highly turbulent parts of the flow, and the depth difference over which velocities were computed.

Natural tracers should be abundantly available for the RSIV algorithms to be detected. Within the main flow, these tracers in the form of boils provided overall favorable seeding density and lightning properties for autocorrelation between image pairs to be estimated. For parts of the flow with a lack of generated boils, the RSIV procedure could not be applied. Information adjacent to the main flow in Area A (e.g. to study the return current) was therefore limited using RSIV. Depending on the scale of the domain, artificial seeding

may provide a solution to estimate flow velocities in these areas for future applications.

4. To what extent can the RSIV and ADCP data be used to quantify large-scale horizontal flow patterns at the Roompot area?

Generally speaking, the RSIV data from Area A offered a representative flow field from which large-scale velocity distributions were easily derived. They provided a first order approximation of the horizontal flow structure, without the demand for expensive and time consuming single-point measurements. The flow field was characterized by a jet-like structure, with large mean centreline velocities and strong lateral gradients observed up to a distance of about 250 m from the barrier.

From the normalized autocorrelation between ADCP measurements in the main flow (Figure 4.21) the size of coherent structures was estimated in the order of 10 m. Although small and likely not related to large 2DCS, they may be associated with vertical vortices or structures that originate from grid turbulence at the inlet's pillars. This interpretation should be treated carefully and regarded as an order of magnitude estimation, because the applied method using linear time interpolation to compensate for the vessel's velocity is sensitive to errors. The temporal evolution of flow non-uniformity was well captured by the ADCP measurements. Lateral velocity gradients computed across several lateral transects within the domain increased between 3 hrs and 1 hr before maximum flood (T_1 - T_3). At each interval lateral velocity gradients decreased in streamwise direction, along with a spatial growth of the mixing layer towards the scour hole. A large recirculation zone was shown to develop between the time intervals, leading to strong return currents close the scour hole. These currents are accompanied by streamline contraction on the interface of the main flow and adjacent water. Flow contraction and associated large lateral gradients during maximum flood were also observed on the upstream edge of the scour hole.

Temporal information on the development of the flow field over a tidal cycle was not estimated using RSIV because images were obtained during a single time interval of 30 s. Considering the adequate accuracy of the flow velocities, it is expected that this information can nevertheless be subtracted over a tidal cycle. This assumption can be tested with additional drone flights over the area using the approach described in Chapter 3.

6.1.2 Main question

"How can remotely sensed image velocimetry be developed to estimate surface flow velocities for large-scale environmental flow applications?"

This thesis addressed the study on large-scale flow structures around the Roompot inlet, one of the three inlets that form the ES-SSB. The flow on the scale that was studied is characterized as shallow because the horizontal length scales greatly exceed the water depth. Dominating processes develop in the horizontal plane and hydrodynamic properties of the flow can therefore be obtained by measuring surface velocities. Information on the horizontal flow structure was expected to contribute in understanding the relation between the large-scale flow structure and ongoing scour. The aim of this thesis was therefore to develop a remotely sensed image velocimetry method to estimate surface flow velocities for large-scale environmental flow applications.

The Roompot area was first studied using satellite images to obtain information on its spatial extent, characteristic flow features and the possibility to distribute GCPs across the domain. Laboratory experiments

were carried out to test a series of marker configurations matching the GCP distributions intended to be used for the field application. Projection errors for these different configurations helped in assessing the expected quality of the various projections between image and world coordinates. A checkerboard experiment was conducted in order to retrieve the camera specific intrinsic parameters required to undistort images via lens correction.

During the field campaign ADCP data and images were collected in (partially) overlapping areas of the flow to allow the RSIV-derived flow field to be validated. GCPs were positioned along the margins of the images with as much spatial variability as could possibly be applied using the information from the analyzed satellite images.

The uneven GCP distribution imposed restrictions on solving for the full camera matrix, and the homography between the imaged plane and physical space was computed instead. The assumption of GCPs to be positioned on the same plane was justified because (i) the projection errors were found to be relatively small with respect to geometric errors, and (ii) variations in the water level gradient and topography in the area were assumed negligible compared to the elevation of the drone. Calibrated images were analyzed with PIVLab by autocorrelating displacements of natural tracers (boils) between image pairs. An analysis on different settings in PIVlab was carried out to study the sensitivity of the derived flow fields to choices on e.g. record duration, interrogation sizes, and frame rate. Geometric distortions as a result of rotations and translations of the drone during filming were found to be the greatest error source, limiting the time duration over which RSIV velocities were computed to 30 s. Selecting a frame rate of 10 fps and an interrogation size of 192x192 px provided the most accurate results. Pretreatment methods such as the application of a highpass filter did not affect to the quality of the flow field. This was also shown in the section on image validation where the effect of different velocity filtering techniques on the derived flow velocities was studied in more detail. The flow fields appeared to be insensitive to changes in velocity limits, indicating that the developed RSIV method may not be restricted to the flow through the Roompot inlet. This notion is further corroborated by the additional analysis on the sensitivity analysis described in Appendix E.1, where a variety of pretreatment options in PIVlab did not lead to improved results. In the following section a series of recommendations are provided to help developing the RSIV procedure for future research.

6.2 Recommendations

6.2.1 Future RSIV applications

The results from this thesis led to the conclusion that RSIV can be a valuable and promising tool to approximate the flow field around hydraulic structures. Under certain conditions, the collection and processing of drone images for RSIV is a cheap and fast procedure. Of course, drone recordings introduce additional challenges with respect to stable cameras mounted on a platform. With mobile filming, general restrictions to weather conditions, camera angle, and GCP distribution become ever more important for the image calibration procedure. The following solutions and recommendations are proposed for the RSIV process to be applicable to a wider range of applications:

Image stabilization

Geometric distortions were found to be the largest contributor to the global projection error. This is a challenge that applies to all sorts of mobile filming for RSIV purposes. Aiming for more favourable weather conditions (particularly with less wind) would obviously be a good choice, but can not always be realized. A solution to tackle rotational motion of the camera during image post-processing is therefore proposed. Pairs of images oriented differently can be stabilized by the projective transformation using the homography procedure discussed in Appendix B.1. Rather than mapping between the image plane and a physical plane, it can also be used to map between two image planes. On each single image frame of the RSIV recordings the positions of (at least) 4 GCPs should be detected with an automatic feature-detection algorithm. Each GCP requires to be well distinguishable, so that they create large contrasts in lightning properties with its surroundings. For example yellow or orange markers can be used to auto-detect corresponding color values. This method was attempted in this research, but the markers were not uniquely identified by the auto-detection algorithms. Figure 6.1 schematizes this procedure. Successful stabilization allows for longer time-averaging and smaller geometric errors, both of which are crucial for more accurate flow field estimates.

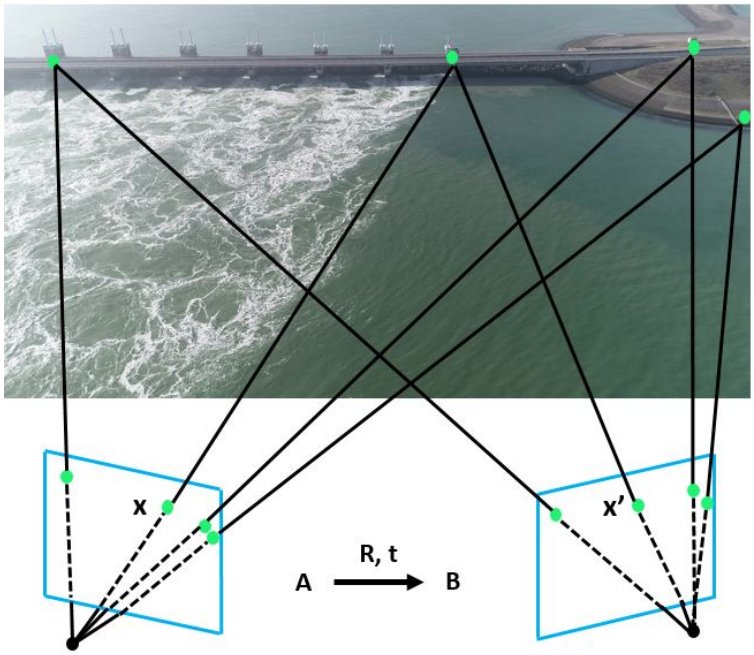

Figure 6.1: Schematization of stabilizing images. At least 4 GCPs are required to be distinguished on each image. The planar homography can then be used to map each coordinate x on image A to x' on image B.

Uniform GCP distribution

The requirement of a spatially uniform marker configuration around hydraulic structures is often less of a challenge for smaller sized areas. Examples are dams, sluices and groynes designed in rivers usually not larger than a few hundred meters across. The current research demonstrated that solving for the full camera matrix using a well-defined GCP distribution eliminates most of the projection errors. For larger applications such as at the ES-SSB or for monitoring nearshore processes, the lack of markers can only be partially compensated for. Although initially rejected, buoys attached to the safety line would make for excellent reference points

on the scale of these projects. Small variations in their positions during the time span of filming are easily outweighed by the benefit of adding spatial information to the projection matrix. Possible alternatives are stationary boats, platforms or structures positioned in the water that may be used as GCP. Adding only a few of these GCPs are expected to already provide sufficient projection quality, and are recommended for areas similar to area B studied in this thesis.

Multiple cameras

The current work uses a single camera to investigate key flow patterns at the center of basin. More cameras may be needed in the field to cover more areas for the study of hydrodynamic behaviour elsewhere. Also, loss of spatial resolution at increasing distances from the camera limits the accuracy of the RSIV results compared to zones near the camera. Another camera mounted on the barrier can be positioned such that flow processes near the inlet are studied in more detail, and to capture additional GCPs on the dam parallel to the main flow. In general, given the large size of Roompot area, several cameras are necessary to cover the entire range between the barrier and scour holes for a complete flow pattern study.

Artificial seeding

The identification of surface features is thoroughly discussed in the study. In addition to boils, artificial particles (e.g., the biodegradable particles) can be added to increase the autocorrelation between groups of tracers. This solution is less favourable for large areas, but was shown to work effectively in various fluvial studies (see Chapter 5 and Appendix D). For an extension of the current work on the development of RSIV, artificial seeding is recommended to for example estimate the flow field in floodplains where the limited flow depths adds restrictions to velocity measurements.

Coupling with (physical) models

For coastal processes or application for which wind has a large effect on the surface roughness, wind measurement and analysis in the field can be useful to eliminate wind effects on surface velocity. This may both increase the size of the area capable for RSIV analysis, and the accuracy of the RSIV-derived flow velocities.

6.2.2 Additional research on scour development

The complexity of hydrodynamics and scour development in environmental flows makes it challenging to quantitatively describe relevant physical processes. Field measurements collected in this thesis and by Broekema (2020) have provided sufficient data to qualitatively relate the different flow states to scour hole development. It is expected that an additional field campaign at the Roompot inlet would therefore not lead to alternative hypotheses or new fundamental knowledge on the subject using RSIV. Only stationary ADCP measurements with high temporal resolution (e.g. 1 Hz) may contribute to better estimates of flow characteristics such as the size of coherent structures. Because they can not be deployed on top of the bed protection, the question arises whether or not such data would be a valuable investment. Much progress however can be made with numerical models and experimental setups that account for the 3D geometry of scour holes. Although still in their infancy, recent developments previously discussed have emphasized on

the contribution of flow three-dimensionality to scour growth. Two approaches are recommended to extent this research:

1. Account for the complex geometry of the scour hole. Studies often only consider the upstream slope of a scour hole as a variable, thereby neglecting the effect flow non-uniformity has on the other slopes (and vice versa).

2. Study turbulence processes using detailed numerical models such as a large eddy simulation (LES). In LES the contribution of the large, energy-carrying structures to momentum and energy transfer are resolved, and only the effect of the smallest scales of turbulence is modeled. This may allow for large-scale unsteadiness of the flow to be simulated in great detail, including horizontal flow contraction and associated vertical flow attachment (Pope, 2000) that was found to be important for the scour processes near the Roompot inlet. In Appendix F an attempt was made to simulate these processes in OpenFOAM using experiments carried out by Broekema (2020). Further development of the simulations did not fit in the time frame of this thesis, but is assumed to be a valuable contribution to current research on the topic. Readers interesting in further developing these simulations may find useful information in the corresponding appendix. Data obtained at the Roompot inlet can be used as boundary conditions and validation of such models.

References

Abdel-Rahman, A. (2010). A review of effects of initial and boundary conditions on turbulent jets. *WSEAS transactions on Fluid Mechanics*, 4(5):257–275.

Baykal, C., Sumer, B. M., Fuhrman, D. R., Jacobsen, N. G., and Fredsøe, J. (2015). Numerical investigation of flow and scour around a vertical circular cylinder. *Philosophical Transactions of the Royal Society A: Mathematical, Physical and Engineering Sciences*, 373(2033):20140104.

Bijlsma, A., Tralli, A., Verbruggen, W., and Haas, P. (2017). Detailed hydrodynamics of the eastern scheldt storm surge barrier: validation of a cfd approach.

Bilajbegović, A., Leu, E., and Mulić, M. (2007). Prednosti hibridnih globalnih navigacijskih satelitskih sustava. *Kartografija i geoinformacije*, 6(izv./spec.):221–233.

Breusers, H. (1966). Conformity and time scale in two-dimensional local scour.

Broekema, Y. B. (2020). Horizontal shear flows over a streamwise varying bathymetry.

Brown, R. G. and Hwang, P. Y. (2012). *Introduction to random signals and applied Kalman filtering: with MATLAB exercises*. J Wiley & Sons.

Chandavari, V. and Palekar, S. (2014). Diffuser angle control to avoid flow separation. *Int. J. Tech. Res. Appl*, 2(5):16–21.

Chu, V. (1983). Stability of turbulent shear flows in shallow channel. In *Proc. XX Congress IAHR, Moscow, 1983*, volume 3, pages 128–133.

Chu, V. H. and Babarutsi, S. (1988). Confinement and bed-friction effects in shallow turbulent mixing layers. *Journal of hydraulic engineering*, 114(10):1257–1274.

Daigle, A., Bérubé, F., Bergeron, N., and Matte, P. (2013). A methodology based on particle image velocimetry for river ice velocity measurement. *Cold regions science and technology*, 89:36–47.

Dal Sasso, S. F., Pizarro, A., Pearce, S., Maddock, I., and Manfreda, S. (2021). Increasing lspiv performances by exploiting the seeding distribution index at different spatial scales. *Journal of Hydrology*, 598:126438.

Date, A. W. (2005). *Introduction to computational fluid dynamics*. Cambridge University Press.

De Vries, S., Hill, D., De Schipper, M., and Stive, M. (2011). Remote sensing of surf zone waves using stereo imaging. *Coastal Engineering*, 58(3):239–250.

Detert, M. and Weitbrecht, V. (2014). Helicopter-based surface piv experiments at thur river. In *Proceedings of the International Conference on Fluvial Hydraulics (River Flow 2014), Lausanne, Switzerland*, pages 3–5.

Detert, M. and Weitbrecht, V. (2015). A low-cost airborne velocimetry system: proof of concept. *Journal of Hydraulic Research*, 53(4):532–539.

Di Mare, L., Klein, M., Jones, W., and Janicka, J. (2006). Synthetic turbulence inflow conditions for large-eddy simulation. *Physics of Fluids*, 18(2):025107.

Dracos, T., Giger, M., and Jirka, G. (1992). Plane turbulent jets in a bounded fluid layer. *Journal of Fluid Mechanics*, 241:587–614.

D'Errico, J. R. (2006). Understanding gridfit. *Information available at: http://www. mathworks. com/matlabcentral/fileexchange/loadFile. do*, 55:70–83.

Ettema, R., Fujita, I., Muste, M., and Kruger, A. (1997). Particle-image velocimetry for whole-field measurement of ice velocities. *Cold Regions Science and Technology*, 26(2):97–112.

Frisch, U. and Kolmogorov, A. N. (1995). *Turbulence: the legacy of AN Kolmogorov*. Cambridge university press.

Fujita, I. and Kunita, Y. (2011). Application of aerial lspiv to the 2002 flood of the yodo river using a helicopter mounted high density video camera. *Journal of Hydro-environment Research*, 5(4):323–331.

Fujita, I., Muste, M., and Kruger, A. (1998). Large-scale particle image velocimetry for flow analysis in hydraulic engineering applications. *Journal of hydraulic Research*, 36(3):397–414.

Gao, X.-S., Hou, X.-R., Tang, J., and Cheng, H.-F. (2003). Complete solution classification for the perspective-three-point problem. *IEEE transactions on pattern analysis and machine intelligence*, 25(8):930–943.

Ghidaoui, M. S., Kolyshkin, A. A., Liang, J., Chan, F. C., Li, Q., and Xu, K. (2006). Linear and nonlinear analysis of shallow wakes. *Journal of Fluid Mechanics*, 548:309.

Ghodsian, M. and Vaghefi, M. (2009). Experimental study on scour and flow field in a scour hole around a t-shape spur dike in a 90 bend. *International Journal of Sediment Research*, 24(2):145–158.

Guan, D., Melville, B. W., and Friedrich, H. (2014). Flow patterns and turbulence structures in a scour hole downstream of a submerged weir. *Journal of Hydraulic Engineering*, 140(1):68–76.

Hauet, A., Creutin, J.-D., and Belleudy, P. (2008). Sensitivity study of large-scale particle image velocimetry measurement of river discharge using numerical simulation. *Journal of Hydrology*, 349(1-2):178–190.

Heikkila, J. and Silvén, O. (1997). A four-step camera calibration procedure with implicit image correction. In *Proceedings of IEEE computer society conference on computer vision and pattern recognition*, pages 1106–1112. IEEE.

Hoffmans, G. J. and Booij, R. (1993). Two-dimensional mathematical modelling of local-scour holes. *Journal of Hydraulic Research*, 31(5):615–634.

Hoffmans, G. J. and Verheij, H. J. (1997). *Scour manual*, volume 96. CRC press.

Holland, K. T., Holman, R. A., Lippmann, T. C., Stanley, J., and Plant, N. (1997). Practical use of video imagery in nearshore oceanographic field studies. *IEEE Journal of oceanic engineering*, 22(1):81–92.

Huang, H., Dabiri, D., and Gharib, M. (1997). On errors of digital particle image velocimetry. *Measurement Science and Technology*, 8(12):1427.

Ingram, R. G. and Chu, V. H. (1987). Flow around islands in rupert bay: An investigation of the bottom friction effect. *Journal of Geophysical Research: Oceans*, 92(C13):14521–14533.

Issa, R. I. (1986). Solution of the implicitly discretised fluid flow equations by operator-splitting. *Journal of computational physics*, 62(1):40–65.

Jasek, M., Muste, M., and Ettema, R. (2001). Estimation of yukon river discharge during an ice jam near dawson city. *Canadian Journal of Civil Engineering*, 28(5):856–864.

Jin, T. and Liao, Q. (2019). Application of large scale piv in river surface turbulence measurements and water depth estimation. *Flow Measurement and Instrumentation*, 67:142–152.

Jirka, G. H. (2001). Large scale flow structures and mixing processes in shallow flows. *Journal of Hydraulic Research*, 39(6):567–573.

Johnson, E. D. and Cowen, E. A. (2017). Estimating bed shear stress from remotely measured surface turbulent dissipation fields in open channel flows. *Water Resources Research*, 53(3):1982–1996.

Kantoush, S., Sumi, T., and Murasaki, M. (2011). Evaluation of sediment bypass efficiency by flow field and sediment concentration monitoring techniques. *Journal of Japan Society of Civil Engineers, Ser. B1 (Hydraulic Engineering)*, 67(4):I_169–I_174.

Kantoush, S. A. and Schleiss, A. J. (2009). Large-scale piv surface flow measurements in shallow basins with different geometries. *Journal of Visualization*, 12(4):361–373.

Kim, H. S., Nabi, M., Kimura, I., and Shimizu, Y. (2014). Numerical investigation of local scour at two adjacent cylinders. *Advances in Water Resources*, 70:131–147.

Kim, Y. (2006). *Uncertainty analysis for non-intrusive measurement of river discharge using image velocimetry*. The University of Iowa.

Koopmans, H. (2017). Scour holes in tidal rivers with heterogeneous subsoil under anthropogenic influence. MSc thesis TU Delft, the Netherlands. *www.repository.tudelft.nl*.

Koutalakis, P., Tzoraki, O., and Zaimes, G. (2019). Uavs for hydrologic scopes: application of a low-cost uav to estimate surface water velocity by using three different image-based methods. *Drones*, 3(1):14.

Kraichnan, R. H. (1967). Inertial ranges in two-dimensional turbulence. *The Physics of Fluids*, 10(7):1417–1423.

Le Boursicaud, R., Pénard, L., Hauet, A., Thollet, F., and Le Coz, J. (2016). Gauging extreme floods on youtube: application of lspiv to home movies for the post-event determination of stream discharges. *Hydrological Processes*, 30(1):90–105.

Le Coz, J., Hauet, A., Pierrefeu, G., Dramais, G., and Camenen, B. (2010). Performance of image-based velocimetry (lspiv) applied to flash-flood discharge measurements in mediterranean rivers. *Journal of hydrology*, 394(1-2):42–52.

Legleiter, C. J., Kinzel, P. J., and Nelson, J. M. (2017). Remote measurement of river discharge using thermal particle image velocimetry (piv) and various sources of bathymetric information. *Journal of Hydrology*, 554:490–506.

Lesparre, J. (2006). The impact of the antenna mounting on the phase centre variation. In *EUREF Symposium*, pages 05–03.

Lilly, D. K. (1992). A proposed modification of the germano subgrid-scale closure method. *Physics of Fluids A: Fluid Dynamics*, 4(3):633–635.

Lin, D., Grundmann, J., and Eltner, A. (2019). Evaluating image tracking approaches for surface velocimetry with thermal tracers. *Water Resources Research*, 55(4):3122–3136.

Liu, X. and García, M. H. (2008). Three-dimensional numerical model with free water surface and mesh deformation for local sediment scour. *Journal of waterway, port, coastal, and ocean engineering*, 134(4):203–217.

Meinhart, C. D., Wereley, S. T., and Santiago, J. G. (1999). Piv measurements of a microchannel flow. *Experiments in fluids*, 27(5):414–419.

Mooyaart, L. F., Jonkman, S. N., De Vries, P. A., Van der Toorn, A., and Van Ledden, M. (2014). Storm surge barrier: Overview and design considerations. In *ICCE 2014: Proceedings of 34th International Conference on Coastal Engineering, Seoul, Korea, 15-20 June 2014*. Coastal Engineering Research Council.

Muste, M., Fujita, I., and Hauet, A. (2008). Large-scale particle image velocimetry for measurements in riverine environments. *Water resources research*, 44(4).

Muste, M., Hauet, A., Fujita, I., Legout, C., and Ho, H.-C. (2014). Capabilities of large-scale particle image velocimetry to characterize shallow free-surface flows. *Advances in water resources*, 70:160–171.

Nieuwstadt, F. T., Westerweel, J., and Boersma, B. J. (2016). *Turbulence: introduction to theory and applications of turbulent flows*. Springer.

O'Mahoney, T., de Fockert, A., Bijlsma, A. C., and de Haas, P. (2020). Hydrodynamic impact and power production of tidal turbines in a storm surge barrier. *International Marine Energy Journal*, 3(3):127–136.

Pan, Y. and Banerjee, S. (1995). A numerical study of free-surface turbulence in channel flow. *Physics of Fluids*, 7(7):1649–1664.

Pizer, S. M., Amburn, E. P., Austin, J. D., Cromartie, R., Geselowitz, A., Greer, T., ter Haar Romeny, B., Zimmerman, J. B., and Zuiderveld, K. (1987). Adaptive histogram equalization and its variations. *Computer vision, graphics, and image processing*, 39(3):355–368.

Poletto, R., Craft, T., and Revell, A. (2013). A new divergence free synthetic eddy method for the reproduction of inlet flow conditions for les. *Flow, turbulence and combustion*, 91(3):519–539.

Pope, S. B. (2000). *Turbulent Flows*. Cambridge University Press.

Qu, M. (2012). *Experimental studies of wireless communication and GNSS kinematic positioning performance in high-mobility vehicle environments*. PhD thesis, Queensland University of Technology.

Raffel, M., Willert, C., Wereley, S., and Kompenhans, J. (2007). Particle image velocimetry. 2 edn springer.

Rodi, W. (1980). Turbulence models and their application in hydraulics - A state of the art review. *NASA STI/Recon Technical Report A*, 81:21395.

Rodi, W. (1997). Comparison of les and rans calculations of the flow around bluff bodies. *Journal of wind engineering and industrial aerodynamics*, 69:55–75.

Roth, G. and Katz, J. (2001). Five techniques for increasing the speed and accuracy of piv interrogation. *Measurement Science and Technology*, 12(3):238.

Scarano, F. and Riethmuller, M. L. (1999). Iterative multigrid approach in piv image processing with discrete window offset. *Experiments in Fluids*, 26(6):513–523.

Shavit, U., Lowe, R. J., and Steinbuck, J. V. (2007). Intensity capping: a simple method to improve cross-correlation piv results. *Experiments in Fluids*, 42(2):225–240.

Socolofsky, S. A. and Jirka, G. H. (2004). Large-scale flow structures and stability in shallow flows. *Journal of Environmental Engineering and Science*, 3(5):451–462.

Spalart, P. R. (2000). Strategies for turbulence modelling and simulations. *International journal of heat and fluid flow*, 21(3):252–263.

Stenfert, J. (2017). Scour holes in heterogeneous subsoil: An experimental study to improve knowledge of the development of scour holes in heterogeneous subsoil. MSc thesis TU Delft, the Netherlands. *www.repository.tudelft.nl*.

Tabor, G. R. and Baba-Ahmadi, M. (2010). Inlet conditions for large eddy simulation: A review. *Computers & Fluids*, 39(4):553–567.

Talstra, H. (2011). Large-scale turbulence structures in shallow separating flows. PhD thesis TU Delft, the Netherlands. *www.repository.tudelft.nl*.

Tauro, F. and Grimaldi, S. (2017). Ice dices for monitoring stream surface velocity. *Journal of Hydro-environment Research*, 14:143–149.

Tauro, F., Porfiri, M., and Grimaldi, S. (2016). Surface flow measurements from drones. *Journal of Hydrology*, 540:240–245.

Taylor, G. I. (1938). The spectrum of turbulence. *Proceedings of the Royal Society of London. Series A-Mathematical and Physical Sciences*, 164(919):476–490.

Teledyne (2021).

Tennekes, H. and Lumley, J. L. (2018). *A first course in turbulence*. MIT press.

Thielicke, W. and Stamhuis, E. (2014). Pivlab–towards user-friendly, affordable and accurate digital particle image velocimetry in matlab. *Journal of open research software*, 2(1).

Uijttewaal, W. (2002). Lecture notes: Turbulence in hydraulics, TU Delft.

Uijttewaal, W. and Booij, R. (2000). Effects of shallowness on the development of free-surface mixing layers. *Physics of fluids*, 12(2):392–402.

Uijttewaal, W., Lehmann, D. v., and Mazijk, A. v. (2001). Exchange processes between a river and its groyne fields: Model experiments. *Journal of Hydraulic Engineering*, 127(11):928–936.

Üşenti, B. (2019). Scour hole formation for lateral non-uniform flow in non-cohesive sediments. MSc thesis TU Delft, the Netherlands. *www.repository.tudelft.nl*.

Van Baars, S. and Van Kempen, I. (2009). The causes and mechanisms of historical dike failures in the netherlands. *E-WAter journal, 2009*.

van de Zande, B. (2018). Jet behaviour in longitudinal deepening shallow flows: A case study to the eastern scheldt storm surge barrier. MSc thesis TU Delft, the Netherlands. *www.repository.tudelft.nl*.

Van Driest, E. R. (1956). On turbulent flow near a wall. *Journal of the aeronautical sciences*, 23(11):1007–1011.

van Heijst, G. (2007). Zelforganisatie van twee-dimensionale stromingen. In *conference; TOP-lezing TU/e; 2007-12-19; 2007-12-19*.

Van Prooijen, B. (2004). Shallow mixing layers. PhD thesis TU Delft, the Netherlands. *www.repository.tudelft.nl*.

van Prooijen, B. C. and Uijttewaal, W. S. (2002). A linear approach for the evolution of coherent structures in shallow mixing layers. *Physics of Fluids*, 14(12):4105–4114.

Verbeek, M., Labeur, R., and Uijttewaal, W. (2017). Large scale piv applied to flow interaction downstream a semi-open barrier. *4th International Symposium of Shallow Flows, Eindhoven (Netherlands)*.

Weitbrecht, V., Kühn, G., and Jirka, G. (2002). Large scale piv-measurements at the surface of shallow water flows. *Flow Measurement and Instrumentation*, 13(5-6):237–245.

Weitbrecht, V., Socolofsky, S. A., and Jirka, G. H. (2008). Experiments on mass exchange between groin fields and main stream in rivers. *Journal of Hydraulic Engineering*, 134(2):173–183.

Westerweel, J. and Scarano, F. (2005). Universal outlier detection for piv data. *Experiments in fluids*, 39(6):1096–1100.

Wieneke, B. (2017). *PIV uncertainty quantification and beyond*. PhD thesis, Delft University of Technology.

Wu, X. (2017). Inflow turbulence generation methods. *Annual Review of Fluid Mechanics*, 49:23–49.

Zhang, Z. (2000). A flexible new technique for camera calibration. *IEEE Transactions on pattern analysis and machine intelligence*, 22(11):1330–1334.

Zhao, Y., Chen, D., Yang, L., Li, X., and Tang, W. (2003). The principle and method of analysis of remote sensing application. *Beijing: Science Press*, 20:13.

Zhu, X. and Lipeme Kouyi, G. (2019). An analysis of lspiv-based surface velocity measurement techniques for stormwater detention basin management. *Water Resources Research*, 55(2):888–903.

Appendix A: details on the measurement campaign

This appendix includes additional information on the measurement campaign that was carried out around the Roompot inlet at March 1, 2021. It treats the required conditions of the measured data and equipment defined in advance. Details on the sailed ADCP transects and GCP positions are also provided.

A.1 Measurement conditions

Based on the research objective, several conditions were defined to assure the quality of the data obtained by the drones and ADCP measurements.

A.1.1 Date and time

The drone measurements require a sufficient amount of tracers to be visible on each image. For this reason, flow velocities through the barrier should be maximum for it to generate the most amount of foam/bubbles. Flood and spring-tide conditions are therefore preferred. Four different dates are considered based on the maximum water levels at the seaside of the Roompot inlet. Table 8 provides an overview of the suitable options aligned with rising tide conditions, taking into account daylight and regular working hours. Maximum flood occurs at around 16:00 hr on each proposed day.

Table 8: Possible date and times for the measurement campaign to take place.

Day	**Date**	**Max. water level w.r.t NAP (cm)**	**From**	**To**
Monday	15-02-2021	171	10:30	16:30
Monday	01-03-2021	196	10:30	16:30
Tuesday	16-03-2021	171	10:00	16:00
Wednesday	31-03-2021	201	10:00	16:00

A.1.2 ADCP measurements

- Sailed ADCP should cover a larger areal extent within the two domains.
- These mobile ADCP measurements should be carried out for a short period (on a time scale at which the flow is assumed to be more or less stationary), and not simultaneously with the drone measurements to avoid noise in the images.

A.1.3 Drone measurements

- The two drones considered are of the type DJI Phantom 4 Pro 2.0.

- Drones will be piloted from Neeltje Jans, see Figures A.1 and A.2.
- Weather conditions should be sufficient, i.e. it should be dry and clear. Moreover, a maximum wind power of 4 is allowed.
- Permitted maximum flight altitude is 120m with a maximum horizontal distance of 500m from the pilot.
- A permit above the ES-SSB is required and provided by the Province of Zeeland. Another one was requested via the ES-SSB coordinator upon agreement on the actual date of the measurement campaign.
- Three LiPo batteries per drone were available. Average flight time is about 20 min excluding time needed to return the drone back to the pilot.
- Certain fly restrictions apply to the area. Most importantly is a minimum distance of 75m to the N57 road.
- Pilot requires an ROC-exemption to be able to control the drone. He or she will mark the work spots and wear visible clothing (Figure A.3).

A.1.4 Image quality and post-processing

- The DJI Phantom 4 Pro 2.0 is equipped with a 20 megapixel camera.
- The drone is able to capture images in 4K resolution (3840x2160 px) at 30 frames per second (fps).
- A micro SD with a storage of capacity 128GB is equipped on the drone. Writing speed is $\geq$ 15 MB/s.
- The maximum angle of the camera is 84 degrees. The quality of the measurements will drop for larger viewing angles. Preparations were made to optimize a balance between this angle and (loss of) resolution.

A.1.5 GCPs and GNSS determination

- A total of 35 GCPs were marked on top of the barrier and on Neeltje Jans, see Figure A.7.
- GCPs should be sufficiently large and uniquely distinguishable on the images.
- The location of these GCPs are determined by a Trimble 8 GNSS system using post processed kinematic (PPK).

A.2 Measurement areas

The drone flights and ADCP measurements will be carried out at the landward side of the ES-SSB, near the northeastern Roompot scour hole. Two broad areas are studied over which the mixing layer can be quantified. Moreover, there should be sufficient ground control points (GCPs) available on each image to georeference the raster data to Earth coordinates. The first area is located close to the barrier with dimensions 300x450m (aspect ratio 2:3), where the natural tracers are expected to be well visible and the GCPs could be distributed more uniformly (Figure A.1). Figure A.1 shows the second entire area to be

covered, with dimensions 500x670m (aspect ratio 2:3). In order to optimize a balance between the camera footprint and ground sampling distance, the areas were determined using test flights in advance of the measurement campaign. Figure A.3 depicts the platform from which the drone will be piloted.

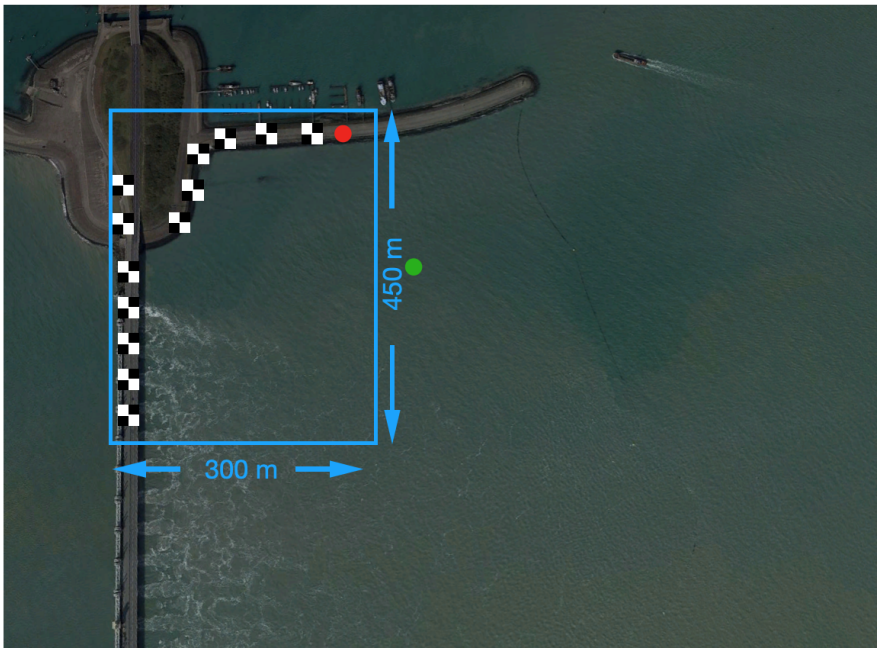

Figure A.1: First area close to the barrier. The chess-like patterns indicate the ground control points. The red dot marks the location of the drone pilot. The green dot indicates the fixed drone position during filming.

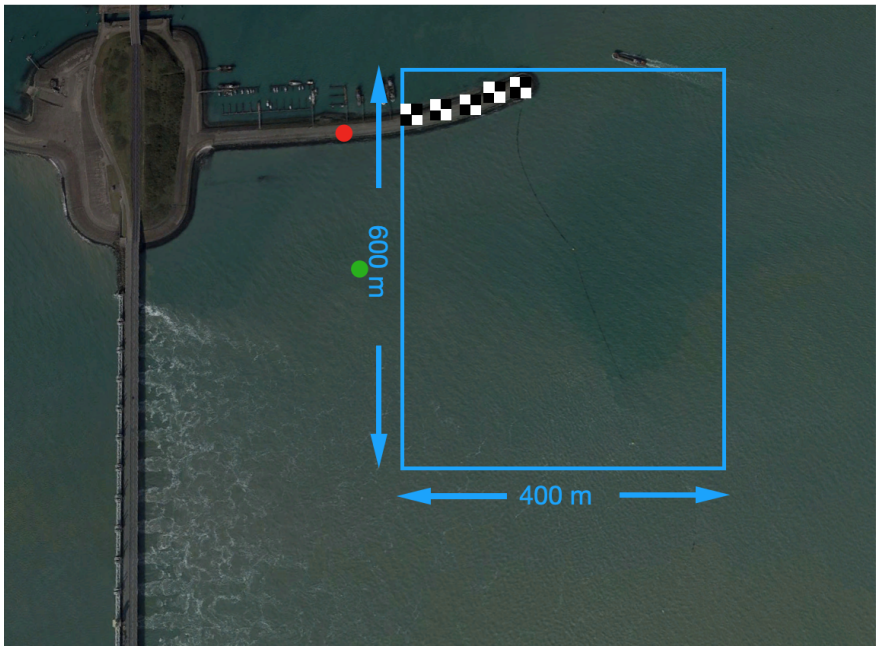

Figure A.2: Area close to the northeastern Roompot scour hole where a recirculation zone is present.

Figure A.3: Installing the pilot platform on the dam parallel to the main flow.

A.3 ADCP measurements

ADCP measurements on a sailing boat are proposed to validate the post-processed drone images. Since it is important to overlap the ADCP and drone measurements (i.e. to measure within the same time interval), without the generation of noise in the images caused by the boat, the measurements are conducted closely one after another. Transects are illustrated in Figures A.4 and A.5. Details of the sailing routes are shown in Figures 10 and 9. With mobile measurements the two relatively small domains can be sailed in about 12 min considering a sailing velocity of 4 m/s. This time window is sufficient to assume the flow to be stationary. The sailing routes are to be repeated four times per area (similar to the drone measurements), to include different stages within a tidal cycle. Even though the four sessions are performed over different time intervals, the complementary data is expected to be very useful to analyze general flow structures over a tidal cycle, and can be a great asset to the overall validation of the data. The vessel will depart at the inside port of Neeltje Jans, close to the Roompot inlet.

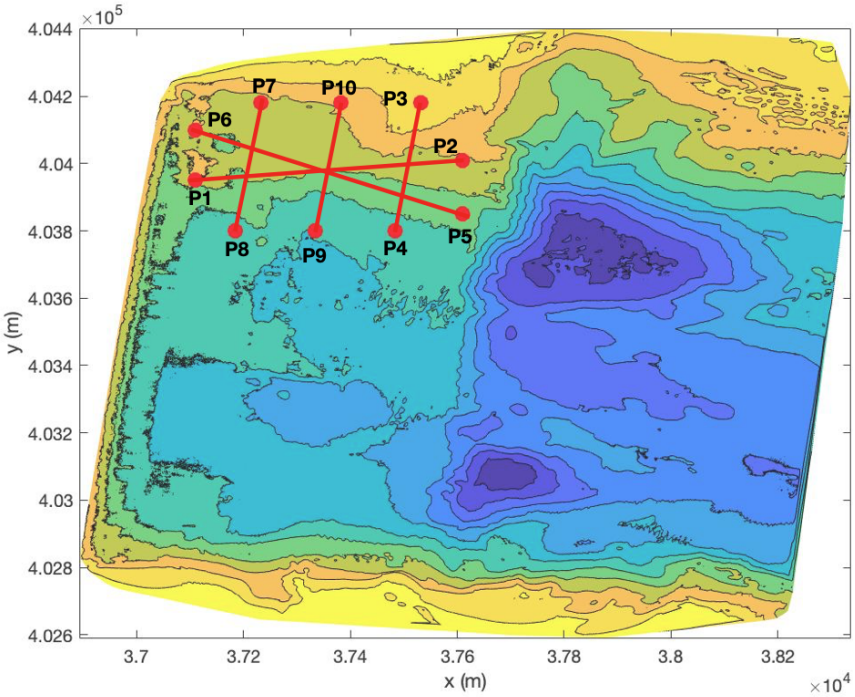

Figure A.4: Proposed transects for the first area located close to the barrier.

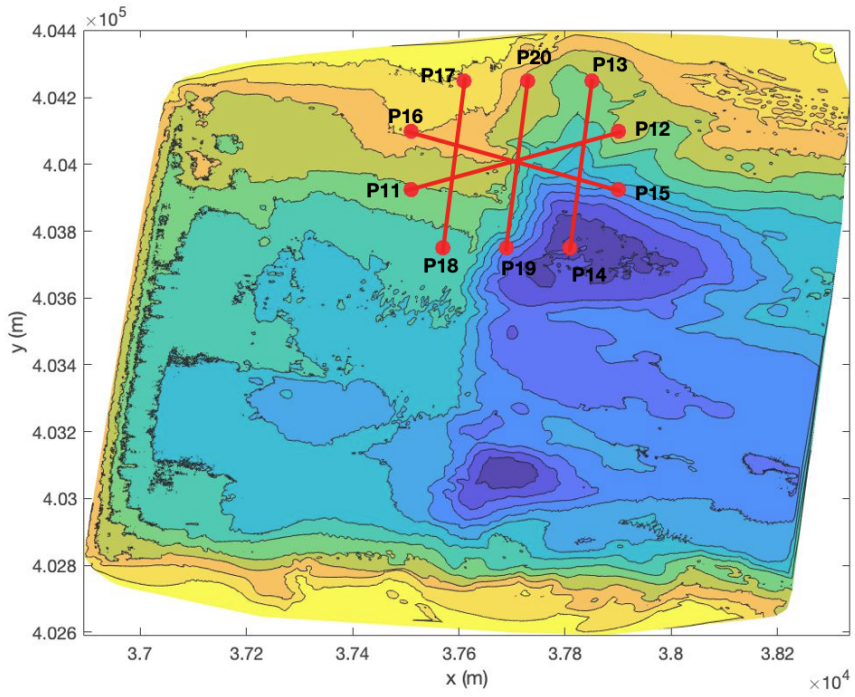

Figure A.5: Proposed transects for the second area located close to the Roompot scour hole.

Table 9: Distances and duration of the sailed transects.

Area 2				Area 1		
Route	**Distance [m]**	**Duration [s]**		**Route**	**Distance [m]**	**Duration [s]**
P1 to P2	427.5	106.9		**P11 to P12**	503.6	125.9
P2 to P3	158.1	39.5		**P12 to P13**	187.0	46.8
P3 to P4	501.6	125.4		**P13 to P14**	383.0	95.8
P4 to P5	196.8	49.2		**P14 to P15**	135.6	33.9
P5 to P6	427.5	106.9		**P15 to P16**	559.0	139.8
P6 to P7	180.3	45.07		**P16 to P17**	145.9	36.5
P7 to P8	501.6	125.4		**P17 to P18**	383.0	95.8
P8 to P9	120.0	30.0		**P18 to P19**	150.0	37.5
P9 to P10	501.6	125.4		**P19 to P20**	383.0	95.8
Total	3014.9	753.7		**Total**	2830.2	707.6

Table 10: Coordinates of the sailed transects.

Area 2					Area 1			
Route	**X**	**Y**	**ID**		**Route**	**X**	**Y**	**ID**
Route 1	37610	403925	P1		**Route 6**	37110	403950	P11
	38000	404100	P2			37610	404010	P12
Route 2	37950	404250	P3		**Route 7**	37532	404180	P13
	37910	403750	P4			37484	403800	P14
Route 3	38000	403925	P5		**Route 8**	37610	403850	P15
	37610	404100	P6			37110	404100	P16
Route 4	37710	404250	P7		**Route 9**	37232	404180	P17
	37670	403750	P8			37184	403800	P18
Route 5	37790	403750	P9		**Route 10**	37334	403800	P19
	37830	404250	P10			37382	404180	P20

A.4 GCPs and GNSS measurements

A sufficient amount of GCPs are required for post-processing the images. Since a uniform distribution of the GCPs within the domain can not be achieved over a large body of water, checkerboard markers of sizes 20x20 cm and 30x30 cm are positioned along the dam perpendicular to the barrier. No markers are allowed to be placed on top of the barrier because they may potentially hinder traffic crossing the N57 road. Instead, the road- and traffic signs on the bikeway parallel to this road are found to be convenient markers well visible from large camera distances. An example of the deployed GCPs on the barrier is shown in Figure A.6).

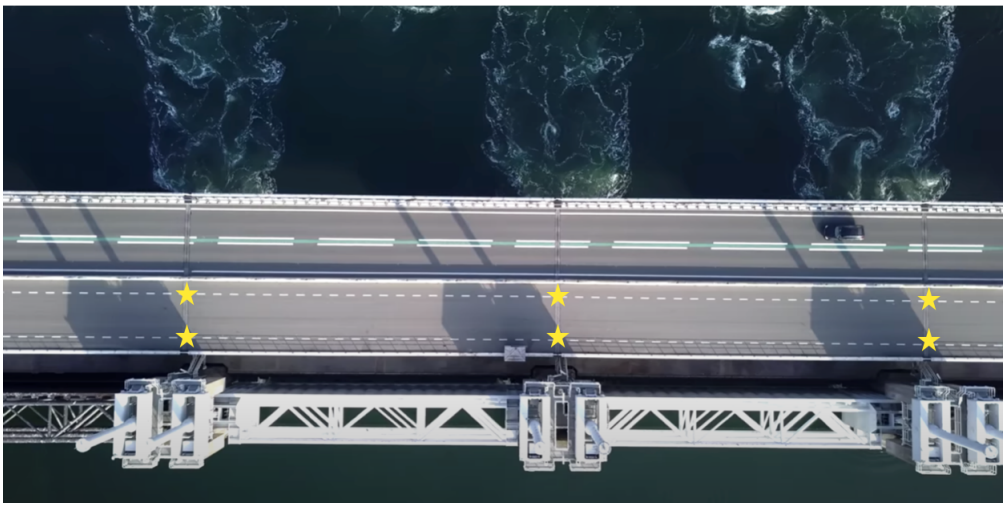

Figure A.6: Example of where GCPs were deployed. The contrasting road signs were well visible from large camera distances. Particular attention was given to a maximum spread in the x, y-plane.

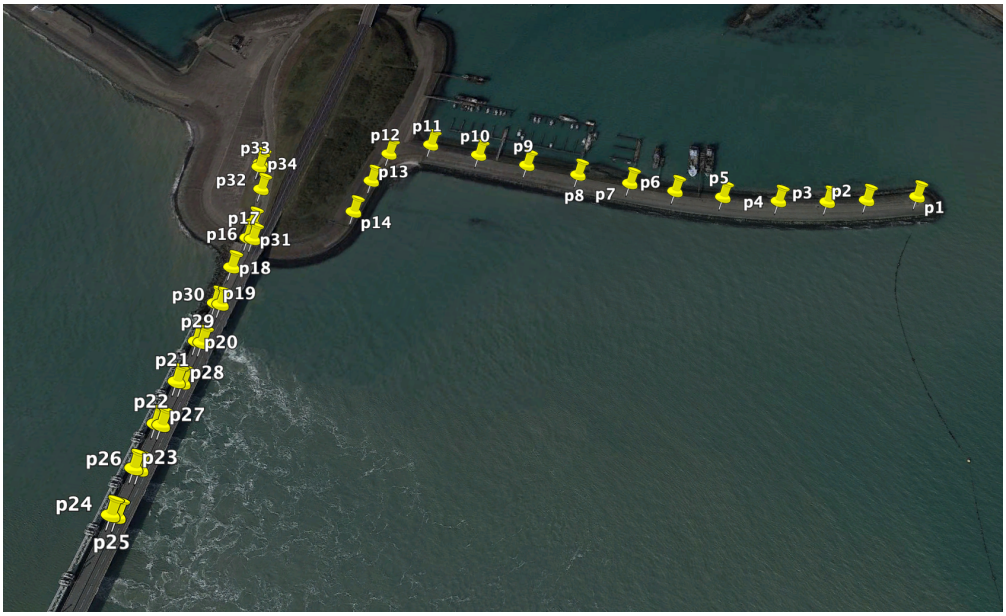

Figure A.7: Locations of ground control points around the Roompot inlet.

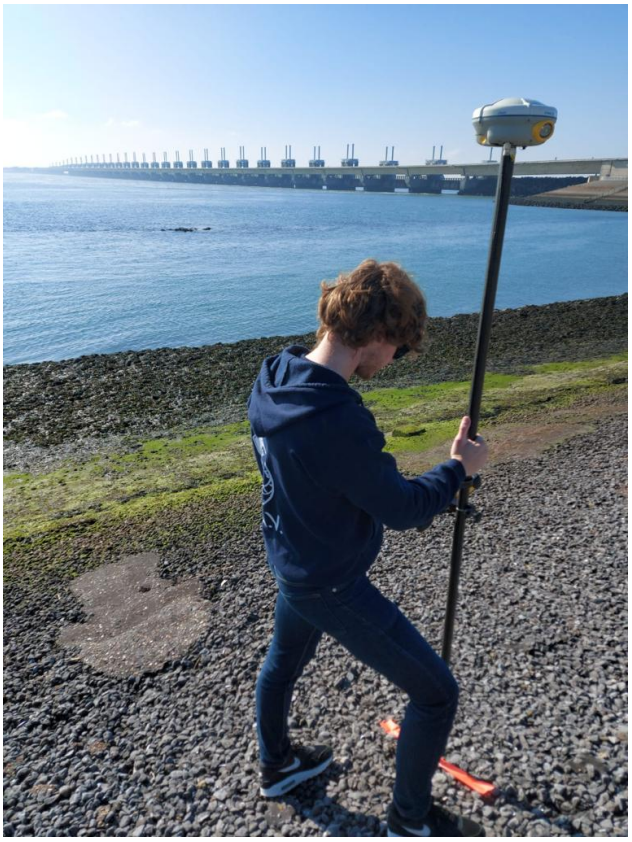

Figure A.8: Measurement of GCP 'P9' at the dam perpendicular to the barrier.

In total, 37 GCPs will be placed across the areas, of which their positions are accurately measured using a PPK survey from a Trimble R8 GNNS station. The post-processed results of all locations are shown in the ITRF2008 (Table 11) and ETRS86 (Table 12) reference systems, where *sn*, *se* and *su* are the standard deviations in latitudinal, longitudinal and vertical direction, respectively.

Table 11: PPK-processed coordinates in the ITRF2008 reference system.

	Lat[deg]	Lon[deg]	H[m]	sn[m]	se[m]	su[m]	sne[m]	snu[m]	seu[m]
p1	51.61647426	3.69353242	47.2319	0.0011	0.0008	0.0022	0.0003	-0.0008	-0.0007
p2	51.61635361	3.69280085	47.4038	0.0011	0.0008	0.0023	-0.0004	-0.0005	-0.0003
p3	51.61627278	3.69223351	47.2671	0.0012	0.0009	0.0023	-0.0003	-0.0006	-0.0004
p4	51.61620752	3.69152997	47.3193	0.0012	0.0010	0.0023	-0.0003	-0.0006	-0.0004
p5	51.61617319	3.69072435	47.3536	0.0012	0.0010	0.0023	-0.0002	-0.0007	-0.0005
p6	51.61617145	3.69002425	47.3206	0.0012	0.0011	0.0024	0.0005	-0.0007	-0.0009
p7	51.61619812	3.68935349	47.3904	0.0011	0.0009	0.0021	0.0002	-0.0004	-0.0003
p8	51.61622252	3.68857522	46.8564	0.0013	0.0010	0.0023	0.0005	-0.0005	-0.0003
p9	51.61626297	3.68779615	46.8873	0.0014	0.0010	0.0024	0.0005	-0.0003	-0.0004
p10	51.61631419	3.68704652	47.2286	0.0013	0.0010	0.0024	0.0005	-0.0006	-0.0003
p11	51.61636808	3.68629206	47.4643	0.0013	0.0010	0.0023	0.0003	-0.0007	-0.0006
p12	51.61618825	3.68570938	46.8135	0.0013	0.0009	0.0023	0.0004	-0.0008	-0.0005
p13	51.61583090	3.68556965	46.4821	0.0013	0.0010	0.0024	0.0004	-0.0009	-0.0006
p14	51.61544262	3.68545231	46.5030	0.0013	0.0010	0.0025	0.0004	-0.0009	-0.0005
p15	51.61647449	3.69353234	47.2111	0.0014	0.0009	0.0025	-0.0004	-0.0004	-0.0005
p16	51.61516076	3.68406793	57.9177	0.0016	0.0010	0.0026	-0.0003	-0.0010	0.0002
p17	51.61498957	3.68407797	57.6995	0.0013	0.0010	0.0025	-0.0005	-0.0008	-0.0005
p18	51.61465210	3.68400987	57.2988	0.0014	0.0011	0.0027	-0.0005	-0.0011	0.0007
p19	51.61425865	3.68397819	56.6459	0.0015	0.0010	0.0026	-0.0005	-0.0012	0.0007
p20	51.61385663	3.68392305	56.3654	0.0014	0.0011	0.0027	-0.0006	-0.0012	0.0009
p21	51.61345310	3.68386735	56.2582	0.0015	0.0011	0.0027	-0.0006	-0.0011	0.0009
p22	51.61305069	3.68381244	56.3193	0.0017	0.0016	0.0027	-0.0011	-0.0012	0.0010
p23	51.61264786	3.68375619	56.2758	0.0016	0.0012	0.0028	-0.0007	-0.0010	0.0009
p24	51.61224402	3.68370124	56.2571	0.0017	0.0015	0.0028	-0.0010	-0.0011	0.0011
p25	51.61223991	3.68377752	56.3831	0.0016	0.0011	0.0027	-0.0006	-0.0009	0.0009
p26	51.61264361	3.68383225	56.3588	0.0018	0.0012	0.0032	-0.0004	0.0005	0.0012
p27	51.61304630	3.68388836	56.3493	0.0016	0.0012	0.0030	-0.0003	-0.0006	0.0013
p28	51.61344908	3.68394295	56.3253	0.0016	0.0012	0.0029	-0.0002	-0.0005	0.0013
p29	51.61385228	3.68399817	56.3822	0.0016	0.0012	0.0030	-0.0003	-0.0007	0.0013
p30	51.61425428	3.68405339	56.7216	0.0015	0.0010	0.0024	0.0003	0.0005	0.0007
p31	51.61498564	3.68415345	57.7302	0.0017	0.0009	0.0026	0.0004	-0.0007	0.0006
p32	51.61556424	3.68400485	57.9923	0.0017	0.0009	0.0025	0.0004	-0.0007	0.0006
p33	51.61582637	3.68385042	57.5142	0.0019	0.0014	0.0035	-0.0008	-0.0014	0.0015
p34	51.61587157	3.68385025	57.5813	0.0019	0.0012	0.0027	0.0008	-0.0006	0.0007

Table 12: PPK-processed coordinates in the ETRS89 reference system.

	Lat[deg]	Lon[deg]	H[m]	sn[m]	se[m]	su[m]	sne[m]	snu[m]	seu[m]
p1	51.61646900	3.69352477	47.2095	0.0011	0.0008	0.0022	0.0003	-0.0008	-0.0007
p2	51.61634835	3.69279321	47.3815	0.0011	0.0008	0.0023	-0.0004	-0.0005	-0.0003
p3	51.61626752	3.69222587	47.2448	0.0012	0.0009	0.0023	-0.0003	-0.0006	-0.0004
p4	51.61620226	3.69152232	47.2970	0.0012	0.0010	0.0023	-0.0003	-0.0006	-0.0004
p5	51.61616793	3.69071670	47.3312	0.0012	0.0010	0.0023	-0.0002	-0.0007	-0.0005
p6	51.61616619	3.69001661	47.2982	0.0012	0.0011	0.0024	0.0005	-0.0007	-0.0009
p7	51.61619286	3.68934585	47.3681	0.0011	0.0009	0.0021	0.0002	-0.0004	-0.0003
p8	51.61621726	3.68856758	46.8340	0.0013	0.0010	0.0023	0.0005	-0.0005	-0.0003
p9	51.61625771	3.68778850	46.8649	0.0014	0.0010	0.0024	0.0005	-0.0003	-0.0004
p10	51.61630893	3.68703888	47.2063	0.0013	0.0010	0.0024	0.0005	-0.0006	-0.0003
p11	51.61636282	3.68628442	47.4420	0.0013	0.0010	0.0023	0.0003	-0.0007	-0.0006
p12	51.61618299	3.68570174	46.7911	0.0013	0.0009	0.0023	0.0004	-0.0008	-0.0005
p13	51.61582564	3.68556201	46.4598	0.0013	0.0010	0.0024	0.0004	-0.0009	-0.0006
p14	51.61543736	3.68544467	46.4807	0.0013	0.0010	0.0025	0.0004	-0.0009	-0.0005
p15	51.61646923	3.69352469	47.1888	0.0014	0.0009	0.0025	-0.0004	-0.0004	-0.0005
p16	51.61515550	3.68406029	57.8953	0.0016	0.0010	0.0026	-0.0003	-0.0010	0.0002
p17	51.61498431	3.68407032	57.6771	0.0013	0.0010	0.0025	-0.0005	-0.0008	-0.0005
p18	51.61464684	3.68400222	57.2765	0.0014	0.0011	0.0027	-0.0005	-0.0011	0.0007
p19	51.61425339	3.68397055	56.6236	0.0015	0.0010	0.0026	-0.0005	-0.0012	0.0007
p20	51.61385137	3.68391541	56.3430	0.0014	0.0011	0.0027	-0.0006	-0.0012	0.0009
p21	51.61344784	3.68385971	56.2358	0.0015	0.0011	0.0027	-0.0006	-0.0011	0.0009
p22	51.61304543	3.68380480	56.2970	0.0017	0.0016	0.0027	-0.0011	-0.0012	0.0010
p23	51.61264260	3.68374855	56.2534	0.0016	0.0012	0.0028	-0.0007	-0.0010	0.0009
p24	51.61223876	3.68369359	56.2347	0.0017	0.0015	0.0028	-0.0010	-0.0011	0.0011
p25	51.61223465	3.68376988	56.3608	0.0016	0.0011	0.0027	-0.0006	-0.0009	0.0009
p26	51.61263836	3.68382461	56.3364	0.0018	0.0012	0.0032	-0.0004	0.0005	0.0012
p27	51.61304104	3.68388072	56.3270	0.0016	0.0012	0.0030	-0.0003	-0.0006	0.0013
p28	51.61344382	3.68393531	56.3030	0.0016	0.0012	0.0029	-0.0002	-0.0005	0.0013
p29	51.61384702	3.68399053	56.3599	0.0016	0.0012	0.0030	-0.0003	-0.0007	0.0013
p30	51.61424902	3.68404575	56.6993	0.0015	0.0010	0.0024	0.0003	0.0005	0.0007
p31	51.61498038	3.68414581	57.7078	0.0017	0.0009	0.0026	0.0004	-0.0007	0.0006
p32	51.61555898	3.68399721	57.9700	0.0017	0.0009	0.0025	0.0004	-0.0007	0.0006
p33	51.61582111	3.68384277	57.4919	0.0019	0.0014	0.0035	-0.0008	-0.0014	0.0015
p34	51.61586631	3.68384261	57.5590	0.0019	0.0012	0.0027	0.0008	-0.0006	0.0007

A.5 Planning

Prior to the fieldwork campaign, an hourly planning was created and sent to all participants Table 13. Due to the unforeseen fog that hindered filming in the morning and early afternoon, activities were rescheduled throughout the day. Table 14 shows the actual times at which the measurements were carried out.

Table 13: Proposed overview of activities scheduled during the measuring campaign.

Time	**Activity**
9:30 - 10:00	Arrival and general meeting at ES-SSB
10:00 - 10:30	Measurement preparations
10:30 - 12:30	Drone measurements area 1
10:30 - 12:30	ADCP measurements area 1
12:30 - 13:00	Lunch break
13:00 - 15:00	Drone measurements area 2
13:00 - 15:00	ADCP measurements area 2
15:00 - 15:15	Coffee break
15:15 - 16:00	Additional drone flights (optional)
16:00 - 17:00	Wrap up and departure

Table 14: Overview of rescheduled activities adjusted throughout the measurement campaign.

Time	**Activity**
9:30 - 10:00	Arrival and general meeting at OSK
11:30 - 12:00	Test flights for visibility and camera orientation
12:00 - 14:30	ADCP measurements area 1
13:50 - 14:30	Drone measurements area 1
14:30 - 15:00	Lunch break
15:00 - 17:00	ADCP measurements area 2
13:00 - 17:00	Drone measurements area 2
17:00 - 17:30	Wrap up and departure

Appendix B: Theoretical behaviour of turbulent flows

B.1 Vorticity and the energy cascade

The motions of a fluid are governed by the Navier-Stokes equations. They generally describe a balance between the change in momentum of the fluid on one hand, and pressure gradients and dissipative viscous forces on the other. For the flow considered in this research, the set of equations is reduced to their incompressible form, i.e. the fluid's density remains constant during flow. Following Pope (2000), the Navier Stokes equations for incompressible flow can then be written as

$$\nabla \cdot \mathbf{u} = 0 \tag{B.1}$$

$$\rho \frac{\partial \mathbf{u}}{\partial t} + \rho(\mathbf{u} \cdot \nabla)\mathbf{u} = -\nabla P + \nu \nabla^2 \mathbf{u} = -\rho \mathbf{g}, \tag{B.2}$$

where $\mathbf{u}$=$(u, v, w)^T$ is the fluid velocity vector (in m/s), p is the hydrodynamic pressure (kg/ms^2), ρ is a constant density (kg/m^3), μ is the dynamic molecular viscosity (Ns/m^2) and $\mathbf{g}$ is the gravitational acceleration (m^2/s^2). Dividing Equation B.2 by the density and define the so-called non-hydrostatic normalized pressure by $p = \frac{P}{\rho} + g$, Equation B.2 can be rewritten into

$$\frac{\partial \mathbf{u}}{\partial t} + (\mathbf{u} \cdot \nabla)\mathbf{u} = -\nabla p + \nu \nabla^2 \mathbf{u}, \tag{B.3}$$

in which ν is the kinematic viscosity (m^2/s). Fluid motion is induced by hydrodynamic pressure gradients, while the velocity field is continuously deformed by the action of nonlinear momentum advection and viscosity. It was already stated that for Re $>$ 2000, flows can become hydrodynamically unstable and eventually exhibit chaotic behavior. The action of viscous forces (combined with no-slip boundary conditions) introduces rotation into the velocity field, even when the initial flow field did not contain vortices. Due to the presence of these rotations, a chaotic flow field will always contain vortices. The vorticity vector ζ (s^{-1}) is defined as

$$\zeta = \nabla \times \mathbf{u} \tag{B.4}$$

From Equation B.3, the vorticity equation can be written as (Kraichnan, 1967)

$$\frac{\partial \zeta}{\partial t} + \zeta(\nabla \cdot \mathbf{u}) = \mathbf{u}(\nabla \cdot \zeta) + \nu \nabla^2 \zeta. \tag{B.5}$$

Equation B.5 describes how the vorticity changes when moving along with a fluid element. The second term on the right-hand side is recognized as the diffusion of vorticity due to viscosity. The first term on the right can be expressed as

$$\mathbf{u}(\nabla \cdot \zeta) = \zeta s_{ij} \tag{B.6}$$

where

$$s_{ij} = \frac{1}{2}(\nabla_i u_j + \nabla_j u_i) \tag{B.7}$$

represents the *rate-of-strain* tensor. Dimensional indices are represented by: $i, j \in \{1, 2, 3\}$. Equation B.6 is often called *vortex stretching* and describes the interaction between the fluid deformation and the vorticity. Vorticity, and in particular vortex stretching, is a fundamental process in turbulence. If the velocity field is stretched in the direction of the local vorticity vector (i.e. normal to the associated vortex plane) the local vorticity in that direction will increase; rotational kinetic energy will be transferred to higher frequencies and hence to smaller scales, both in space and time Nieuwstadt et al. (2016). Because this process cannot occur in two dimensions, vortex stretching is restricted to 3D flows. At the macro scale, unstable larger eddies transfer energy to the eddies at smaller scales. This well known process of energy cascading continues until the energy is dissipated into heat by viscosity at the Kolmogorov scales. The break-down of vortices and dissipation of energy are therefore closely tied to the rotational nature of a turbulent flow. From Equation B.3 the energy equation can be formulated as follows (e.g. Frisch and Kolmogorov (1995); Tennekes and Lumley (2018):

$$\frac{\partial E}{\partial t} + \nabla \cdot [\mathbf{u}(p + E) + \nu\zeta \times \mathbf{u}] = -2\nu Z, \tag{B.8}$$

with $E = \frac{1}{2}\mathbf{u} \times \mathbf{u}$ being the energy and $Z = \frac{1}{2}\zeta \cdot \zeta$ the enstrophy. In the inviscid limit, i.e. $\nu \to 0$, the energy dissipation rate per unit mass ϵ ($\mathrm{m}^2/\mathrm{s}^3$) remains finite:

$$\epsilon = \lim_{\nu \to 0} 2\nu Z > 0, \tag{B.9}$$

In the limit, the Navier-Stokes equation conserves the kinetic energy, of which the forcing is balanced by energy dissipation. For this to hold, the enstrophy must grow as the viscosity decreases. This is consistent with the Kolmogorov spectrum, where the the spatial energy density spectrum E (m^3/s^2) at small isotropic turbulent scale is of the form (Frisch and Kolmogorov, 1995):

$$E(k) \sim \epsilon^{2/3} k^{-5/3}, \tag{B.10}$$

where k is the wave number (m^{-2}) associated with a certain turbulence length scale $\mathcal{L}$. The spectrum therefore does not depend on viscosity, but on the forcing and the wave number.

B.2 Implications for quasi 2D flows

Flows confined in the vertical direction exhibit very distinct properties in their vorticity dynamics, as the vorticity vector consists of only one component that is perpendicular to the 2D velocity field everywhere. Thus, vorticity reduces to a scalar field and the vortex stretching term in Equation B.5 disappears. This leads to the following revisited expression:

$$\frac{\partial \zeta}{\partial t} + \zeta(\nabla \cdot \mathbf{u}) = \nu \nabla^2 \zeta, \tag{B.11}$$

The remaining terms show that if no other vorticity inputs are present and if the vertical structure of the flow is more or less depth uniform, vorticity is a conserved quantity in 2D.

The Navier-Stokes equations in two dimensions have an infinite number of inviscid invariants, of which the energy and enstrophy (being conserved quantities) are the most important (Kraichnan, 1967). They are respectively expressed as

$$E_k = \frac{1}{2}\mathbf{u}^2 \int_0^\infty E(k)dk \tag{B.12}$$

$$Z = \frac{1}{2}\omega^2 = \int_0^\infty k^2 E(k)dk \tag{B.13}$$

The enstrophy Z can be expressed as the second moment of the spectral kinetic energy distribution (van Heijst, 2007). In the viscous case, i.e. $\nu > 0$, balance equations for the two quantities in spectral form are

$$\frac{\partial E}{\partial t} = -2\nu Z \quad , \quad \frac{\partial Z}{\partial t} = -\nu |\nabla \zeta|^2 \tag{B.14}$$

Since the enstrophy is bounded by its initial value, the energy dissipation rate will decrease in proportion to the viscosity; an energy cascade in the Kolmogorov sense will not occur. In the 2D case therefore:

$$\lim_{\nu \to 0} \frac{\partial E}{\partial t} = 0 \quad , \quad \lim_{\nu \to 0} \frac{\partial Z}{\partial t} < 0 \tag{B.15}$$

From Equation B.15 it can be concluded that a dissipation anomaly for the energy does not exists, and energy can not be dissipated at small scales. If in a 2D flow for a certain forcing with length scale $\mathcal{L}$ kinetic energy is added at a forcing wave number $k_f \sim \mathcal{L}^{-1}$, this energy may be redistributed by means of conservation of kinetic energy and enstrophy Talstra (2011). Figure B.1 illustrates the behaviour of the two processes. Kinetic energy transferred to smaller length scales (larger k) is then compensated by a flux towards the larger length scales (smaller k). (Kraichnan, 1967) expressed the two simultaneously occurring processes as:

$$E(k) \sim \begin{cases} \epsilon^{2/3} k^{-5/3} & \text{if } k < k_i \quad (\text{“inverse energy cascade”}) \\ \eta^{2/3} k^{-3} & \text{if } k > k_i \quad (\text{“enstrophy cascade”}) \end{cases} \tag{B.16}$$

where η (s^{-3}) is the rate of enstrophy dissipation per unit mass. The two processes are illustrated in Figure B.1.

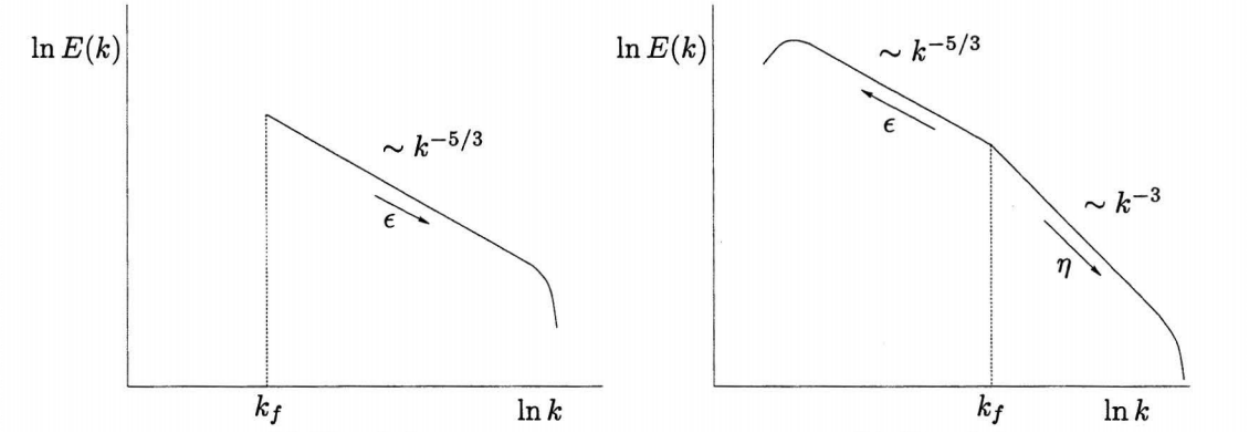

Figure B.1: Schematical illustration of (a) the direct energy cascade in 3D turbulence and (b) the inverse energy cascade and the direct enstrophy cascade in 2D turbulence.

Due to the inverse energy cascade kinetic energy tends to concentrate in large-scale vortices that are stable and do not break up, a process often referred to as "self- organization" (van Heijst, 2007). A unique property of the inverse energy cascade is that adjacent 2D vortices may merge into larger eddies when they exhibit the same vorticity sign. For opposite signs the vortices are able to co-exist.

Appendix C: Image calibration

This appendix describes a series of approaches for calibrating the camera images and includes an error analysis of the different results. It starts with an explanation on how the projection matrix can be solved using the full camera matrix, and what assumptions were made to compute the homography between images instead. It will then elaborate on the choices made to add or exclude certain ground control points (GCPs) that may significantly affect the calibration process. To this end, multiple configurations of the GCPs are tested to quantify pixel displacements not attributed to the flow of water within the domain of interest.

C.1 Camera projection

In Section 3.2.4 the projection matrix was expressed as

$$sx_i = K\begin{bmatrix} R \mid t \end{bmatrix} X_i = \begin{bmatrix} f_u & 0 & 0 \\ 0 & f_v & 0 \\ u_0 & v_0 & 1 \end{bmatrix} \begin{bmatrix} R_{11} & R_12 & R_13 & t_1 \\ R_{21} & R_22 & R_23 & t_2 \\ R_{21} & R_22 & R_23 & t_1 \end{bmatrix} \begin{bmatrix} X \\ Y \\ Z \\ 1 \end{bmatrix}, \tag{C.1}$$

with K the matrix containing the intrinsic camera parameters. R is a 3x3 rotation matrix and t a 3x1 translation vector, both of which make up the extrinsic matrix. The camera extrinsics can be solved via a pose estimation using PnP. For the Roompot application however, GCPs required for this estimation were not sufficiently distributed, leading to projection biases and hence (very) inaccurate projection matrices. Rather than solving for the full camera matrix, a technique called homography can be used to find the locations of points from an image. That is, a geometric transformation matrix is applied to map points from the image that are on the plane to their world coordinates. Because of the 2D nature of this projective transformation, all $Z-$coordinates are assumed to be on the same plane with $Z =$ is zero. The GCPs at the Roompot inlet are positioned at an average elevation of about 10 m above the water surface. Although computing the homography may therefore introduce (small) projection errors, this approach is easy to implement even with relatively poor GCP distribution. If no translations of the camera over the record duration are assumed, Equation C.1 can be rewritten to

$$sx_i = K\begin{bmatrix} R \mid 0 \end{bmatrix} \begin{bmatrix} X \\ Y \\ 0 \\ 1 \end{bmatrix} = KRX_i. \tag{C.2}$$

Therefore, $x_i = KRK^{-1}X$, where KRK is the homography. The equation can be rewritten to

$$s\begin{bmatrix} x \\ y \\ 1 \end{bmatrix} = \begin{bmatrix} h_{11} & h_{12} & h_{13} \\ h_{21} & h_{22} & h_{23} \\ h_{31} & h_{32} & h_{33} \end{bmatrix} \begin{bmatrix} X \\ Y \\ 1 \end{bmatrix} \tag{C.3}$$

The intrinsic parameters were determined during lab experiments, but information on R is missing. The 9 unknown elements of the homography matrix can be estimated using a linear least squares method. The inverse homography can be used to map an image into the same perspective as the target.

C.2 Linear transformation

An alternative solution to transform between image and world coordinates is derived in terms of the following collinearity equations (Holland et al., 1997):

$$\begin{aligned} u &= \frac{a_0 + a_1 x + a_2 y + a_3 z}{1 + a_4 x + a_5 y + a_6 z} \\ v &= \frac{a_7 + a_8 x + a_9 y + a_{10} z}{1 + a_4 x + a_5 y + a_6 z}. \end{aligned} \tag{C.4}$$

The unknown coefficients $a_0 ... a_{10}$ are known as the direct linear transformation (DLT) coefficients, and are composed of the three rotation angles, the camera center world coordinates, and the image center coordinates. Instead of the intrinsic matrix K, the three remaining unknowns are the effective focal length, and two scale factors. Rewriting Equation C.4 leads to

$$\begin{aligned} u &= a_0 + a_1 x + a_2 y + a_3 z - b_1 u x - b_2 u y - b_3 u z \\ v &= c_0 + c_1 x + c_2 y + c_3 z - b_1 v x - b_2 v y - b_3 v z. \end{aligned} \tag{C.5}$$

These equations can be solved for using the linear least squares relation $y = Ax$, with y the vector that includes the pixel coordinates (u,v) of each ground control point. A is mxn design matrix with m the number of GCPs, and n the amount of unknown parameters. They can be expressed as follows:

$$y = \begin{bmatrix} u_1 \\ v_1 \\ \vdots \\ u_k \\ v_k \end{bmatrix}, \quad A = \begin{bmatrix} 1 & x_1 & y_1 & z_1 & -u_1 x_1 & -u_1 y_1 & -u_1 z_1 & 0 & 0 & 0 & 0 \\ 0 & 0 & 0 & 0 & -v_1 x_1 & -v_1 y_1 & -v_1 z_1 & 1 & x_1 & y_1 & z_1 \\ \vdots & \vdots & \vdots & \vdots & \vdots & \vdots & \vdots & \vdots & \vdots & \vdots & \vdots \\ 1 & x_k & y_k & z_k & -u_k x_k & -u_k y_k & -u_k z_k & 0 & 0 & 0 & 0 \\ 0 & 0 & 0 & 0 & -v_k x_k & -v_k y_k & -v_k z_k & 1 & x_k & y_k & z_k \end{bmatrix} \tag{C.6}$$

The vector of unknowns can then be computed via

$$\hat{x} = (A^T Q_y^{-1} A)^{-1} A^T Q_y^{-1}, \tag{C.7}$$

with Q_y being the covariance matrix of the observations. The least squares residuals are

$$\hat{e} = y - A\hat{x} \tag{C.8}$$

With the estimated coefficients, the inverse equations

$$\begin{bmatrix} [a_0 - c_1 u] & [a_1 - c_2 u] & [a_2 - c_3 u] \\ [b_1 - c_1 v] & [b_2 - c_2 v] & [b_3 - c_3 v] \end{bmatrix} \begin{bmatrix} x \\ y \\ z \end{bmatrix} = \begin{bmatrix} [u - a_3] \\ [v - c_0] \end{bmatrix} \tag{C.9}$$

can now be determined with only the new world coordinates x,y, and z as unknowns. Assuming the GCPs to be positioned at an equal elevation, and the slope of the water surface to be negligible, z can be taken as a constant value defined by the difference between the water surface and each GCP. Equation C.10 can subsequently be written as

$$\begin{bmatrix} [a_1 - b_1 u] & [a_2 - b_2 u] \\ [c_1 - b_1 v] & [c_2 - b_2 v] \end{bmatrix} \begin{bmatrix} x \\ y \end{bmatrix} = \begin{bmatrix} [u - a_0 - (a_3 - b_3 u)z] \\ [v - c_0 - (c_3 - b_3 v)z], \end{bmatrix} \tag{C.10}$$

from which the world coordinates x and y can be computed.

Appendix D: RSIV related studies

RSIV showed to be a powerful technique capable of analyzing the velocity field distribution of the surface flow with high precision. The main advantage of RSIV over in-situ measurements is that it instantaneously measures velocities in a flow plane, rather than at a point or along a line. The mean vector field, turbulence characteristics, flow patterns (streamlines, pathlines), vorticity, and discharges can all be readily obtained from the raw image-based measured velocities (Muste et al., 2008). While the above examples are not exhaustive, they are intended to illustrate that RSIV is a cost-effective, quick and safe tool to provide comprehensive, quantitative flow information over a wide range of flow types (uniform, non-uniform) and measurement conditions (e.g., floods, low, shallow flows) with little site preparation. As was explained in this thesis, the principles of RSIV are based on the procedure of conventional PIV method that is discussed in detail by e.g. Meinhart et al. (1999). The use of mobile filming allows for flow field estimations on much larger scales. In recent research, the extension from conventional PIV to free-surface velocity measurements, commonly called large-scale particle image velocimetry (LSPIV), was already studied with great success (Weitbrecht et al., 2002; Fujita et al., 1998; Johnson and Cowen, 2017). LSPIV is usually carried out with a stationary camera mounted on a platform to limit the effect of vibrations and geometric distortion. In more recent studies, images were also taken from mobile platforms such as UAVs (Koutalakis et al., 2019; Tauro et al., 2016), and even helicopters (Detert and Weitbrecht, 2014). These studies motivated the current research to extent the applicability to even larges surface areas.

In hydraulic engineering applications, LSPIV has so far been tested to measure surface velocity vectors of water and ice in a variety of flows (Ettema et al., 1997; Fujita et al., 1998; Uijttewaal et al., 2001). While the image and data processing algorithms are similar to those used in conventional PIV, adjustments are required for processing the recorded images. Similar to RSIV, in LSPIV the water surface is often seeded with tracer particles that advect with the flow and provide visual texture in the images. Natural tracers such as bubbles, debris, ripples or water color gradients visible at the flow's surface have been successfully tracked (Le Coz et al., 2010; Fujita and Kunita, 2011; Muste et al., 2014). Good agreement between LSPIV measurements and other methods confirmed that these natural tracers are sufficiently light to follow the mean surface flow Ettema et al. (1997); Jasek et al. (2001).

Many advances in image quality and post-processing techniques have been made since the advent of remotely measuring surface characteristics of environmental flows in the mid 1990s (Muste et al., 2008). With high-resolution cameras nowadays easily obtainable, water surfaces can be imaged with great detail at low costs. Many studies demonstrated that the LSPIV accuracy is within 3.5–5% in laboratory conditions and ranging from 5% to 15% depending of the site and condition at the time of the measurements (Muste et al., 2014). Examples of successful LSPIV application are found in storm water detention basins Zhu and Lipeme Kouyi (2019), river discharge measurements (Hauet et al., 2008; Jin and Liao, 2019; Le Coz et al., 2010), and estimation of river ice velocities (Daigle et al., 2013).

Appendix E: Additional RSIV results

The data analysis that was shared in Chapter 4 included only the most significant results derived from RSIV. This appendix covers supplementary results related to the sensitivity analysis and projections in Area B that are believed to add to the quality of the RSIV procedure. To this end, Section E.1 starts with additional results derived from the application of several pretreatment methods introduced in Chapter 4.2. In Section E.2, an analysis on the limitations of the projection analysis over Area B are presented.

E.1 Pretreatment methods

From the sensitivity analysis important conclusions were drawn with respect to the duration of filming, amount of frames per seconds, and *IA* options. It was found that various pretreatment methods for the particular application did not lead to improved results, a statement that is being demonstrated in this section.

Highpass filter

A highpass filter can be applied in case low frequency noise such as inhomogeneous lightning or low seeding density cause noise on the images. High frequency information passes through the filter, and low frequency noise is subtracted from the image. Figure E.1 shows the highpass filter for two different sizes: 60x60 px and 90x90 px. Results are very similar, indicating that highpass filtering for the current application does not contribute to an improved velocity field.

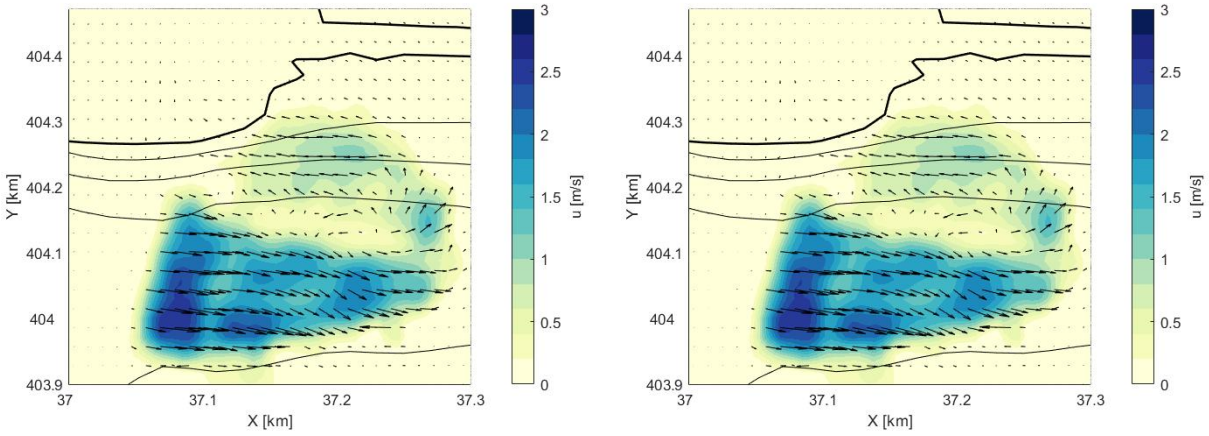

Figure E.1: Applied high pass filters of size 60x60 px (left image) and 90x90 px (right image)

.

Wiener filter

A Wiener filter is another method to filter out noise from an image. In contrast to a frequency response filter such as a highpass, signal and noise in a Wiener filter are stationary linear stochastic processes with

known spectral characteristics. More information can be found in e.g. Brown and Hwang (2012). Figure E.2 illustrates the effect of Wiener filtering for sizes 60x60 px, 90x90 px, 120x120 px, and 150x150 px. Compared to Figure 4.14a, computed velocities corresponding to surface ripples are to some extent filtered out. No large variations are found in the main flow, nor are they present between each different filter size. Therefore, a Wiener filter may be useful for RSIV applications where surface roughness cause vectors not related to the area of interest are computed (such as the one considered here). It would however depend on the SNR of the specific flow, i.e. the filter may perform worse if tracked seeding particles are dominated by surface roughness.

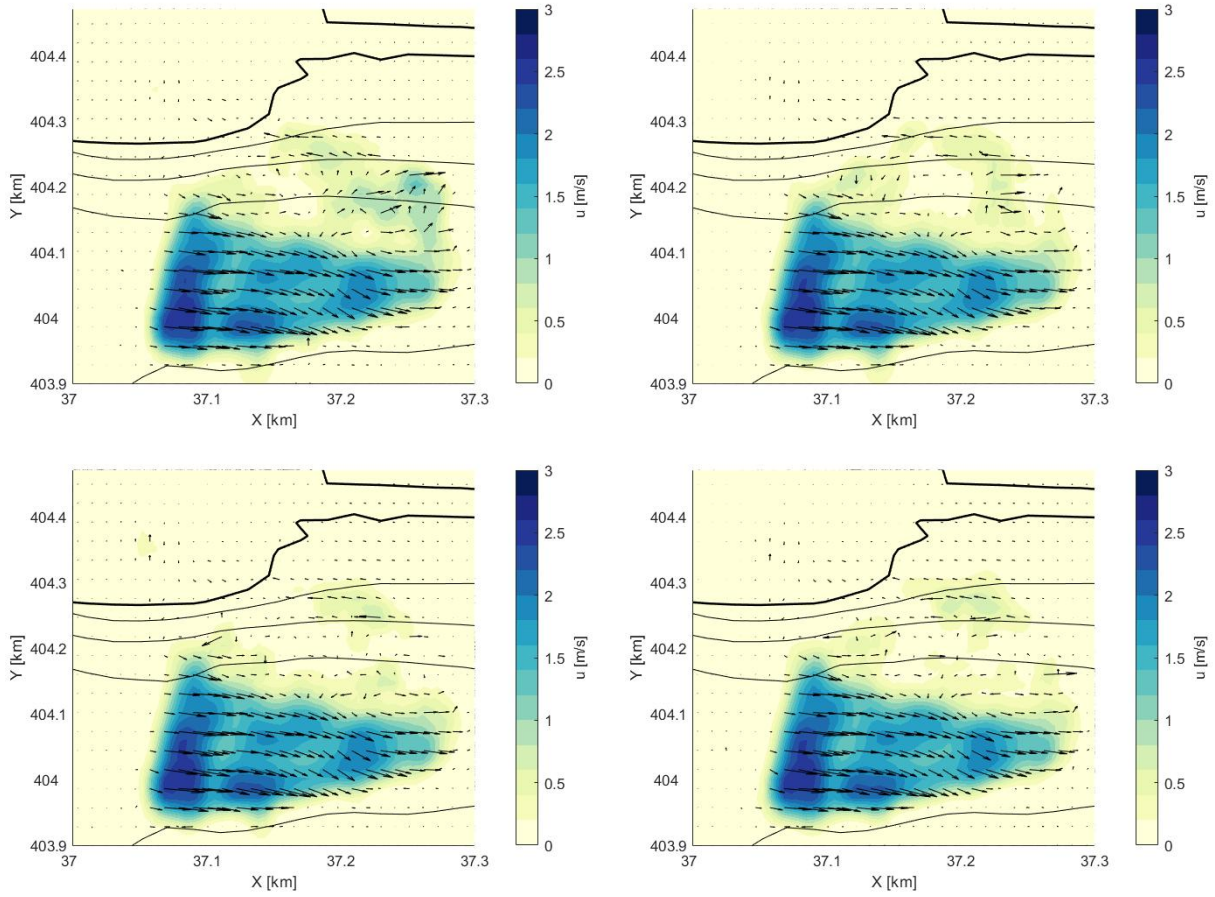

Figure E.2: Applied Wiener filters for different sizes. From upper right to lower left image: 60x60 px, 90x90 px, 120x120 px, and 150x150 px.

.

Intensity capping and window deformation options

In Section 3.2.5 the process of image enhancing was explained. The purpose of creating larger lightning contrast between relevant tracers following the main flow the environment is to better autocorrelate surface features between image pairs. Non-uniformities in lightning caused by e.g. solar glare or shadows on the water surface may bias the result of the correlation signal. Shavit et al. (2007). Intensity capping can be applied to limit the upper values of the greyscale intensity so that only a small amount of the information

on pixel intensity is adjusted. In Figure E.3 the upper limits are adjusted to account only for 0.6 and 0.8 times the maximum intensity. No changes to the flow field however are apparent.

Finally, a *spline* window deformation is applied as opposed to a linear approach. The window deformation technique interpolates displacement information between successive passes. Thielicke and Stamhuis (2014) mention a (small) improvement when using *linear* over *spline* window deformation, though the latter is computationally more expensive. No differences between the two flow fields are again observed (Figure E.4).

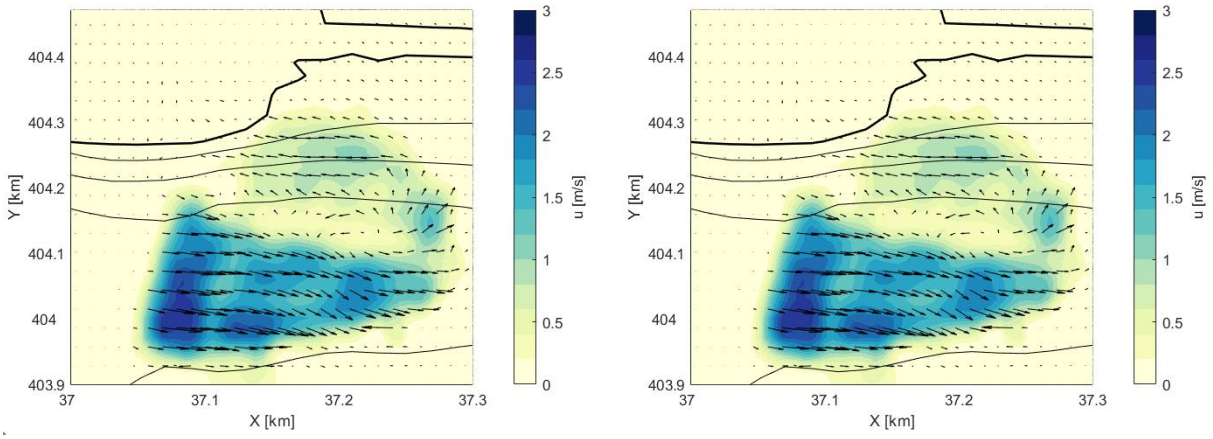

Figure E.3: Flow fields using an intensity of 0.6 (left) and 0.8 (right) times the maximum intensity of the greyscale image.

.

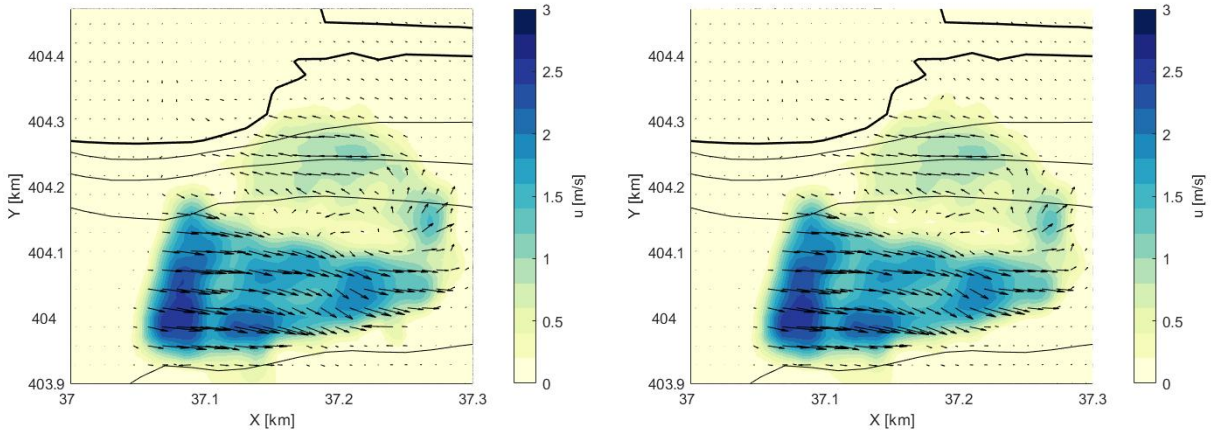

Figure E.4: Flow fields using a *linear* (left) and *spline* (right) window deformation technique.

E.2 Projection analysis Area B

RSIV analyses were carried out over Area A (close to the barrier) because the flow is characterized by a high seeding density. The lack of tracers in Area B was a challenge well known, but attempts were nonetheless made to assess the possibility of tracking small agglomerations of boils or foam separated from the main flow. Another option was to use the (raw) images to estimate the size of the recirculation zone based on a sediment

plume. Similar to Area A, this would require a sufficiently estimated projection. Markers were places on a dam along the left margin of the images, but any information in perpendicular direction was missing. Solving for the projection matrix using the inverse homography was not possible because all markers were collinear (i.e. they were placed on the same line). One method that was applied to account for this lack of GCPs involved an estimation of the coordinates of the safety line that would act as 'imaginary' markers. The distances between GCPs and several buoys placed along this safety line were measured using Google Earth with an accuracy in the order of several tens of meters. Although this provided some spatial information regarding the upper part of the image, another imaginary GCP was required to also account for the lower part of the image. Since any reference for such a marker position was absent, only very rough guesses could be made. Also, since the FoV of the camera reached all the way across the estuary, these guesses would only add information close the dam. An example of a projection is shown in Figure E.5. The stretched projection is clearly apparent. An analysis similar to that described in Section 4.2.1 was carried out to estimate the quality of the projection errors. Projection errors quickly increased for increasing distances from the camera at the right margin of the images. No configuration using imaginary GCPs contributed to a representative projection, therefore the RSIV procedure in Area B was not further elaborated on.

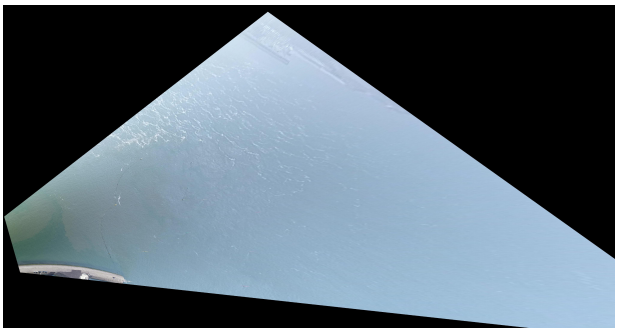

Figure E.5: Attempted camera projection for Area B. The lack of any spatial information on the water and the large FoV lead to large projection errors.

.

Appendix F: Numerical validation of experimental set-up

A three-dimensional representation of the flow field is imperative if the observed 2D velocity vectors are to be related to near-bed turbulence intensities. Since analytical solutions to describe turbulent flows are lacking, numerical simulations are required to solve the Navier-Stokes equations down to the Kolmogorov length scales in a numerical grid. Chapter 2 covered the principles of flow attachment and flow separation for laterally (non)uniform flows occurring near the Roompot scour hole. Broekema (2020) performed a series of laboratory experiments to describe the flow patterns for these two different regimes in a flume, the cases of which are being validated through a numerical model in this chapter. Section F.1 describes the experimental set-up used by the author. In Section F.2, the model characteristics and chosen parameters are elaborated on. The model results are then the topic of Section F.3.

F.1 Experimental set-up

The experimental cases were performed in a 14 m long, 0.4 m deep and 0.4 m wide glass-sided flume (Figure F.1). Its main features are a horizontal obstruction and a sloping bottom at a certain distance from the flume's inlet. The lateral velocity gradients in a developing mixing layer downstream of the obstruction diminishes as the mixing layer grows in size (see Equation 2.2). The nonuniformity of the flow can consequently be controlled by the distance L_D between the obstruction and the upstream slope. The gradient of the slope was chosen such that flow separation would be induced for horizontally uniform configurations. The bed level in the flume was uniform in lateral direction. The upstream and downstream water levels d_u and d_d equalled approximately 0.12 m and 0.27 m, respectively. These values resemble the relative increase in flow depth over the Roompot scour hole. To ensure a fully turbulent flow with minimum surface disturbances, a Reynolds number of $Re = 3{\cdot}10^4$ was generated using a discharge value Q_{in} of 11 l/s. Table 15 shows an overview of the two cases considered.

Table 15: Overview of the two different experimental cases performed by Broekema (2020).

Case	Slope	d_u[m]	d_d[m]	L_d [m]	Q_{in} [l/s]	Vertical flow state
Case I	1:2 (26.5 °)	0.12	0.27	0.4	11	Attachment
Case II	1:2 (26.5 °)	0.12	0.27	0.7	11	Separation

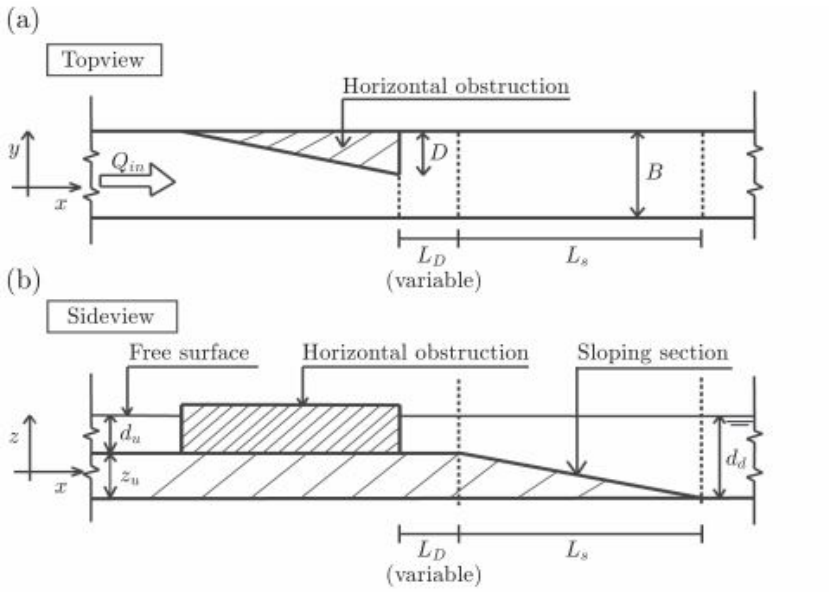

Figure F.1: Sketch of the experimental configuration. a) Topview of the experimental set-up. The flume width B is 0.4 m, and the horizontal contraction has a maximum width D of $0.5B$. The distance L_D is an experimental variable to control the magnitude of the lateral velocity gradient at the slope. The length of the sloping section L_s is determined by the slope steepness i_b. b) Side-view of the set-up. The water depth upstream of the slope is given by $d_u = 0.12$ m, and the water depth downstream of the slope equals $d_d = 0.27$ m (Broekema (2020)).

.

F.2 Model set-up

The field of computational fluid dynamics (CFD) is concerned with numerical solution of differential equations governing transport of mass, momentum, and energy in moving fluids. CFD activity emerged and gained prominence with availability of computers in the early 1960s (Date, 2005). Since then, many software packages and computer codes were developed, after which CFD became an important component of engineering practise in a wide variety of industries. In this thesis the package OpenFOAM is used. Although OpenFOAM has a very wide range of (industrial) applications, it is often the desired choice in research work on e.g. scour hole development and hydrodynamic processes (Baykal et al., 2015; Kim et al., 2014; Liu and García, 2008).

F.2.1 Turbulence model

Flow separation is a very complex phenomenon and requires high resolution numerical modeling to be captured. However, resolving the Navier-Stokes equations on all scales for the domain considered is computationally too expensive. Another approach would be to ensemble average these equations, losing information on time dependent fluctuations but allowing the use of a much coarser numerical grid. These Reynolds-averaged Navier-Stokes (RANS) solutions introduce Reynolds stresses that need to be closed using a turbulence closure model. Simulation flow separation would nonetheless require a high resolution grid, and solving for the multiple equations in commonly used RANS models (e.g. $k-\epsilon$ or $k-\omega$) is still computationally demanding. Also, studies on flow separation have shown that current steady RANS methods are often not within the

reach of simulating the relevant flow phenomena (Spalart, 2000; Rodi, 1997). The application of a large eddy simulation (LES) on the domain is therefore the desired choice, even though an even smaller time step and finer grid is required. Appendix B briefly summarizes the most widely adopted models and provides support for the model chosen.

LES can be regarded as a simulation technique intermediate between the direct simulation of turbulent flows and the solution of the Reynolds-averaged equations. In LES the contribution of the large, energy-carrying structures to momentum and energy transfer are resolved, and only the effect of the smallest scales of turbulence is modeled (Figure F.2). This allows for large-scale unsteadiness of the flow to be simulated in great detail, including flow separation and vortex shredding (Pope, 2000). Because the eddies become more isotropic as they cascade down to the Kolmogorov scales, they lose their energy in a self-similar processes not much affected by the large scale geometry (Uijttewaal, 2002). Modelling the small scales in the inertial subrange greatly enhances numerical speed while loss of information is limited. The small scale motions are removed by spatial averaging or filtering, the result of which is similar to the Reynolds equation:

$$\frac{\partial}{\partial t}(\bar{u_j}) + \nabla_i(\bar{u_j}\bar{u_i}) = -\frac{1}{\rho}\nabla_j\bar{p} + \nu\nabla_i^2\bar{u_j} + \nabla_i\tau_{ij}. \tag{F.1}$$

τ_{ij} represents the stresses caused by the processes on scales smaller than that of the spatial filter. This so called 'sub-grid stress' can be formulated as:

$$\tau_{ij} = \nu_t(\frac{\partial\bar{u_i}}{\partial x_j} + \frac{\partial\bar{u_j}}{\partial x_i}). \tag{F.2}$$

Viscous terms have been neglected, and incompressible continuity has been assumed for the grid-filtered variables (Lilly, 1992). These stresses require the subgrid-scale to be modelled. The homogeneity and isotropy of the sub-grid turbulence allows to define the a sub-grid viscosity defined by the length scale of the filter width (mesh size) and the sub-grid deformation. In the commonly used Smagorinsky's model, the eddy-viscosity is assumed to be proportional to the subgrid characteristic length scale Δ and to a characteristic turbulent velocity taken as the local strain rate

$$\nu_t = (C_s\Delta_f)^2\sqrt{(2S_{ij}S_{ij}} \quad , \quad S_{ij} = \frac{1}{2}(\frac{\partial\bar{u_i}}{\partial x_j} + \frac{\partial\bar{u_j}}{\partial x_i}), \tag{F.3}$$

where Δ_f is the filter width and C_s the Smagorinsky constant. This method assumes that the energy production and dissipation of the small scales are in equilibrium.

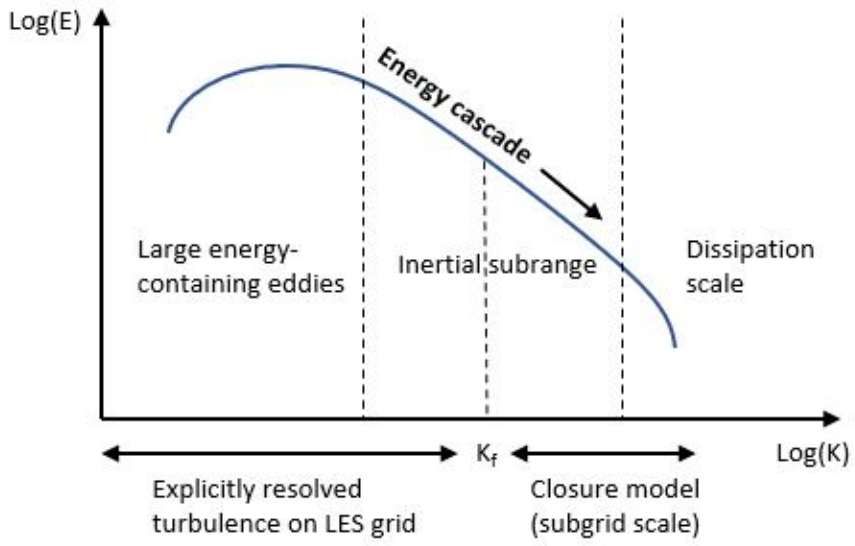

Figure F.2: Schematic representation of the LES approach: large energy-containing eddies are resolved while the smaller scales are modelled using a subgrid model

.

Following Lilly (1992), the constant C_s may be obtained by assuming that the cut-off wave number $k_c = \frac{\pi}{\Delta}$ lies within a $k^{-5/3}$ Kolmogorov cascade for the energy spectrum $E(k) = C_k \epsilon^{2/3} k^{-5/3}$ (see Section F.2.1) and requiring that the ensemble-averaged subgrid dissipation is identical to ϵ. An approximate value for the constant is then

$$C_s = \frac{1}{\pi}(\frac{3C_k}{2})^{-3/4}. \tag{F.4}$$

For a Kolmogorov constant of $C_K \approx 1.4$, this yields $C_s \approx 0.18$.

This value is close to the chosen default setting of OpenFOAM, where C_s is taken as 0.156. However, C_s appears to require adjustment for different problems, which diminishes the transferability and predictive ability of the LES model.

F.2.2 Boundary layers and wall treatment

Because $y^+ \gg 1$ in the entire domain, wall functions are applied to properly model the turbulent viscosity ν_t close to the walls. Wall functions are boundary conditions and in OpenFOAM all of them are included in the abstract class `FvPatchField`. They provide Dirichlet and Neumann boundary conditions, which inherit from `FixedValue` and `zeroGradient`, respectively. Wall functions cover the effect of surfaces if they are not modeled directly, and are therefore only avoidable at DNS resolution close to the wall. Here only the application of wall functions in OpenFOAM is described. In `wallFunctions` directory there are six types of wall function sub-directories. For the LES model considered, only `nutWallFunctions` can be applied, which is an abstract class in the *nutWallFunctions* directory and inherits from the `fixedValueFvPatchScalarField`. From this class the `nutUBlendedWallFunction` is applied. It provides a wall constraint on the turbulent viscosity, i.e. ν_t, based on velocity. It uses a binomial-function and a wall-function blending method between

the viscous and inertial sublayer predictions of ν_t via:

$$\nu_t = (u_{\tau,v}^n + u_{\tau,l}^n)^{1/n}, \tag{F.5}$$

where u_τ is the friction velocity, $u_{\tau,v}$ the friction velocity in the viscous sublayer and $u_{\tau,l}$ the friction velocity in the inertial sublayer. n is a blending factor.

The simplest approach to include wall modeling in LES simulation imposes some additional constraints upon the eddy viscosity. The Smagorinsky model predicts that the eddy viscosity reaches its highest values in regions of intense shear, for example, near solid boundaries. However, observations show that turbulent eddies are damped near wall boundaries. Therefore, a damping mechanism needs to be added to the Smagorinsky model to capture the true behavior of eddies near a wall. Typically, a damping function of the type suggested by Van Driest (1956) may be employed, which leads to the following expression for the eddy viscosity:

$$D = 1 - exp^{\frac{y^+}{A^+}}, \tag{F.6}$$

in which $A^+ = 26$ is a Van Driest constant. The constant scaling is chosen to ensure that the Smagorinsky model produces a mean velocity profile that agrees well with that computed from the law of the wall for simple shear flows. The final length scale is given by:

$$\Delta = min(\frac{ky}{C_s}D, \Delta_g), \tag{F.7}$$

where Δ_g is a geometric-based delta function. Here the cube-root volume delta is used.

F.2.3 Numerical grid

In Section 5.3.1 it was mentioned that for complex flow phenomena such as flow separation high resolution modelling is required. The solubility of the flow field (i.e. low residuals and convergence of the included parameters) is to a large extent affected by the mesh dimensions. The size of the mesh should be sufficiently small to be in the inertial zone of the energy spectrum, ensuring it's smaller than the large scale phenomena but larger than the smaller scales that would be filtered by the model. On the other hand, the mesh size is chosen such that the maximum Courant number (Co) in each cell is kept below one. The dimensionless wall coordinate y^+ has a value well above the viscous sublayer for all boundaries so that wall functions are necessary. Finally, aspect ratios close to one may considerably increase the convergence rate of the solution. Also, for studying flow separation gradients along the surface can be significant. Large cell aspect ratios are undesirable as they can lack tangential resolution to capture those gradients, and therefore lead to inaccurate results around the location of a separation point.

To limit the computational time during the set-up of the simulations, the model parameters were adjusted such that it initially would properly solve the flow field for a relatively course grid. Eventually a balance between resolution and simulation time was established for a high resolution grid.

F.2.4 Boundary and initial conditions

In addition to the boundary conditions specified for the turbulent viscosity, the LES model requires conditions for velocity and pressure to be defined across the domain. At all boundaries but the outlet, the pressure

is set to `zeroGradient` such that there is no gradient in the variable. For the velocity a `noSlip` boundary condition is chosen at the side walls and the bottom wall (bed). Velocities at the free surface are modelled using a `slip` condition, resulting in a wall shear stress equal to 0 N/m^2.

In unsteady simulations such as LES the challenge is particularly pronounced at the inflow boundary of spatially developing turbulence simulations (Di Mare et al., 2006; Wu, 2017). Ideally, some or all of the following boundary conditions should be met:

- be stochastically varying on scales down to the filter scale (spatially and temporally);
- behave like turbulence;
- allow the easy specification of turbulent properties (such as turbulence intensities and its length scales);
- be easy to implement and to adjust to new inlet conditions.

The lack of initial perturbations entering the domain inevitably demands for some artificial turbulence generated at the inlet. Many attempts to achieve such a turbulence state at the start of the simulation have been made, some of which are implemented in the source code of OpenFOAM. The intuitively most straightforward choice is the generation of some random velocity fluctuations. This white noise however is spatially and temporally uncorrelated and turbulence properties tend to die out quickly (Tabor and Baba-Ahmadi, 2010). A more sophisticated and accurate solution to the problem is to use turbulence properties generated in a RANS model as initial conditions at the inlet. The option `turbulentDFSEMInlet` includes the development of synthesised eddies based on input values for the Reynold stresses and turbulent length scales (Poletto et al., 2013). To this end, Reynold stresses and velocities are extracted from a $k-\omega$ simulation. The turbulence length scales were computed according to the following definition:

$$L = C_{\mu}^{-1/4} \frac{\sqrt{k}}{\omega}, \tag{F.8}$$

where C_{μ} is a model constant with a value of 0.09. An overview of the specified boundary and initial conditions is provided in Table 16.

Table 16: Boundary and initial conditions as specified in OpenFOAM.

Boundary	U $[m/s]$	p $[m^2/s^2]$	ν $[m^2/s]$
Inlet	turbulentDFSEMInlet	zeroGradient	Calculated
Outlet	zeroGradient	0	Calculated
Free surface	slip	zeroGradient	nutUBlendedWallFunction
Side walls	noSlip	zeroGradient	nutUBlendedWallFunction
Bottom wall	noSlip	zeroGradient	nutUBlendedWallFunction

F.2.5 Discretization

Choices for spatial and temporal discretizations are based on the trade-off between accuracy and stability of the numerical models. Time discretization is applied using a second order implicit backward scheme suitable for transient simulations. The time-step was chosen small enough to maintain a Courant number < 0.5. Unlike its temporal equivalent, spatial discretization can be divided into different subcategories, the

most important ones being the gradient schemes and divergence schemes. For the former, the default `Gauss linear` option is chosen in which the standard finite volume method is applied. Interpolation is performed by central differencing. The linear-upwind stabilised transport (LUST) is selected as the divergence scheme that uses a blend between a linear and a linear upwind scheme. The blending-factor is set to 0.75 linear. This offers a balance between accuracy and stability derived from a range of LES cases.

F.2.6 Numerical process

Incompressible flows are dominated by the effects of pressure variations where their effects on the velocity field are significant. In this case the continuity equation does not act as a conservation of mass equation as it does for compressible flows but as an important constraint on the behaviour of the velocity field. How the pressure is derived from the continuity and momentum equations is not straightforward using primitive variables. Issa (1986) developed an improved pressure-velocity calculation method called the pressure-implicit with splitting of operators (PISO) scheme. It is an efficient method to solve the Navier-Stokes equations in unsteady problems. The simulation is executed via the following steps:

1. The pressure is assumed to be equal to p.
2. The momentum equation is solved with p for the different components of the velocity.
3. In an iterative process, the pressure equation is solved using the velocity at each previous time step.
4. The velocity is updated based on the computed pressure value.
5. The other variables are computed using the new values for the velocity and pressure
6. Depending on the input value for the corrector steps, this process is repeated from step 3 onwards.
7. At every new time step the process advances up to the final time specified.

Specific solvers for each individual parameter in the model equations can be specified. The solvers are specified in the `fvSolution` dictionary, which is explained in Appendix B. Although the implicit schemes in OpenFOAM allow for a Courant number greater than one, the number of correction steps can be reduced to decrease the simulation time. The model may also miss out on fluctuations or transient features when choosing a larger time step.

F.3 Results and analysis

In the remaining section of this chapter the results of the models are shown. Figures F.3 and F.4 are the first preliminary simulations for the cases of vertically attached and vertically separated flow, respectively. The upper models in the figures display the velocity magnitude after a simulation period of 25 s, computed as $|\bar{u}| = \sqrt{\bar{u_1} + \bar{u_2} + \bar{u_3}}$ [m/s].

The lower models indicate the time-averaged velocity magnitude over this time window.

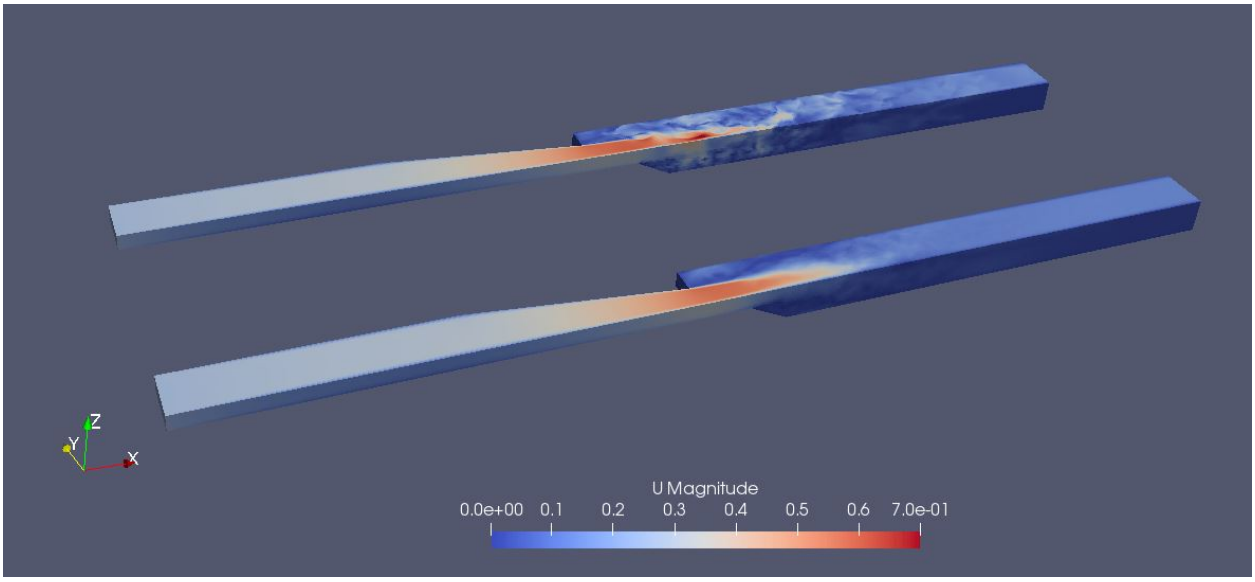

Figure F.3: Model results of the experiment with flow attachment. The upper model represents the time averaged velocity magnitude at t = 25 s, whereas the lower model illustrates the time-averaged results.

.

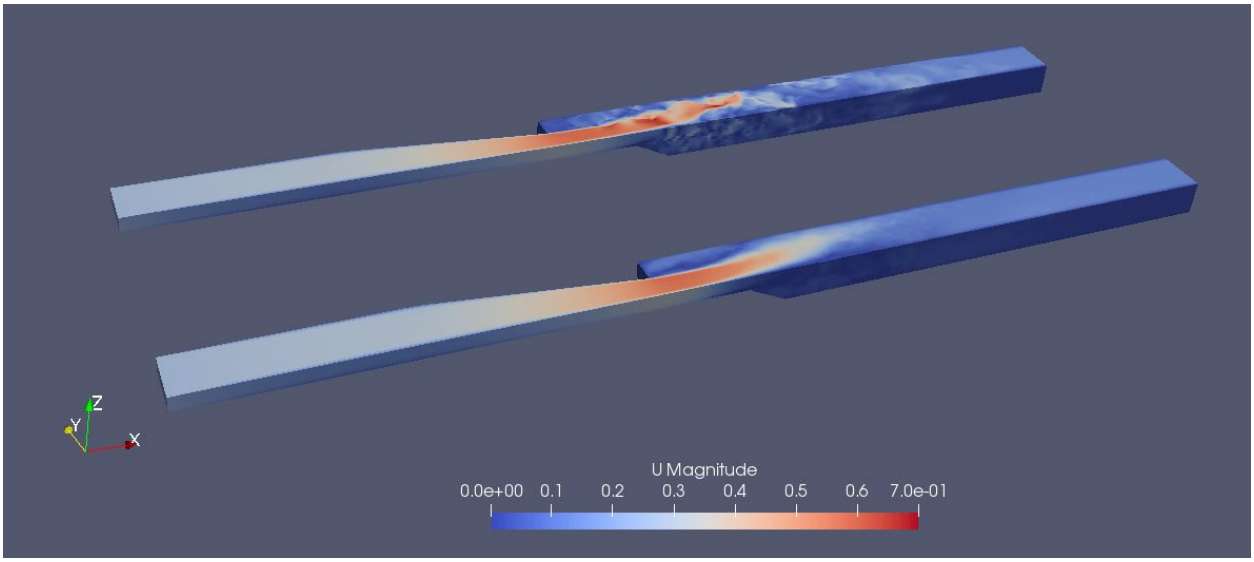

Figure F.4: Model results of the experiment with flow separation. The upper model represents the time averaged velocity magnitude at t = 25 s, whereas the lower model illustrates the time-averaged results.

.

The cases exclude the implementation of the `turbulentDFSEMInlet` as described in Section 5.3.4, causing the flow to be too laminar. Instead, a fixed value of 0.25 m/s was imposed on the inlet boundary. The time-averaged velocity magnitudes are nonetheless comparable to the results from the experimental cases of Broekema (2020), ranging between 0.5 and 0.6 m/s. For the vertically flow detached case (Figure F.3, a convergence of the flow towards the high velocity side is observed. In the other configuration, the flow diverges to the other side of the channel. Both phenomena are also identified by Broekema (2020). For both

cases, flow separation is absent.